Theses & Dissertations   Graduate Studies

Summer 8-14-2015

Polymeric Nanocarriers for Treatment of Melanoma and Genetically Modified Mesenchymal Stem Cells to Improve Outcome of Islet Transplantation

Vaibhav Mundra
University of Nebraska Medical Center

POLYMERIC NANOCARRIERS FOR TREATMENT OF MELANOMA AND GENETICALLY MODIFIED MESENCHYMAL STEM CELLS TO IMPROVE OUTCOME OF ISLET TRANSPLANTATION

by

Vaibhav Mundra

A DISSERTATION

Presented to the Faculty of
the University of Nebraska Graduate College
in Partial Fulfillment of the Requirements
for the Degree of Doctor of Philosophy

Pharmaceutical Sciences Graduate Program
Under the supervision of Professor Ram I. Mahato
University of Nebraska Medical Center
Omaha, Nebraska
August, 2015

Supervisory Committee:

Amarnath Natarajan, Ph.D.	Rakesh K. Singh, Ph.D.
Nora E. Sarvetnick, Ph.D.	Tatiana K. Bronich, Ph.D.

ACKNOWLEDGEMENTS

ABSTRACT

Melanoma is a lethal malignancy with limited treatment options for advanced metastatic stages. New targeted therapeutic options with discovery of BRAF and MEK inhibitors have shown significant survival benefit. Despite the recent progress, inefficient tumor accumulation and dose limiting systemic toxicity remains pressing challenges for treating metastatic melanoma and there is a need for drug delivery approach to improve therapeutic index of chemotherapeutics. Nanoparticle based drug delivery represents promising approach to enhance efficacy and reduce the dose limiting systemic toxicity. Nanoparticles can be formulated either by physical encapsulation of drugs or by covalent conjugation of drugs to the polymeric backbone. Nanoparticles based strategies for encapsulation and conjugation of drugs to the polymer was reviewed in Chapter 2 where we summarized non-covalent interactions between polymer backbone and drug for physical encapsulation, various polymeric backbones for drug conjugation and application of photodynamic therapy in melanoma.

Phototherapy, a light activated treatment modality is a potential therapeutic option for treatment of melanoma. Excitation of photosensitizer by light of specific wavelength can be clinically utilized for fluorescence assisted tumor surgery, photoacoustic imaging, photochemical internalization and phototherapy. Indocyanine green, water soluble FDA approved anionic tricarbocyanine with excellent safety profile and absorption in the near infrared (NIR) range is an excellent photosensitizer. However, short half-life (2-4 minutes) and limited extravascular distribution restricts PT application of ICG. In chapter 3, we have described ICG based phototherapy wherein plasma circulation and tumor accumulation of ICG was improved by designing its micelles formulation. ICG micelles

were formulated by covalently conjugating ICG-NH$_2$ to the pendant carboxyl groups of poly (ethylene glycol)-block-poly(2- methyl-2-carboxyl-propylene carbonate) (PEG-PCC) copolymer using carbodiimide coupling. ICG conjugated amphiphillic polymer self-assembled into micelles with particle size of 30-50 nm and high drug loading. These ICG conjugated micelles exhibited significant in vitro photodynamic cytotoxicity. Use of sodium azide and NIR radiation at 4° C revealed photodynamic and photothermal as primary mechanism of cytotoxicity of ICG solution and ICG conjugated micelles respectively. In vivo NIR imaging demonstrated ICG conjugated micelles prolonged ICG circulation and increased its tumor accumulation through enhanced permeability and retention effect Increase in tumor accumulation improved therapeutic efficacy with complete tumor regression in NIR irradiated ICG conjugated micelles compared to free ICG and control in A375 human melanoma tumor model in athymic nude mice. These results suggest that ICG conjugated micelles can be potentially utilized for phototherapy.

Clinical translation of tubulin inhibitors for treating melanoma is limited by multidrug efflux transporters, poor aqueous solubility, and dose-limiting peripheral toxicities. Tubulin inhibitors with efficacy in taxane-resistant cancers are promising drug candidates and can be used as single agent or in conjunction with other chemotherapy. In chapter 4, we describe synthesis of tubulin inhibitors with activity in taxane resistant cell lines with IC$_{50}$ in nanomolar range for the treatment of metastatic melanoma. LY293, a 5 indole derivative analog, binds to colchicine binding site and does not exhibit clinically prevalent drug resistance mechanism such as multidrug resistance (MDR) protein, breast cancer resistance protein (BCRP) and P-glycoprotein (P-gp). Since

LY293 is poorly soluble in water, LY293 was formulated as polymeric nanoparticles for systemic therapy of melanoma. Methoxy polyethylene glycol-b-poly (carbonate-co-lactide) (mPEG-b-P (CB-co-LA)) random copolymer was synthesized and characterized by ^{1}H NMR and gel permeation chromatography (GPC). Polymeric nanoparticles were formulated using o/w emulsification method with a mean particle size of 150 nm and loading efficiency of 7.40%. Treatment with LY293 loaded nanoparticles effectively inhibited the proliferation of melanoma cells in vitro and exhibited concentration dependent cell cycle arrest in G2/M phase. In vivo, LY293 loaded nanoparticles significantly inhibited the proliferation of highly aggressive metastasized melanoma in a syngeneic lung metastasis melanoma mouse model without toxicity to vital organs.

Islet transplantation has been performed in many patients especially undergoing kidney transplantation to treat Type I diabetes. Proportion of recipients who achieved insulin independence is low and is limited by long-term graft rejection and by primary non-function of islets. Primary non-function is characterized as the loss of islet viability and function caused by non-immune reasons, such as the disruption of islet microvasculature and apoptosis of islets due to production of inflammatory cytokines at the transplantation sites. In chapter 5, we studied the potential of human bone marrow derived mesenchymal stem cells (hBMSCs) as gene carriers for improving the outcome of human islet transplantation. hBMSCs were transduced with Adv-hVEGF-hIL-1Ra to overexpress human vascular endothelial growth factor (hVEGF) and human interleukin-1 receptor antagonist (hIL-1Ra). Viability of human islets co-cultured with hBMSCs was determined by membrane fluorescent method and glucose stimulation test. Transduced hBMSCs and human islets were co-transplanted under the kidney capsule

of NOD.Cg-*Prkdc^scid* *Il2rg^tm1Wjl*/SzJ diabetic mice and blood glucose levels were measured over time to evaluate the efficacy of genetically modified hBMSCs. Our in vitro and in vivo results showed hBMSCs can be used as gene delivery vehicles to improve the outcome of islet transplantation without affecting their stemness and differentiation potential.

LIST OF FIGURES

LIST OF ABBREVIATIONS

χFH	Flory–Huggins interaction parameter
Adv	Adenovirus
ABI	2-aryl-4-benzoyl-imidazole
ATCAA	2-aryl-thiazolidine-4-carboxylic acid amides ()
BRAF	Serine–threonine protein kinase B-RAF
BCRP	Breast cancer resistance protein
CMC	Critical micellar concentration
CSCs	Cancer stem cells
DOX	Doxorubicin
DTIC	Dacarbazine
EPR	Enhanced permeability and retention effect
FDA	Food and Drug Administration
GFLG	Gly–Phe–Leu–Gly
ICG	Indocyanine green
IEs	Islet equivalents
IFN-γ	Interferon-γ
IL-1β	Interleukin -1 beta
hBMSCs	Human bone marrow mesenchymal stem cells
hIL-1Ra	Human interleukin 1 receptor antagonist
hVEGF	Human vascular endothelial growth factor
HPMA	N-(2 hydroxypropyl) methacrlyamide
K_d	Distribution rate constant
K_r	Release rate constant
MAP	Mitogen-activated protein

MBC	2-Methyl-2-benzyloxycarbonyl-propylene carbonate
MC1R	Melanocortin type-1 receptor
MDR	Multidrug resistance
MOI	Multiplicity of infection
NIR	Near-infrared
PAT	Phenyl thiazole
P-gp	P-glycoprotein
PCI	Photochemical internilzation
PDT	Photodynamic therapy
PEG	Poly (ethylene glycol)
mPEG-b- P- (CB-co-LA)	methoxypoly (ethylene glycol)-b-poly(carbonate-co-lactide)
PEG-MBC	poly(ethylene glycol)-block-poly(2-methyl-2-benzoxycarbonyl-propylene carbonate)
PEG-PCC	poly(ethylene glycol)-block-poly(2-methyl-2-carboxylpropylene carbonate)
PG	Polyglutamate
PNF	Primary non-function
PT	Phototherapy
PTT	Photothermal therapy
PTX	Paclitaxel
RES	Reticuloendothelial system
ROP	Ring opening polymerization
ROS	Reactive oxygen species
SI	Stimulation index
SMART	4-substituted methoxybenzoylaryl- thiazoles

TBA	Tubulin binding agents
TEM	Transmission electron microscope
TNF-α	Tumor necrosis factor alpha
vWF	Von Willebrand factor

CHAPTER 1 INTRODUCTION

1.1 Polymeric nanocarriers for treatment of melanoma

Melanoma is an extremely aggressive type of skin cancer with a high potential of metastasis and ability to develop resistance to most anticancer agents. While surgery and radiation are the first line therapy for treating localized melanoma, systemic therapy is the cornerstone of clinical management of metastatic melanoma (1). Currently dacarbazine (DTIC) and kinase inhibitors are the Food and Drug Administration (FDA) approved drugs for the treatment of metastatic melanoma with modest efficacy and development of resistance (2-4). Tubulin inhibitors like vinca alkaloids and taxanes such as paclitaxel have been clinically prescribed as a single agent or in combination with other chemotherapeutic agents but efficacy are limited by development of resistance (5). Tubulin polymerization inhibitors with antiproliferative IC_{50} in nanomolar range and ability to circumvent multidrug resistance (MDR) protein, breast cancer resistance protein (BCRP) and P-glycoprotein (P-gp) was synthesized by our collaborator (6). However, poor aqueous solubility of (2-(1H-Indol-5-yl) thiazol-4-yl) 3, 4, 5-trimethoxyphenyl methanone (LY293) necessitates the use of cosolvent for its systemic delivery. Biodegradable polymeric nanoparticles are attractive formulation strategies for solubilizing the hydrophobic drug within their core and modulate the drug release. In chapter 3, we have synthesized and characterized a biodegradable amphiphillic polymer for nanoparticulate formulation of poorly soluble drug LY293: We carried out the proposed work with the following aims:

- Design and optimize synthesis of methoxypoly(ethylene glycol) -b- poly (carbonate-co-lactide) [mPEG-b-P (CB-co-LA)] and perform its characterization by 1H NMR and GPC

- Perform formulation and characterization of LY293 loaded nanoparticles.

- Determine the *in-vitro* anticancer efficacy, apoptosis and study of cell cycle perturbation by LY293

- Determine the *in-vivo* anticancer efficacy of nanoparticulate formulation of LY293 in lung metastatic melanoma mouse model after systemic administration.

In chapter 4, we have designed polymeric micelles of indocyanine green for phototherapy (PT) of melanoma. Phototherapy (PT), a combination of photodynamic therapy (PDT) and photothermal therapy (PTT) involves the administration of biocompatible photosensitizer followed by its excitation with light of specific wavelength which leads to generation of local heat and reactive oxygen species. The major advantage of PT is that both photosensitizer and irradiating light are inert by themselves and do not cause any systemic toxicity or collateral damage. However, application of indocyanine green is limited by its short plasma circulation half-life and inefficient tumor accumulation for phototherapy.   To improve the plasma circulation and thereby, enhance the tumor accumulation, we formulated and characterized micelles formulation of indocyanine green. We performed the work with the following aims:

- Synthesis and characterization of mPEG-b-PCC-g-indocyanine green -g-dodecanol (mPEG-PCC-g- NH2 ICG -g-DC)

- Formulation and characterization of ICG conjugated polymeric micelles

- Perform cellular uptake and in vitro phototoxicity with elucidation of mechanism of cytotoxicity

- Determine in vivo biodistribution using near infrared fluorescence imaging and in-vivo photodynamic toxicity

1.2 hBMSCs as gene delivery vehicles to express VEGF and IL-1Ra to improve the outcome of human islet transplantation

The main objective of this work was to study genetic modification of human bone marrow derived mesenchymal stem cells for improving the outcome of islet transplant. We have previously shown that genetic modification of human islet with growth factors and cytokines receptor antagonist improved the outcome of islet transplant (7, 8). However, transduction of islets with virus results in immune response especially when relatively higher multiplicity of infection (MOI) is used to get desired transgene expression (9).

To resolve this potential issue, we hypothesized that hBMSCs can be genetically modified by adenovirus for transgene expression and their use as gene delivery vehicles. In addition, hBMSCs also provide immune protection to islet grafts and improve the function and survival of grafted islet by secreting various growth factors. We carried out the proposed aim:

- Perform hBMSCs characterization, adenovirus transduction and quantification of transgene expression.

- Determine the effect of genetically modified BMSCs on islet viability and islet function in vitro.

- Determine the in vivo outcome of co-transplantation of genetic modified BMSCS and islet transplant in diabetic NSG mice.

3

CHAPTER 2 NANOPARTICLES MEDIATED DRUG DELIVERY FOR TREATING MELANOMA*

2.1 Introduction

Melanoma is the cancer of melanocytes which are present as single cells within the basal layer of epidermis. Melanoma is a highly aggressive skin cancer with potential of metastasis and responsible for majority of skin related deaths. The 5-year survival of metastasized melanoma is around 10 % (10). Systemic chemotherapy is mainstay for the treatment of melanoma and DTIC was standard of care for melanoma till the approval of new targeted kinase inhibitors. DTIC monotherapy is associated with a poor response rate of around 7.2-7.5 % and does not extend survival benefits (11).

About 60% of melanoma patients carry activating mutations in the gene encoding the serine–threonine protein kinase B-RAF (BRAF). Discovery of these activating mutations paved the way for development of small molecule inhibitors targeting mitogen-activated protein (MAP) kinase pathway. BRAF inhibitors (vemurafenib, dabrafenib), MEK inhibitor (trametinib), and the combination of dabrafenib with trametinib are the newest small molecules approved by the FDA approved for treating BRAF mutated melanoma. However, response to potent BRAF inhibitors is short lived and disease progression is seen at a median of 5-7 months (3, 12). Hence, there is a need for improved treatment options for effective treatment of melanoma. Tubulin binding agents (TBA), platinum analogues, anthracyclines and nitrosoureas have been clinically prescribed in melanoma as combination therapy (1) and exhibits comparable response rate to DTIC.

*Adapted with permission. Mundra V, Li W, Mahato RI. Nanoparticle-mediated drug delivery for treating melanoma. Nanomedicine (Lond). 2015;10(16):2613-33

However, multiple drug resistance (MDR) mechanisms, poor delivery and dose limiting systemic toxicity restrict the therapeutic application of these chemotherapeutic drugs. Thus, there is a need to improve the biodistribution of chemotherapeutics to tumor with minimum peripheral exposure and thereby minimize the systemic toxicity. Advent of nanoparticle based drug delivery resulted in tumor selective delivery of drugs by enhanced permeability and retention effect (EPR) with reduced peripheral exposure. Furthermore, interaction between receptors overexpressed by tumor and their ligands has been exploited to enhance the cellular uptake of nanoparticles. However, formulation of nanoparticles with enhanced stability in plasma and limited premature drug release are potential pitfalls in harnessing the improved biodistribution by EPR effect. Hence, we have reviewed the different polymer modifications to enhance the non-covalent interaction between polymer backbone and drug as well as polymer drug conjugates to design kinetically stable nanoparticles with enhanced drug loadings. In addition, nanoparticles based photodynamic therapy (PDT) presents exciting avenues for detection, treatment and evasion from possible mechanism of resistance from melanoma. In this chapter, we summarize the different polymer modification for preparation of nanoparticles, nanoparticles for PDT and targeted nanocarriers followed by conclusion and future outlook of nanoparticle based therapy for melanoma.

2.2 Drugs acting on tubulin polymerization

Microtubules are dynamic cytoskeleton structure in eukaryotic cells and play a key role in maintaining the cellular structure, transport of vesicles, cell signaling and mitosis (13). Microtubules are long, slender, filamentous, cylindrical tubes which are composed of α-tubulin and β- tubulin heterodimer. Microtubules results from polymerization of αβ tubulin heterodimer in two steps; nucleation and elongation. During nucleation, an

oligomer consisting of 6-12 αβ tubulin heterodimer units is formed. Reversible, non-covalent addition of αβ tubulin heterodimer to oligomer during elongation leads to the formation of protofilament. Polymerization of microtubules is dynamic process and hydrolysis of tubulin bound GTP provides energy. Microtubules essentially exhibit two different dynamic behavior, "treadmilling" and "dynamic instability". Treadmilling refers to the net addition of tubulin subunit to the plus end along with the net dissociation of subunit from the minus end without affecting the length of microtubules. Dynamic instability is characterized by alternate switch between phases of growth and shortening. One end of microtubules, plus end shows rapid and prominent growth and shortening as compared to the minus end (14). This rapid and prominent microtubule dynamics is essential for successful cell mitosis. Microtubules undergo extensive reorganization where plus end of microtubules binds kinetochores of chromosomes and arrangement of microtubules of metaphase plate. Oscillation of chromosomes at the metaphase plate and shortening of microtubules spindles leads to separation of the chromosomes and cell mitosis (15).

Crucial role played by microtubules in the cell mitosis makes them an ideal target for arresting rapid proliferating cancer cells and inducing apoptosis. Drugs acting on dynamics of polymerization are also known as antimitotic as these agents not only perturb mitosis but also arrest proliferating cancer cells during interphase. These microtubule targeting drugs can be classified as depolymerizing or polymerizing agents based on their action on assembly of microtubules. Antimitotic agents exert their effect by binding either to the αβ tubulin heterodimer subunit or by binding to the microtubule assembly. Majority of microtubules acting drugs were initially isolated from natural

products and paved the way for further development of microtubule acting agents. These agents interact with microtubules through at least four known sites; the laulimalide, taxane, vinca alkaloid and colchicine site (16). Vinca alkaloids were the first microtubule agents which were isolated from periwinkle leaves and arrest mitosis at metaphase. Vincristine, vinblastine and vinorelbine bind to the tubulin molecules at the growing tip of microtubules and thereby promote depolymerization of microtubules. At higher concentrations, vinca alkaloids also interact at the interface of two αβ tubulin heterodimer and prevent self-association of αβ tubulin subunits. Laulimalide, microtubule stabilizing agent have been isolated from marine sponge and show excellent cytotoxicity in vitro. Laulimalide binds to different site than PTX and stabilize microtubule. Laulimalide retains its activity in PTX resistant cell lines and P-gp over expressing cell lines. However, poor efficacy to toxicity ratio limited its therapeutic value (14). Taxanes bind to polymerized microtubule at β subunit and prevent the depolymerization of microtubules. Colchicine is isolated from *Colchicum autumnale L* and is used as monotherapy to treat familial Mediterranean fever and acute gout flares. Colchicine binds to the β-tubulin and gets polymerized into tubulin heterodimer. This high affinity binding of colchicine alters the straight structure of tubulin dimer to the curved structure and thereby destabilizing the microtubules. However, low therapeutic index of colchicine limits its clinical translation.

Successful chemical synthesis and clinical translation of taxanes and vinca alkaloids has made colchicine binding site as a promising site to target cancer cells. Several colchicine binding agents have been synthesized but no agent has been yet approved for clinical use. Our group has synthesized a series of 4-substituted

7

methoxybenzoylaryl- thiazoles (SMART) compounds with structural modification of lead compound, substituted 2-aryl-thiazolidine-4-carboxylic acid amides (ATCAA) (Figure 2.1). SMART compounds exhibited nanomolar efficacy against melanoma with activity against Pgp overexpressing cell lines and better toxicity profile compared to existing depolymerizing agent (17-19). These derivatives were synthesized with emphasis on structure-activity relationship (SAR) studies for the central thiazolidine ring of the ATCAA analogs, the effect of spacers, and to remove the chiral centers. Among the synthesized derivatives, SMART compounds containing hydrophobic thiazole ring have extremely poor water solubility which requires use of surfactants for effective dosing. In addition, thiazole ring of the SMART compounds may undergo oxidative cleavage resulting in a nitroxide and ultimately reduced *in vivo* stability for SMART analogs. Biomimetic replacement of the central thiazole ring of the SMART compounds with imidazole moiety was performed to design 2-aryl-4-benzoyl-imidazole (ABI) analogs. Imidazole moiety was introduced as imidazole is present in many existing drugs and has been proven to be very stable. Secondly, compared with the thiazole ring, the imidazole ring is much more hydrophilic, is expected to have improved aqueous solubility which would its systemic administration without toxicity. Preformulation and preclinical characterization confirmed this where compared to SMART; ABI analogs have higher water solubility, improved pharmacokinetic properties, and oral bioavailability without compromising activity (20). To further improve the aqueous solubility of thiazole derivatives, phenyl thiazole (PAT) analogue having an amino linkage were synthesized (Figure 2.1) (6, 20). PAT analogues exhibited nanomolar efficacy against melanoma and improved bioavailability as compared to SMART

8

analogues. Therapeutic potential of these synthesized ABI and SMART analogues can be further potentiated by minimizing the systemic side effects and improving their delivery to tumor.
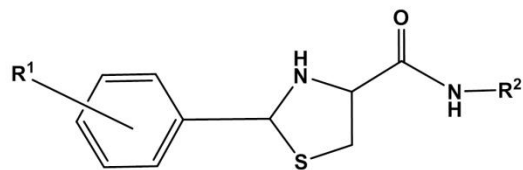
2-aryl-thiazolidine-4-carboxylic acid amides (ATCAA)
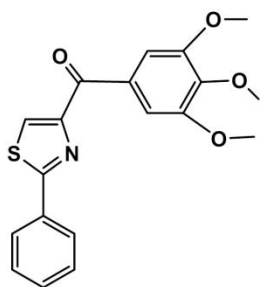
SMART: IC50 = 21-71 nM
Oral Bioavailability = 3.3 %
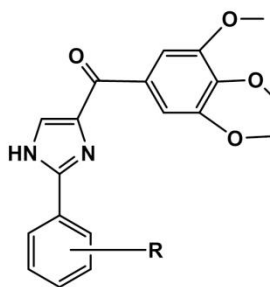
ABI: IC50 = 8-45 nM
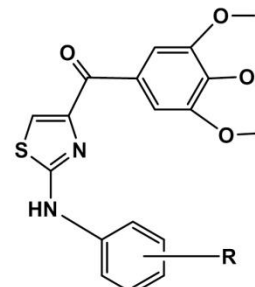
PAT: IC50 = 37-53 nM
Oral Bioavailability = 21 %

Figure 2-1.   Structure Activity Relationship of 4-substituted methoxybenzoylaryl thiazoles compound on efficacy and oral bioavailability

2.3 Nanotechnology for Drug Delivery

Lack of selectivity for tumor tissue, unfavorable physicochemical property and poor biopharmaceutical characteristics limit the therapeutic efficacy of anticancer drugs. Free drugs circulate throughout the body and permeate the cell membrane through passive diffusion. This non-selective distribution and cellular permeability of anticancer drugs is the primary reason for dose limiting toxicity (21, 22). Poor physicochemical and biopharmaceutical properties of anticancer drugs present additional challenges in their delivery. Drugs with low water solubility require cosolvent for their administration and causes systemic toxicity, whereas water soluble drugs are rapidly eliminated through kidney restricting the plasma residence time for their partition to tumor.

Nanotechnology has provided a platform to overcome these challenges and deliver drugs smartly to tumor (23, 24). Doxil and Abraxane are the two clinically approved nanoproducts of DOX and PTX with improved biodistribution and safety profiles, respectively. Micelles, nanoparticles, liposomes, dendrimers and polymer-drug conjugates are the most commonly used nanoparticles for drug delivery. Drugs delivery by nanoparticles exhibit altered biodistribution and pharmacokinetic profiles. Maeda et al. first have shown macromolecules preferentially accumulate at the tumor site due to enhanced vascular permeability and poor lymphatic drainage (25, 26). High molecular weight polymers (> 50 kDa) showed significant accumulation at 6 h while low molecular weight polymers cleared rapidly due to rapid diffusion into the blood stream. Prolonged circulation of nanoparticles improves their accumulation at the tumor site for local release of drug and/or uptake of drug loaded nanoparticles by cancer cells. To maximize the drug delivery, it is imperative that drug release rate constant (K_r) while nanoparticles are in the circulation should be miniscule as compared to distribution rate

11

constant of nanoparticles to tumor (K_d) (Figure 2.2). Premature release of drugs from the nanoparticles would nullify the advantage of EPR effect and biodistribution of nanoparticles associated drug would be identical to that of the free drug. However, drugs associated with the nanoparticles are pharmacologically inactive and requires drug release at the tumor site to show therapeutic effect. Considering this, the nanoparticles should be designed to allow effective accumulation of its payload at the tumor site but should be released quick enough to maintain the concentration of free drug above the IC_{50} values. Broadly, drugs are either encapsulated within the nanoparticles or conjugated to a lipid or polymeric nanoparticles. In the following sections, we would review drug encapsulation and conjugation approach in terms of formulation design, interaction between drug and polymer backbone for enhanced drug loading, drug release, and how the existing information can be utilized to design smart nanoparticles.
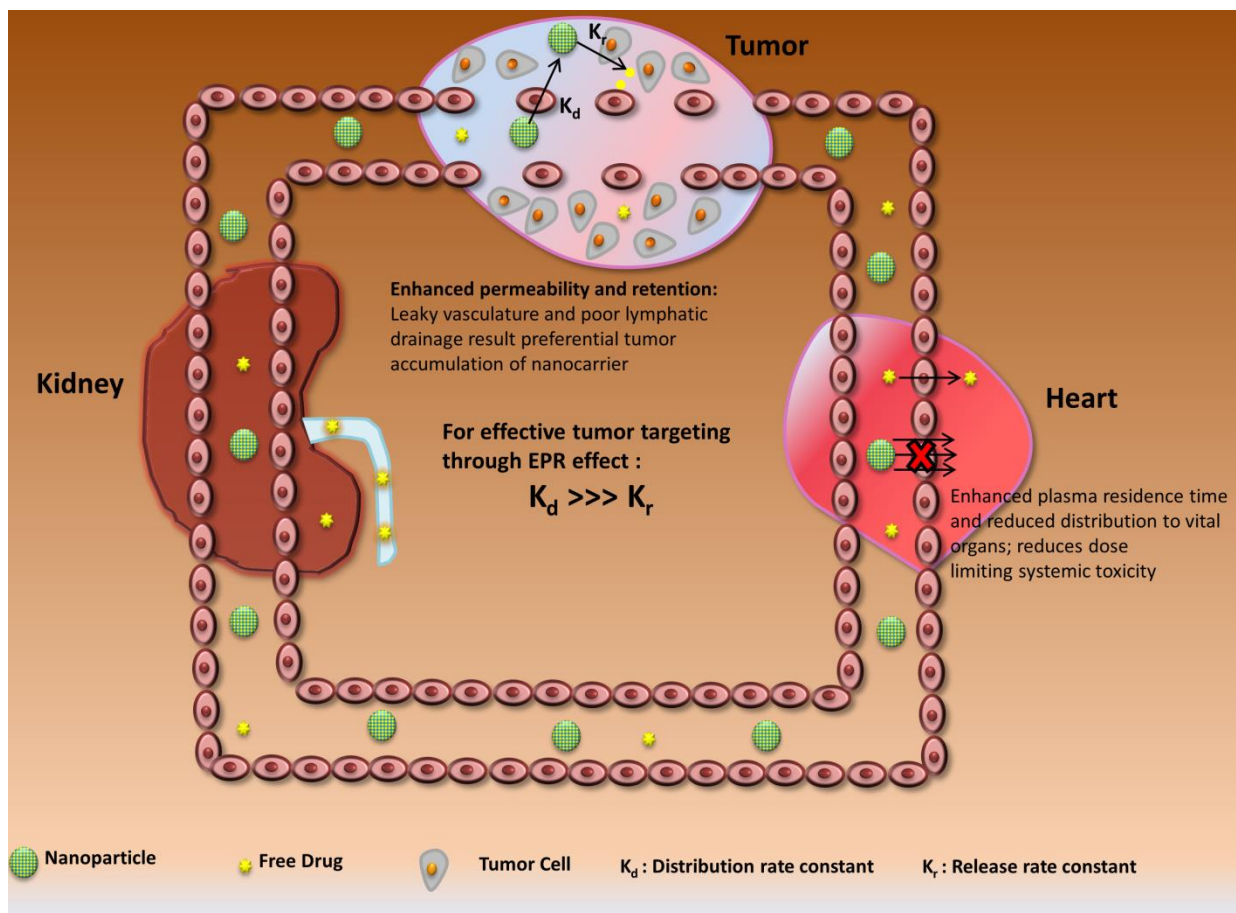
Figure 2-2.   Nanoparticles mediated drug delivery.

Poor extravasation of nanoparticles across endothelium of vital organs and enhanced permeability and retention of nanoparticles at tumor site result in preferential tumor distribution of chemotherapeutics. To harness full potential of nanoparticles based drug delivery, release rate constant of drug (K_r) from nanoparticles should be much smaller as compared to distribution rate constant (K_d) to prevent premature release of drug from nanoparticles while in circulation.

2.3.1 Nanoparticles for drug delivery

Low solubility of anticancer drugs is the major obstacle for systemic therapy. Nanomedicines have been extensively explored for the delivery of lipophilic drugs. Hydrophobic core of an amphiphillic polymer improves solubilization of poorly soluble drugs and has reduced toxicity compared to solubilization of drugs in cosolvent. Amphiphillic polymers encapsulate the drug based on non-covalent interactions like hydrophobic interaction, π-π stacking, hydrogen bonding and ionic interactions. Variety of PEG amphiphilic polyester and polyamide copolymers like poly(ethylene glycol)-b-poly-(aspartic acid) [PEG-b-PAA] (27), poly(ethylene glycol)-b-poly(lactide- co-glycolic acid) [PEG-b-PLGA] (28), poly(ethylene glycol)-b-poly(caprolactone) [PEG-b-PCL] (29) and poly(ethylene glycol)-b-poly(D,L-lactide) [PEG-b-PDLLA] (30) with biodegradable hydrophobic cores have been widely studied for formulation of poorly soluble drugs as nanoparticles. Key properties of these nanoparticles such as size, thermodynamic stability, drug loading and drug release kinetics have also been well reported (31-34). These studies have shown that non-covalent entrapment of drugs into nanoparticles is restricted by the lack of kinetic stability of polymer nanoparticles upon dilution, poor drug loading and premature release. To improve the nanoparticle stability and drug loading, copolymers have been modified to enhance non-covalent interactions like hydrophobic interaction, π-π stacking, hydrogen bonding and ionic interaction s between polymer and drugs (34-36). In this section, we would review the different modification of the nanoparticle core based on the drug characteristics and the critical role of drug properties in designing the core of micelles.

2.3.1.1   Hydrophobic interaction

Polymer/drug compatibility has been proposed as the key criteria affecting drug encapsulation within the core of micelles. Based on polymer/drug compatibility and thermodynamics, drug solubilization within micelles have been predicted which correlated well with the experimental findings (37). Polymer/drug compatibility has been characterized by the Flory–Huggins interaction parameter (χFH) which accounts for the forces of interaction between the polymer and the drug; and low χFH values suggest that the polymer is thermodynamically a good solvent for the drug (38, 39). We have previously modified the core of PEG-PLA to decrease χFH between polymer and bicalutamide. Introduction of the carbonate monomer within the core enhanced the interaction between bicalutamide and the core, minimized the χFH resulting in improved bicalutamide loading and enhanced stability (40, 41). Similarly, encapsulation of embelin was enhanced inside the core of polymeric micelles by modifying the carbonate core with dodecanol. Hydrophobic interaction of the long aliphatic chains of embelin within the core was improved by insertion of long aliphatic chain dodecanol. Interaction between the aliphatic chains enhanced the thermodynamic stability by reducing the critical micellar concentration (CMC) values and slow release of embelin from the micelle core (42). Mahmud et al. also reported chemical tailoring of the core with cholesteryl moieties to enhance the cholesterol-compatible Cucurbitacin I in the polymeric micelles (43). Increase in the drug/ polymer compatibility also affects the rate of drug release as higher drug compatibility with the micelle core results in a considerable decrease in the drug release rate as evident from the sustained release of Amphotericin B from fatty acid modified core of PEG-b-poly (amino acid) (43). Hydrophobic interaction can be critical for effective solubilization of a drug lacking

15

hydrophilic groups for other non-covalent interactions and compatibility between drug and micelle core should be evaluated for effective delivery by nanoparticles.

2.3.1.2 π-π stacking

Interaction between π clouds of aromatic rings of DNA base pairs has been well studied and this π - π stacking has been utilized for design of nanoparticles. Polymeric core has also been designed to facilitate the π - π stacking between the core and drug as most of the poorly soluble drugs contain aromatic rings which can participate in the π stacking and thereby, improve the stability of polymeric micelles with enhanced drug loading and sustained release. Kataoka et al have shown that dimers of DOX and DOX interacted with benzyl residue of poly (ethylene glycol)-poly(beta-benzyl-L-aspartate) block copolymer through π - π stacking. π - π stacking between the anthracycline moiety of DOX and benzyl side groups of polymer segment improved drug loading, exhibited sustained release and stabilized the micelles upon dilution (44). Several other groups also have attributed improved drug loading and self-assembly of DOX to the presence of aromatic group in the hydrophobic block of polymers (45, 46). PTX loading of % 34 has been reported with aromatic modification of N-(2 hydroxypropyl) methacrlyamide (HPMA) based micelles. Conjugation of benzoyl or naptholyl derivative to HPMA allowed π - π interaction with PTX which was confirmed by 1H solid-state NMR spectroscopy. π - π interaction between PTX and the aromatic core improved the drug retention within the core as evident from slow release (47).

π - π interaction also plays a critical role in enhancing the solubility of drugs by hydrotrophy. Hydrotropic molecules are believed to undergo aggregation by a stacking

mechanism of the planar aromatic ring present in their chemical structures. Lee et al designed amphiphillic polymers grafted with hydrotropic agents to the hydrophobic block of the copolymer. High local concentration of hydrotropic agents within the core allowed π-π stacking and solubilization of poorly soluble drugs within the core by hydrotrophy. Structural activity relationship of 60 hydrotropic agents confirmed the presence of pyridine and benzene rings within the hydrotropes is essential for solubilization of drugs and thereby confirmed the role of π-π interaction in polymer hydrotropes (48). Moreover, the presence of aromatic rings within the drug is also essential for solubility enhancement by hydrotropes which further confirmed the π-π stacking as the potential mechanism of the solubilization (49). These studies reflect that core of the polymer can be modified to amplify the π-π interaction between the drug and the core for enhanced dynamic stability of nanoparticles, increased drug loading and sustained release.

2.3.1.3   Hydrogen bond and ionic interaction

Core of the micelles has been manipulated to improve the drug loading of weakly acidic and basic drugs. Micelle core containing carboxylic acid has been extensively reported for encapsulation of anticancer drugs DOX and cisplatin (27, 50-53). Ionic interaction between amino group of DOX (pka =8.25) and polymer with carboxylic group resulted in significantly high drug loading and pH dependent DOX release. Strong ionic interaction between cationic drug and polymer is an enthalipically driven process and the encapsulated drug exhibited stoichiometry proportion of 1:1 to molar concentration of carboxyl group of polymer. Loading of polymer bound drug by ionic interaction is further enhanced by stacking interactions among the drug molecule (54). Similarly,

Borsali et al. reported high loading capacity and pH dependent drug release for weakly acidic drugs containing carboxyl functional groups. Core of PEG-poly acrylates was modified with the amino groups to design micelles with weakly basic core. Micelles with weakly basic core resulted in high drug loading of % 50 w/w, which reversed upon esterification of carboxylic groups of these drugs. Role of the acid-base interaction was further confirmed by poor loading capacities with nonionic polyester block copolymers (55). These studies indicate that weakly acidic and basic drugs can be effectively encapsulated at high loading with the modified core of the micelles.

Majority of drugs contain carbonyl groups, hydroxyl groups and amine group which could act as hydrogen-bonding sites. Polymers have been designed for hydrogen bond interaction between the micelle core and hydrogen-bonding sites of the drugs. Hamaguchi et al. reported enhanced drug loading and stable micelles of PTX by modification of the polyaspartate block by 4-phenol-1-butanol. Hydrogen bond interaction between 4-phenol-1-butanol and PTX significantly improved the micelles stability followed by sustained release. This enhanced stability improved the tumor accumulation by 25 fold as compared to free PTX and significantly reduced the associated neurotoxicity further improving the therapeutic profile of PTX (56). Core of the poly-glutamate was grafted with aliphatic, aromatic hydrocarbons and polar side chains to evaluate the effect of hydrogen bond on micellar formulation of PTX. Although blank micelles containing polar groups were thermodynamically less stable, they showed enhanced drug loading, kinetic stability and sustained release of PTX. These enhanced stabilization is due to the additional stabilization by hydrogen-bonding interaction between the polar groups grafted micelle core and the encapsulated PTX

(57). Hydrogen bond interaction has also been utilized to improve the kinetic stability of micelles. Modification of the core of micelles with the urea which is known to associate through bifurcated hydrogen bonds has been reported (58). These urea-containing polymers stabilized micelles by hydrogen bonding Interactions leading to greater kinetic stability with narrow size distribution and high cargo loading capacity. These studies underline the significance of hydrogen bond and ionic interactions in formulation of kinetically stable nanoparticles with high drug loading capacity and sustained release.

2.3.2 Polymer-Drug conjugate

Functional groups of certain drugs and their prodrugs allow covalent conjugation to the polymers for their formulation into nanoparticles. Molecular weight, conjugation chemistry, and biodegradability are the key properties which affect the biodistribution and efficacy of polymer-drug conjugate (59, 60). For efficient plasma circulation and tumor accumulation, ideally molecular weight of the polymer-drug conjugate should be higher than 40 kDa as renal threshold for polymer elimination is approximately 30-40 kDa (61). However, application of high molecular weight polymer may be limited by non-degradable nature of certain polymers and a balanced approach is required between renal elimination and enhanced tumor accumulation by EPR effect. Stability of polymer-drug conjugate in the circulation depends upon the covalent chemistry as well as molecular architecture of polymer-drug conjugate (61). Ester, amide, hydrazone and enzyme sensitive linkers have been reported for conjugation of numerous drugs. This different chemistry has been utilized to synthesize polymer-drug conjugate which are stable in plasma but would release the drug at the tumor site at a desired rate. In general, ester bonds undergo rapid hydrolysis contributing to poor stability in plasma

whereas poor hydrolysis of amide bond restricts the release of drug at the tumor site. To resolve this, polymer drug linkers have been designed for intracellular or tumor specific release of the drug. Among the linkers, tetrapeptide sequence Gly–Phe–Leu–Gly (GFLG) for cleavage by lysosomal proteases (especially cathepsin B) has been widely studied for intracellular drug release (62, 63). However, intracellular drug release from these conjugates is limited by poor cellular uptake of these hydrophilic polymer-drug conjugate which is reflected by higher in vitro IC_{50} of these conjugates (64, 65). An ideal polymer-drug conjugate should be biodegradable, non-immunogenic, stable in plasma and exhibit rapid cell uptake followed by intracellular enzymatic hydrolysis or extracellular release at desired rate. In the following section, we would review the different polymers which have been extensively studied for polymer-drug conjugate.

Polyglutamic acid

Polyethylene glycol
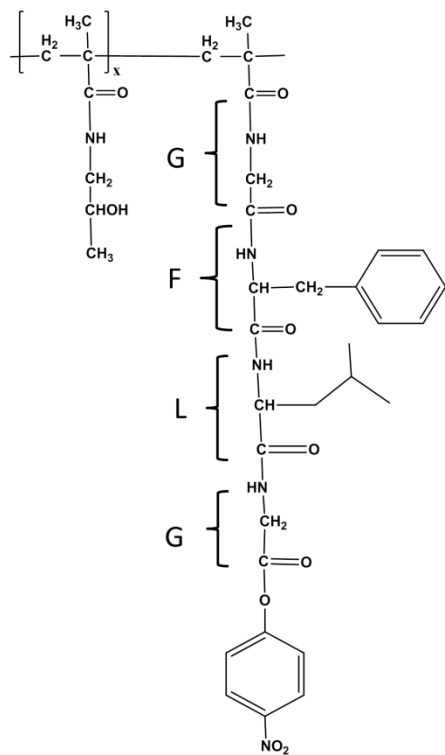
N-(2 Hydroxypropyl) methacrlyamide
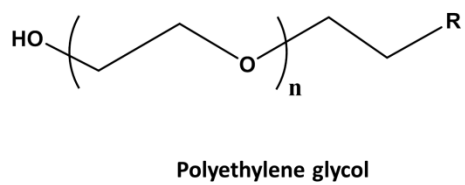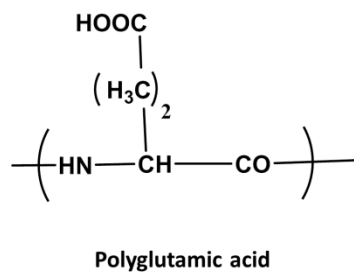
Figure 2-3. **Chemical structure of polymeric backbone used for formulation of polymer-drug conjugate.**

2.3.2.1 Polyethylene glycol (PEG)-drug conjugate

PEGylation of drugs and proteins is well-established and has been extensively used in clinically approved products. Excellent biocompatibility and end group chemistry allows efficient conjugation of drugs to PEG (Figure 2.3). PEG with COOH, NH_2, OH or SH reactive functional groups has been synthesized to conjugate drugs and proteins. Covalent conjugation of PTX, methotrexate (MTX), cisplatin, gemicitabine and camptothecin leading to the formation of ester, amide or disulphide bond has been reported. Enzon has reported the water soluble PEG-PTX conjugate of 40 kDa with 4% loading and equivalent in vivo toxicity (66). Renal threshold for clearance of PEG is approximately 20 kDa and the circulation half-life of PEG dramatically increases from 18 minutes to 16.5 hours as the molecular weight is increased from 6 kDa to 50 kDa (67). However, the utilization of high molecular weight PEG is limited by its non-degradable nature. To overcome this potential challenge, PEG with heterobifunctional reactive groups has been synthesized to attach PEG to nanoparticles (68, 69). Polyester units of PEG copolymer increase the molecular weight of PEG-drug conjugate and are also biodegradable in nature. Unlike PEG-drug conjugate, PEG polyester copolymer-drug conjugate are generally amphiphillic and forms nanoparticles.

There are no reported studies to characterize and quantify kinetics of the cellular uptake of PEG-drug conjugate. Krtaz et al have reported the synthesis of PEG-MTX conjugate of molecular weight ranging from 750 to 40000 Da. All the conjugates exhibited 60-200 fold increase in IC50 values despite the similar inhibitory action on dihydrofolate reductase enzyme in cell free system (70). This increase in IC_{50} value can be attributed to either inefficient cellular uptake or slow hydrolysis of free drug in the cytosol. Hydrolysis of drug as rate limiting step can be ruled out as even rapid release of

DOX from PEG-DOX conjugates with GFLG linker exhibited much higher IC_{50} as compared to free drug. These studies confirmed that cellular uptake rather than drug release from PEG-drug conjugate results in higher IC50 values of PEG-drug conjugate (71). Veronese et al. studied poly(ethylene glycol) PEG-doxorubicin (Dox) conjugates of linear or branched architecture of different molecular weight and with different peptidyl linkers (GFLG, GLFG, GLG, GGRR, and RGLG). Rapid hydrolysis of GFLG linker by lysosomal enzymes in vitro resulted in approximately 57% DOX release at 5 h, as compared to the other linkers (<16% release at 5 h). Highest molecular weight PEG had the longest plasma residence time and consequently the greatest tumor targeting with significantly lower anthracycline levels in heart which highlights the favorable biodistribution by PEG-drug conjugate (71). PEG-drug conjugate has been pre-clinically tested for numerous anticancer drugs but challenges like limited capacity for drug conjugation, poor cellular uptake and non-degradable nature restricted further clinical development of PEG-drug conjugate.

2.3.2.2   N-(2 Hydroxypropyl) methacrlyamide (HPMA) drug conjugate

Application of copolymers of HPMA as drug conjugate was pioneered by Kopecek and co-workers (72). Mainly, HPMA copolymer intermediates for conjugation are synthesized by free radical polymerization using HPMA and methacryloylated (MA)-peptidyl-nitrophenylester as comonomers (Figure 2.3). Facile synthesis of HPMA copolymer allowed incorporation of different functionalities with precise control of molecular weight and composition. HPMA polymer backbone is non-degradable limiting the molecular weight of polymer-drug conjugate below 40,000 kDa to ensure eventual renal elimination. HPMA copolymer-GFLG-DOX-conjugate has been extensively studied clinically. HPMA-DOX conjugate demonstrated enhanced blood levels of DOX with four

to five fold increase in the maximum tolerated dose (73). By contrast, HPMA conjugates of PTX and camptothecin did not show significant improvement from parent molecules. This was attributed to poor plasma stability of ester conjugation of drugs to polymeric backbone which highlights the importance of optimization of conjugation chemistry (74, 75). Etrych et al. reported synthesis of HPMA-PTX conjugate through pH sensitive hydrazone bond (76). HPMA-PTX conjugate through hydrazone bond showed enhanced plasma stability with drug release at mild acidic conditions (pH= 5). However, further clinical translation of HPMA-drug conjugate is limited by rapid renal elimination with 50–75% elimination over 24 h (73). To use high molecular weight HPMA-drug conjugate, Yang et al reported synthesis of high molecular weight HPMA–drug conjugate which contained enzymatically degradable bonds in the polymer backbone. This high molecular weight multiblock HPMA copolymer with enzymatically degradable linker between HPMA blocks with molecular weight distributions below the renal threshold were reported for delivery of gemcitabine (77). Increase in molecular weight of the second-generation enzyme degradable HPMA-drug conjugates resulted in distinct advantages as improved pharmacokinetics (three- to five-times half-life compared with the first generation), and dramatically enhanced tumor inhibition (78). Future clinical translation of HPMA-drug conjugate would depend upon synthesis of second-generation long circulating HPMA-drug conjugates and selective release of drug at the tumor site.

2.3.2.3   Polyglutamate (PG)-drug conjugate

Polyglutamate (PG) is composed of degradable amide bond unlike non-degradable carbon-carbon backbone of PEG and HPMA. PG is generated from hydrolytic removal of benzyl group of poly (γ- benzyl -L- glutamate) and carboxyl group of pendant free PG is utilized for drug conjugation (Figure 2.3). PG-drug conjugates are water soluble and

acquire α helix or random coil structure depending upon the pH of the surrounding media. PG is stable in plasma and long circulation time allows accumulation at tumors. PG like other macromolecules is extensively secreted by kidney and follows the renal threshold cut off for water soluble polymers (79). High molecular weight PG has been shown to activate the fibrinolytic system and week immunogenic response depending when the PG-drug conjugates are administered (80). Li et al. has done extensive work on PG-drug conjugates and extensively characterized PG-drug conjugate of numerous drugs (81).

PG-anthracycline conjugates have been reported using ester, amide, peptide and hydrazone linkers (82-84). All of the PG conjugates have higher in vitro cytotoxicity compared to the free drug. This is attributed to the slow release of the free drug from PG-DOX conjugate. Preclinical data have shown that the conjugate with oligopeptide spacer were active, whereas conjugates without degradable spacers were completely inactive. Increase in the rate of DOX release with increase in the length of spacer improved in vitro and in vivo anticancer effect of PG-DOX conjugate (85). Water soluble PG-PTX conjugate was also synthesized through ester linkage of 2' hydroxyl group of PTX. PG-PTX conjugate exhibited remarkable high loading of 37% and stability in plasma due to molecular architecture. Cellular uptake of radiolabeled PTX and PG backbone suggested that PTX is hydrolyzed extracellularly which was taken up by cells (64). PG-PTX exhibited excellent efficacy in different cancer models as PG-PTX exhibited enhanced circulation in comparison to free PTX and released the drug in the vicinity of tumor (86). PG-PTX has shown excellent safety with equipotent efficacy in

variety of cancer in Phase III trials and highlights the future potential of PG-drug conjugate based nanoparticles.

2.4 Nanoparticles for photodynamic therapy and detection

Photodynamic therapy (PDT) is an exciting detection and treatment modality for melanoma. PDT is based on the excitation of photosensitizer at a specific wavelength of light after preferential tumor accumulation of photosensitizer. Nanoparticles for PDT can be designed for metastasis detection, destruction of bulk tumor and cancer stem cells (CSCs), for photoimmunothrepay and for improving drug delivery at both tumor and cellular level. Galanzha et al reported a novel diagnostic and therapeutic platform with gold carbon nanotubes. Noninvasive in vivo detection and treatment of metastatic melanoma at single cell level was achieved after administration of gold carbon nanotubes by using a combination of PA imaging and photothermal (PT) therapy (87). Nanoparticles labeled with CSCs markers allowed detection and ablation of CSCs by multifunctional PAFC/PTFC nanoparticle based platform. CD44 labelled gold carbon nanotubes enabled ultrasensitive detection of CSCs in vivo (88). PT with antibody labeled nanoparticles selectively targeted and eradicated CSCs (89, 90). These studies highlight the immense potential of nanotechnology based PDT in detection and treatment of circulating tumor cells and CSCs.

Destruction of primary tumor lesion with modulation of immunity against the tumor antigen is potential therapeutic option against metastatic melanoma (91, 92). Photoimmunotherapy, combination of PDT and immunomodulation using adjuvant has demonstrated significant benefits in late stage metastatic melanoma (93, 94). PDT with indocyanine green (ICG) followed by local application of immunostimulant imiquimod resulted in beneficial systemic response against metastatic melanoma (93, 94). To

further improve tumor selective delivery of both immunostimulant and photodynamic agents, nanoparticles have been formulated (95). Bear et al. demonstrated PDT with gold nanoparticles in combination with adoptive T cell transfer prevented primary tumor recurrence post-ablation, inhibited tumor growth at distant sites, and abrogated the outgrowth of lung metastases (96). Also, nanoparticles co-delivering photodynamic agent and immunostimulant exhibited excellent anticancer effect against primary treated and distant untreated tumors. Chitosan-coating around hollow CuS nanoparticles allowed incorporation of the immunoadjuvants containing the cytosine-guanine (CpG) motifs. NIR irradiation triggered disintegration of CuS nanoparticles, allowing the complexation of chitosan and CpG motifs. Nanocomplexation of CpG motifs enhanced their tumor retention and uptake by plasmacytoid dendritic cells (95).

High tumor interstitial pressure and inefficient EPR effect can restrict the drug delivery by nanoparticles. PDT has been shown to improve the nanoparticle mediated drug delivery by reducing interstitial pressure and enhancing tumor vessel permeability. PDT resulted in ~2.5-fold higher tumor uptake at 3 h after administration of liposomal DOX by enlarging the endothelial gap of tumor vessels (97). PDT selectively enhances tumor accumulation of nanoparticles mediated chemotherapy as intratumoral accumulation of free DOX after PDT did not change. Tumor vessel targeted delivery of photosensitizer was achieved by arginine–glycine–aspartic acid (RGD)-modified ferritin. Ferritin encapsulating photosensitizer hexadecafluoro zinc phthalocyanine located to the endothelium of neoplastic vessels *via* RGD–integrin interactions. Photoradiation of tumor vessel located photosensitizer increased the vascular permeability of albumin, quantum dots, and iron oxide nanoparticles by as much as 20 fold with no adverse

27

effects to normal tissues. Enhanced tumor permeability by PDT improved the therapeutic efficacy of liposomal DOX by 75.3% highlighting the potential of PDT in improving the delivery of chemotherapeutics by nanoparticles (98).

Photochemical internilzation (PCI) was established at Norwegian Radium Hospital for cytosolic delivery of therapeutic agents entrapped in endocytic vesicles (99). PCI has been extensively studied for cytosolic delivery of toxins, oligonucleotides, weakly basic drugs like DOX and cisplatin and can be therapeutically exploited for overcoming resistance by efflux transporters as well as intracellular sequesterization of drugs (100-102). Light mediated activation of endocytosed amphiphillic photosensitizer generates reactive oxygen species which damages membrane of endocytic vesicles and thereby leading to cytosolic delivery of therapeutic agent. Nanoparticles encapsulating phthalocyanine upon radiation exhibited PCI properties and facilitated DOX release from the endo-lysosomes to nuclei. This increase in intracellular concentration of DOX resulted in significant reduction in tumor volume (103). Nanoparticles of weakly basic drugs, oligonucleotides and toxin are excellent candidates for combination therapy with PCI as they accumulate in endolysosomes compartment after cellular uptake (104, 105). PCI mediated cytosolic delivery of immunotoxins saporin and gelonin have been studied melanoma xenograft model (101, 106). PCI improved the anticancer response effect of immunotoxins and complete regression was observed in 33% of tumor-bearing mice (101). All these studies highlight the multifold potential of PDT and can be combined with chemo and immunotherapy for metastasis detection, destruction of bulk tumor cells and CSCs and for improving drug delivery in melanoma.

2.5 Active targeting of nanoparticles to melanoma

Passive targeting by EPR effect of nanoparticles improves tumor accumulation but do not enhance the cellular uptake and depends upon the convective transport of nanoparticles against high interstitial pressure (107). To further improve the therapeutic efficacy of nanoparticles, interaction between receptor and ligands has been exploited for active targeting of nanoparticles (108). Peptides, antibodies, small molecules and aptamers have been extensively studied to accomplish active targeting of nanoparticles (109). Nanoparticles for active targeting against tumor vasculature, stromal microenvironments and cell surface receptors have been investigated in preclinical models of melanoma.

Endothelial cells of tumor neovasculature overexpress $\alpha v \beta 3$ integrin receptor in comparison to low or negligible expression by normal vasculature (110). $\alpha v \beta 3$ integrin receptor not only promotes angiogenesis but also supports melanoma growth, adhesive, invasive and migratory properties of the melanoma tumor cells (111). Tripeptide motif RGD, cell adhesion peptide sequence in ECM proteins and its derivatives been extensively studied for design of $\alpha v \beta 3$ targeted nanoparticles (112). Benzera et al. reported significant increase in tumor-to-blood residence time ratios, and tumor-selective accumulation with cyclic RGD peptide ligands modified silica nanoparticles in melanoma xenograft mouse model (113). Surface modification of DOX loaded nanoparticles with DI17E6, a humanized monoclonal antibody against αv-integrins enhanced the integrin receptor specific cellular uptake in melanoma M21 cell line. Targeted nanoparticle reduced the integrin mediated attachment of cells to ECM proteins with enhanced cell cytotoxicity. Enhanced alpha integrin mediated uptake of

DOX loaded nanoparticles significantly reduced the IC50 from 55 to 8 nm in integrin positive melanoma cell line (114).

Progression of melanoma is associated with stromal changes contributing to uncontrolled growth and invasive behavior of melanocytes. These characteristic stromal changes have been exploited to target nanoparticles to tumor stroma. Secreted protein acidic and rich in cysteine (SPARC) a nonstructural matricellular protein has been well studied in the tumorigenicity and progression of melanoma (115-117). Peptide sequence with high affinity and specificity for SPARC protein has been identified by phage display. SPARC targeting peptide modified nanoparticles exhibited high affinity with negligible binding in negative cell lines. Targeting of nanoparticles to SPARC did not alter their blood clearance but there was a 45 fold increase in tumor accumulation of SPARC targeted nanoparticles as compared to the control group. Moreover, SPARC labeled proteins allowed detection of metastatic growth in addition to primary tumors (118). Albumin also exhibits SPARC binding properties and enhances the tumor accumulation of albumin nanoparticles (119-121). Albumin bound PTX nanoparticles (nabPTX) exhibited enhanced response in SPARC overexpressing xenograft in comparison to wild type PC3 tumor xenograft (120). However, these results are largely correlative with small sample size. Also, there are studies which demonstrated efficacy of nabPTX independent of SPARC expression (122-124). Tumor stroma also contains a mesh network of fibrin and fibronectin. Pentapeptide CREKA has been reported to bind to this mesh like network and further enhances the formation of clot like mesh at the target site. CREKA labeled nanoparticles and liposomes showed enhanced accumulation in tumor vessels with induction of additional localized clotting and thereby

producing new binding sites for more particles. This clotting-based amplification greatly enhanced tumor imaging with envision of the design of drug-carrying self-targeting nanoparticles (125).

Cancer cells overexpress receptors for cellular uptake of essential nutrients to meet their high proliferation rate. Transferrin receptor, a type II transmembrane glycoprotein is overexpressed by cancer cells to meet growing demands of iron (126). Targeting overexpression of transferrin receptor with its ligand, transferrin has been extensively studied for targeted delivery of nanoparticles (126). Davis et al reported the first in human clinical trial with transferrin targeted nanoparticles (127). Targeted nanoparticles exhibited dose dependent localization within transferrin positive melanoma tissue with little localization in the adjacent epidermis. Intracellular delivery of nanoparticles was observed only in the transferrin targeted nanoparticles which highlights the need of targeted nanoparticles for intracellular delivery (128, 129). Altered glycosylation patterns are a hallmark of the malignant growth. Proliferation of cancer cells is associated with enhanced sialylation of N linked glycans and this altered glycosylation enabled the design of sialic acid targeted nanoparticles (130, 131). Phenylboronic acid (PBA) reversibly binds with 1,2- or 1,3-diols, which are major constituent of glycan. PBA-sugar complexes are unstable at plasma pH, however PBA forms extremely stable complex with sialic acid at physiological pH (132). This tumor specific sialic acid recognition at physiological pH with controlled pK_a of PBA, have been studied as a molecular basis for the design of targeted nanoparticles. Deshayes et al. reported the design of PBA modified nanoparticles for enhanced delivery to melanoma (133). PBA targeted nanoparticles exhibited higher tumor accumulation level indicating interaction of PBA

targeted nanoparticles with the sialic acid moieties on the surface of cancer cells improved the retention of nanoparticles at the tumor site. PBA targeted nanoparticles demonstrated improved efficacy as compared to non-targeted nanoparticles correlating with their enhanced accumulation in tumors.

Progression of melanoma is associated with expression of high levels of the melanocortin type-1 receptor (MC1R) making it one of the melanoma specific targets for highly sensitive detection and therapy of metastatic melanoma (134). α-MSH, a tridecapeptide and its derivatives have been investigated for melanoma specific targeting (135). Conjugation of MSH derivative as targeting moiety significantly reduced the tumor burden upon PDT with gold nanoparticles. Receptor mediated uptake of targeted nanoparticles resulting into the enhanced tumor nanoparticle levels caused significantly greater necrotic response than non-targeted nanoparticles. Targeting improved the nanoparticle distribution within the tumor matrix as suggested by their presence at >200 µm away from the nearest blood vessels whereas non-targeted were scattered only adjacent to tumor vasculature. Enhanced retention and uptake was confirmed by co-localization of targeted nanoparticles and MC1R (136). Similarly, targeting MC1R raised the sensitivity and specificity of PA imaging with gold nanocages by 300 %. Interaction between MC1R and targeting ligand enhanced nanoparticle per tumor mass by 360 % highlighting that targeted systems can detect early stage melanomas metastatic lymph nodes, and can be potentially used to treat the melanomas (137). Besides MC1R, chondroitin Sulphate Proteoglycan 4 (CSPG4) is a highly specific marker of the nevomelanocyte lineage and has been utilized for targeting melanoma. Ep1 monoclonal antibody to the human melanoma-specific antigen CSPG4

targeted nanoparticles showed a 25-fold preference for melanoma as compared to non-target cells. Selectivity for melanoma was also confirmed in xenograft models where targeted nanoparticles significantly inhibited growth of melanoma xenograft with little effect in breast carcinoma xenograft (138). This all studies highlight the potential of active targeting to improve the outcome of nanoparticle based therapy. However, tumor heterogeneity and translation of preclinical xenograft data to human tumor are the major roadblocks.

2.6 Conclusion

Numerous anticancer drugs have been discovered through advancement in the molecular biology and drug discovery. All these anticancer drugs exhibit excellent efficacy in petri dishes but fail during translation to clinic. BRAF and MEK inhibitors show remarkable response in initial therapy but resistance develops invariably. Moreover, non-specific distribution of BRAF inhibitors leads to malignant and benign growth including squamous cell carcinomas and other severe dermatological side effects (139, 140). Combination therapy to overcome the potential resistance mechanism is the way forward for preventing the relapse. However, unfavorable physicochemical properties and pharmacokinetic profiles limit the clinical application of conventional chemotherapeutics as combination therapy. Nanoparticles based formulation approach to minimize peripheral exposure and to maximize tumor accumulation can be exploited to overcome these potential roadblocks.

Significant progress has been made since the idea of polymer based delivery was first conceived (141). Active targeting strategies using stimuli sensitive and receptor targeted nanoparticles have been devised to further augment the application of nanoparticles based delivery of chemotherapeutics. Despite of all these efforts, there

are limited numbers of approved nanoparticles based products which is due to challenges associated with the formulation of kinetically stable nanoparticles with high drug loading, and controlled release. It would require a concerted effort between drug discovery and formulation scientist to maximize the interaction between polymer and drugs for optimum design of nanoparticles based drug delivery.

CHAPTER 3 MICELLAR FORMULATION OF INDOCYANINE GREEN FOR PHOTODYNAMIC THERAPY OF MELANOMA

3.1 Introduction

Lack of selectivity of chemotherapeutics towards tumor tissue and their dose limiting toxicity led to the development of alternative therapeutic approaches (142). Phototherapy (PT), a combination of photodynamic therapy (PDT) and photothermal therapy (PTT) represents such an approach with improved selectivity and lesser side effects as compared to conventional radiotherapy and chemotherapy. PT involves the administration of non-toxic photosensitizer (PS) followed by its excitation with the light of specific wavelength which leads to the generation of local heat and reactive oxygen species (ROS) particularly singlet oxygen. Tumor selective radiation of PS followed by localized generation of ROS and heat results in selective and efficient destruction of cancer with no or minimal toxicity to normal tissue (143).

Currently, all the food and drug administration (FDA) approved PS absorb in the visible spectral regions restricting light penetration into the skin to only a few millimeters which limits the clinical application of PT for treating topical lesions only (144). The near-infrared (NIR) PS has relatively low tissue absorption, low scattering and minimal auto fluorescence allowing deep tissue penetration for PT. Indocyanine green (ICG), a water soluble anionic tricarbocyanine dye is the only FDA approved NIR agent which has been widely utilized clinically for medical imaging and hepatic function diagnosis (145). ICG strongly absorbs light around 800 nm with minimal scattering and fluorescence interference by biomolecules at this wavelength.

In spite of the excellent safety profile and absorption in the NIR range, short half-life (2-4 minutes) and limited extravascular distribution restricts PT application of ICG. ICG

binds to HDL_3 lipoprotein, albumin and undergoes extensive hepatobiliary secretion restricting its peripheral distribution and sufficient tumor accumulation for PT (146). To prolong its systemic circulation and improve tumor distribution, various formulations of ICG prepared with polyallylamine, calcium phosphate, polymer, hyaluronic acid, liposomes, silica nanoparticles and carbon nanotubes have been reported (147-153). However, poor loading, rapid release and large particle size of these reported ICG formulations nullify the advantages associated with their delivery (149, 151). Non-covalent interactions between ICG and nanoparticle matrix is the primary mechanism for physical encapsulation of ICG in these reported nanoparticles system. Non-covalent interactions are weak in nature which results in the moderate ICG loading and rapid release upon in vivo dilution.

To address these limitations, we have covalently conjugated amino derivative of ICG to the pendant carboxylic group of a biocompatible and biodegradable amphiphillic copolymer. ICG conjugated amphiphillic polymer self-assembled into micelles of 50 nm with improved ICG loading and little premature ICG release. ICG conjugated micelles were evaluated for their cellular uptake and photodynamic toxicity. In vivo biodistribution and tumor accumulation of ICG conjugated micelles was evaluated using non-invasive NIR fluorescence imaging. Finally, the efficacy of PT of ICG conjugated micelles was studied after light irradiation in A375 human melanoma tumor in athymic nude mice.

3.2 Materials and Methods

3.2.1 Materials

2, 2-Bis(hydroxymethyl) propionic acid, methoxy poly(ethylene glycol) (mPEG,

36

Mn = 5000), 8-diazabicycloundec-7-ene (DBU), 1-(3-dimethylaminopropyl)- 3-ethylcarbodiimide HCl, 1-hydroxybenzotriazole (HOBT) benzyl bromide, acridine orange, dodecanol and diisopropylethylamine (DIPEA) were purchased from Sigma Aldrich (St. Louis, MO) and were used as received. Singlet oxygen sensor green (SOSG) reagent, DMEM medium, Lysotracker red, Calcein AM and propidium iodide were purchased from Invitrogen (Carlsbad, CA). All other reagents were obtained from Sigma–Aldrich (St. Louis, MO) unless otherwise stated and were used as received.

3.2.2 Synthesis of 2-Methyl-2-Benzyloxycarbonyl-Propylene Carbonate (MBC)

Monomer 2-methyl- 2-benzyloxycarbonyl-propylene carbonate (MBC) was synthesized as described previously. Briefly, a mixture of 0.168 mol 2, 2-bis(hydroxymethyl)propionic acid and 0.169 mol potassium hydroxide was dissolved in 125 mL of dimethylformamide (DMF) by heating to 100 °C for 1 h with stirring. 0.202 mol benzyl bromide was added dropwise to the warm solution and stirred at 100 °C for 16 h. At the end of reaction, the solvent was removed under reduced pressure and residue was dissolved in 150 mL of ethyl acetate, washed with water, and dried over $MgSO_4$. Ethyl acetate was removed to yield a crude product, which was recrystallized from toluene to give pure benzyl 2, 2-bis(methylol)propionate. To synthesize 2-methyl-2-benzyloxycarbonylpropylene carbonate (MBC), 0.05 mol benzyl 2,2-bis(methylol)-propionate was dissolved in 150 mL of CH_2Cl_2 containing 25 mL of pyridine, and the solution was chilled to - 78 °C. A solution of CH_2Cl_2 containing 25 mmol triphosgene was dripped into the solution over 1 h. The reaction mixture was stirred for an additional 2h at the room temperature before quenching with 75 mL of saturated aqueous NH_4Cl. Subsequently, the organic layer was sequentially washed with aqueous HCl (1 M, 300

mL) and saturated aqueous NaHCO$_3$ (300 mL), dried with Na$_2$SO$_4$, and evaporated to give 2-methyl-2-benzyloxycarbonylpropylene carbonate (MBC) as a crude product, which was further recrystallized from ethyl acetate to give white crystals.

3.2.3 Synthesis of mPEG-PCC-g- NH$_2$ ICG -g-DC

mPEG-MBC was synthesized by ring-opening polymerization of MBC and mPEG in the presence of 1,8-diazabicycloundec-7-ene (DBU) as a catalyst at room temperature for 3 has described previously (154). The crude polymer so obtained was dissolved in chloroform and purified by precipitation in isopropanol followed by drying under vacuum for 48 h. Protective benzyl group of mPEG-MBC was removed by hydrogenation to obtain free carboxyl group for subsequent conjugation. For this, mPEG-MBC (1 g) was dissolved in a mixture of tetrahydrofuran and methanol (1:1; 12 mL) containing palladium on carbon (Pd/C) (200 mg) and charged with hydrogen at a pressure of 55 psi. Reaction was carried out for 18 h after which Pd/C was removed by filtration and solvent was evaporated under reduced pressure to get poly(ethylene glycol)-block-poly(2- methyl-2-carboxyl-propylene carbonate) (PEG-PCC).

ICG-NH$_2$ and DC were conjugated to the carboxyl groups of PEG-PCC using carbodiimide coupling. For this, PEG-PCC (300 mg) was dissolved in 5 mL of DMF followed by addition of 223 mg of 1-hydroxybenzotriazole (HOBT), 317 mg of 1-(3-dimethylaminopropyl)-3-ethylcarbodiimide HCl (EDC), 340 µL of DIPEA and ICG-NH$_2$ and dodecanol (DC) in DMF were added sequentially to the reaction mixture. The reaction was allowed to proceed for 48 h under nitrogen atmosphere at room temperature. After completion of the reaction, crude product was purified by precipitation in large excess of cold isopropyl alcohol. The precipitate obtained was then

dissolved in DMF, dialyzed against DMF and reprecipitated twice in cold isopropyl alcohol to obtain mPEG-PCC-g-ICG-g-DC.

3.2.4 Characterization of Polymer and Polymer Drug Conjugate

^{1}H NMR spectra were recorded on a Bruker AVANCE III instrument (400 MHz, T = 25 °C) using DMSO-d6 as solvent in chemical shift range of 0−13. For GPC, narrow PEG standards (3600–71000 g/mol) from Polymer laboratories (Santa Clara, CA) were used for generating standard curve and the data was processed using LC Solution ver.1.21 GPC option software.

3.2.5 Formulation Development

ICG conjugated micelles were prepared by nanoprecipitation. Briefly, 30 mg of mPEG-b-PCC-g-NH$_2$ICG-g-DC copolymer was dissolved in acetone (0.5 mL) and added to 4 mL of PBS (pH 7.4). Acetone was then evaporated under reduced pressure followed by centrifugation at 5000 g for 5 min. ICG concentration was determined by comparing absorbance at 790 nm to a standard curve of aqueous ICG-NH$_2$ solution. ICG loading was determined as expressed as the weight ratio between ICG content from standard curve and total weight of polymer ICG conjugate. All loading measurements were performed in triplicate.

3.2.6 Transmission Electron Microscopy

ICG conjugated micelles were visualized using a JEM-100S (Japan) transmission electron microscope (TEM). Micellar suspension was loaded onto copper grid negatively stained with NanoVan®. The grid was visualized at 60 kV with magnifications ranging from 50, 000X to 100,000X.

3.2.7 Spectroscopic Measurements

Absorption spectra of both ICG solution and ICG conjugated micelles at 5µg/ml were recorded between 600-900 nm using a slit width of 5nm. Fluorescent spectra of ICG solution, ICG conjugated micelles and DMSO solution of polymer ICG conjugate was recorded at the wavelength of 640 and 760 nm using a slit width of 5nm using fluorescent spectrometer (Spectramax). 10 % Sodium dodecyl sulphate (SDS) was added to ICG conjugated micelle to disrupt the micelle core and to reverse the quenching of ICG signal. Disruption of micelle core and dequenching by SDS solution was studied both qualitatively and quantitatively using Licor Pearl Imaging System and fluorescent spectrometer (Bruckers) respectively.

3.2.8 Measurement of Singlet Oxygen

ICG conjugated micelles of different concentration (1.0 mL) were irradiated for 3 min at 1.5 W at 808 nm to measure generation of singlet oxygen. Singlet oxygen sensor green (SOSG) equivalent to 32.0 µg/mL was added prior to irradiation to monitor the generation of singlet oxygen. Generation of singlet oxygen was determined by measuring the fluorescence intensity of SOSG at 525 nm using an excitation wavelength of 504 nm. The solution of SOSG without ICG was used as the control. Sodium azide was added during irradiation to quench the generated singlet oxygen and to observe subsequent reduction in SOSG fluorescence intensity.

To determine intracellular generation of singlet oxygen, A375 cells were seeded on a 24 well plate (5 x 104 cells/well) overnight and incubated with ICG conjugated micelles at concentrations of 50 µg for 24 h. After 24 h, cells were washed thrice with PBS and 0.02 ml of dihydroethidium (DHE) (50 µM, PBS) was added to the cells for 30 min at 37 ºC as an indicator of reactive oxygen species. Cells were irradiated with a power density

of 2W at 800 nm for 5 min. Cells were washed with PBS twice and imaged using Zeiss microscope at an excitation wavelength of 550

3.2.9 In Vitro Photodynamic Toxicity

A375 cells plated at a density of 35000 cells/well in 24 well plate were incubated with free ICG (2−15 µg) and ICG conjugated micelles at concentration (15-50 µg) for 24 h. Cells were irradiated with a power density of 2W at 800 for 2 min. Contribution of PDT and PTT effect towards cell killing was studied by using sodium azide and irradiation at 4 °C to block PDT and PTT effect, respectively. Sodium azide was added to cell culture medium at 100 mM to quench singlet oxygen and thereby block PDT effect. Cells were irradiated at 4 °C to maintain constant temperature and nullify the PTT effect. Laser only, ICG solution and ICG conjugated micelles without radiation exposure were used as a positive control. After 24h of irradiation, MTT assay was performed to calculate the cell viability. The absorbance was measured at 560 nm using a microplate reader (Epoch, BioTek Instruments Inc., Winooski, VT).

Cell cytotoxicity was also determined after 24 h of cellular uptake of ICG conjugated micelles and ICG solution. Cells were incubated with ICG solution and ICG conjugated micelles for 24 h followed by three PBS washings. Cells were exposed to NIR radiation with a power density of 2W at 800 for 2 min followed by MTT assay after 24 h. Viability staining was also performed on A375 cells using Calcein AM/ propidium iodide. A375 cells were incubated with free ICG solution at 8 µg and ICG conjugated micelles at 30 µg in 24-well plates for 24 h. After 24 h incubation following NIR irradiation, medium was replaced with 1 mL PBS solution containing 4 µL of calcein AM stock solution (1 mg/mL in DMSO) and 2 µM propidium iodide solutions for 30 min. Subsequently, each well

was washed once with PBS and live/dead cells were imaged using Zeiss fluorescent microscope.

3.2.10 Cell Uptake Studies

A375 cells were seeded in 4 well chambers slides (2×10^4 cells/well) overnight and ICG conjugated micelles were added for 24 h at 37 °C to monitor the uptake of ICG conjugated micelles. Cells were incubated with the media containing LysoTracker Red DND-99 (4 µL of 1 mM DMSO solution in 40 mL of media) for 30 min in the dark prior to washing. After washing thrice with PBS, cells were fixed with 4% paraformaldehyde in PBS at room temperature for 15 min and then counterstained with DAPI. Cellular uptake and co-localization of ICG conjugated micelles in lysosomes was imaged using a confocal microscope.

For quantification of cellular uptake, A375 cells were seeded in 6-well plates (3×10^5 cells/well) and cultured with ICG conjugated micelles (containing 20 µg ICG) and free ICG (20 µg) in DMEM medium at 37 °C for 4h, 8h and 24 h. At the end of incubation periods, the cells were washed with PBS thrice and lysed using a lysis buffer. Cellular uptake of ICG was quantitatively measuring fluorescence intensity of 1:1 dilution of cell lysate with DMSO at 820 nm upon excitation at 780 nm and calculated by comparing with standard curve of ICG.

3.2.11 In vivo Imaging

All animal experiments were performed in accordance with the NIH animal use guidelines and protocol approved by the Institutional Animal Care and Use Committee (IACUC) at the University of Nebraska Medical Center (UNMC, Omaha, NE). Athymic nude mice (6−8 weeks old, weight around 20 g) were used as a tumor model for ex vivo imaging. Mice were subcutaneously injected with 4 million A375 melanoma cells

suspended in 200 µL 1:1 serum-free media and Matrigel (BD Biosciences, CA). Mice were randomly divided into free ICG and ICG conjugated micelles group upon reaching a tumor volume of 500-1000 mm^3. Formulations were administered to mice via the tail vein at a dose of 2 mg/kg and whole body imaging was performed using LI-COR Biosciences's pearl small animal imaging system at 1, 3, and 24 h after dosing. The average fluorescence intensity corresponding to tumors was calculated and compared between ICG conjugated micelles and ICG solution groups. To determine the organ distribution, mice were sacrificed after 24 h of injection, and organs including heart, liver, spleen, lung, kidney, and tumor were imaged using LI-COR Biosciences's pearl small animal imaging system with 800 nm filter. The average NIRF intensity for each organ was calculated for ICG conjugated micelle and ICG solution groups.

3.2.12 In vivo efficacy study

For efficacy studies, athymic nude mice (8−9 weeks old, weight around 24 g) were used. Mice were subcutaneously injected with 4 million A375 melanoma cells suspended in 200 µL 1:1 serum-free media and Matrigel (BD Biosciences, CA). Animals were randomly divided into three groups when tumor volume was 200 mm3. Group 1 was kept as the control and received normal saline, group 2 and 3 received ICG solution (10 mg/kg) followed by irradiation at 1 and 6 h respectively and group 4received ICG micelles equivalent to ICG (10 mg/kg). Tumors were irradiated with laser at power density of 2 W for 5 min after 6 hours except for group 2. Tumor sizes were measured after every two days using digital vernier calipers in two perpendicular axis and reported as tumor volume (V = 1/2[a × b2], a = longest axis, b = shortest axis). Body weights were measured every 2 days. Tumor tissues were excised and weighed at the end of study.

3.2.13 Statistical Analysis

The significance of the results was assessed by Student's t-test. The p-values lower than 0.05 were considered as statistically significant.

3.3 Results

3.3.1 Synthesis and characterization of NH$_2$ ICG

ICG does not have functional group for its conjugation to the polymeric backbone and hence amino derivative of ICG was synthesized by Dr. Natarajan's group as reported earlier [1]. Synthesis and purity of ICG was confirmed by the LC-MS where a single peak of 675 Da of amino ICG was observed (**Figure 3.1**).
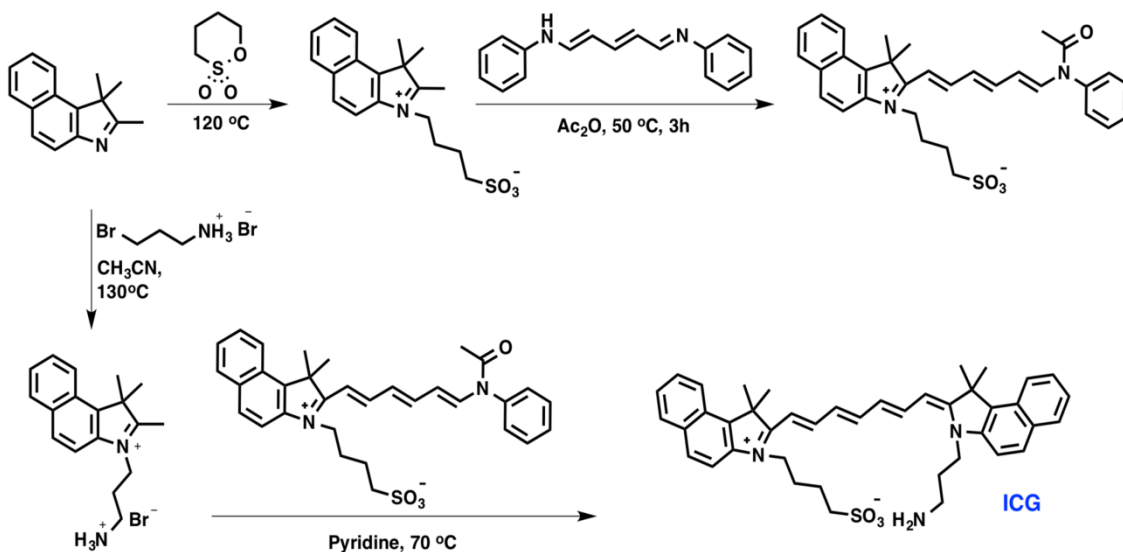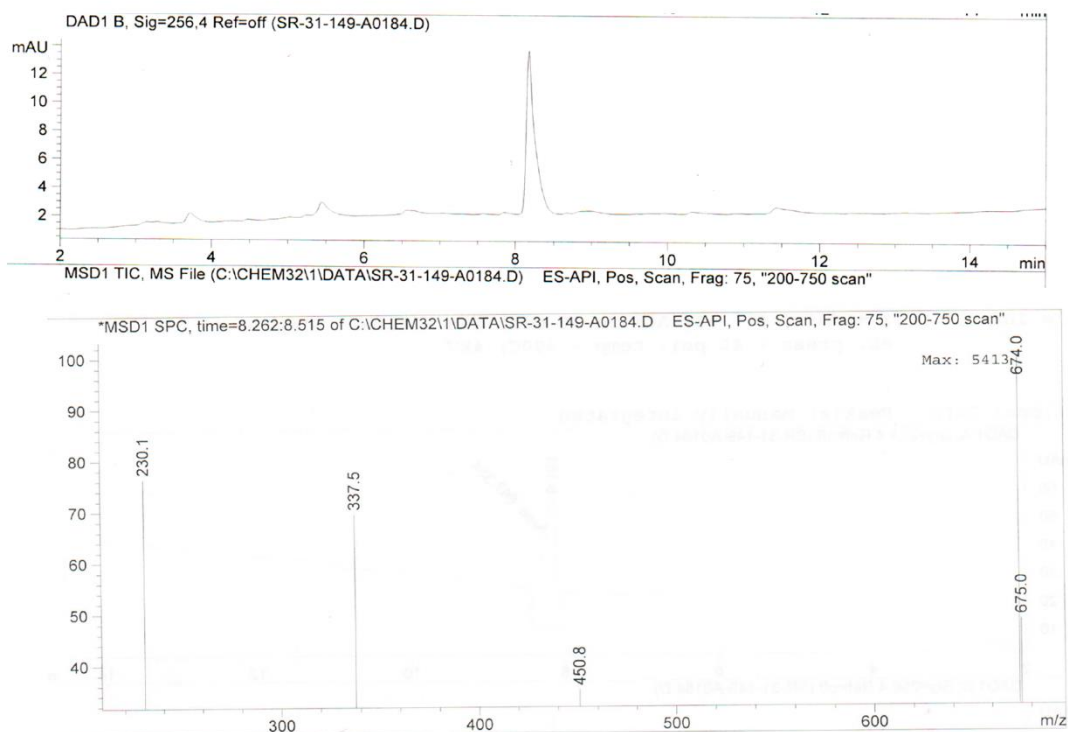
Figure 3-1.   Synthesis and characterization of amino ICG

(A) Schematic presentation of synthesis of ICG. (B) ICG liquid chromatography trace for purity was generated on an Agilent 1200 series system with UV detector (256 nm) using 5-95% acetonitrile as eluent at a flow rate of 1 ml/min and 675 *m/z* was obtained using Agilent 1260 LC-MS-ELSD system (bottom).

3.3.2 Synthesis and characterization of mPEG-b-PCC-g-indocyanine green -g-dodecanol (mPEG-PCC-g- NH₂ ICG -g-DC)

Synthesis of mPEG-b-PBC polymer was confirmed by ^{1}H NMR and GPC (Figure 3.3). The polymerization and structure confirmation of mPEG-b-PBC polymer was determined by the peaks at δ 1.2 (CH_3 in bicarbonate (BC) unit), δ 3.6 (CH_2 in PEG), δ 4.3(CH_2 in BC main chain), δ 5.2 (CH_2 in BC side group), and δ 7.3 (phenyl ring). Using the peak integral areas of PEG CH_2 groups at δ 3.6 and those of the five phenyl ring protons in BC at (δ = 7.30 ppm) the number average molecular weight (Mn) of PEG-b-PBC was 14500 Da (Figure 3.3A). The polymer molecular weight was 11210 Da with a polydispersity of 1.14 as determined from GPC standard curve of narrow PEG standards (**Figure 3.4A**). The Pd/C catalyzed hydrogenation of benzyl group was confirmed by disappearance of peaks at δ 5.2 (CH_2 in BC side group) and δ 7.3 (phenyl ring). In addition, a peak at δ 13 was observed indicating the presence of carboxyl group after removal of protective benzyl group (**Figure 3.3B**). ICG-NH₂ and DC were coupled to PEG-PCC using EDC/ HOBT coupling chemistry and conjugate was purified.

3.3.3 Formulation development

ICG conjugated polymer was formulated as micelles by nanoprecipitation method. Particle size of the micelles was determined by transmission electron microscope (TEM) imaging of vanadium based negative stained micelles which was approximately in the range of 30-50 nm (**Figure 3.4B**). TEM images showed spherical micelle with narrow size distribution. Drug loading of ICG conjugated micelles was 10.2 % by absorption spectroscopy at 790 nm. Spectroscopic characterization of ICG solution and ICG conjugated micelles was performed to study the effect of conjugation and micelles formulation of ICG. Absorption spectrum of ICG conjugated micelles indicated red shift

of 10 nm upon conjugation and formulation of micelles (**Figure 3.5A**). Increasing concentration of ICG is associated with self-quenching which resulted in decrease of NIR fluorescence intensity. Compared to ICG solution, close packing of ICG molecules within the core of micelles resulted in self-quenching and significantly decrease in the fluorescence intensity of ICG micelles (**Figure 3.5B & C**). Increase in the fluorescence intensity of polymer-ICG conjugate in the organic solvent confirmed that quenching within the core of micelles resulted in decrease of fluorescence intensity of ICG conjugated micelles (**Figure 3.5D**). Micelles upon interaction with serum and cellular proteins undergo disassembly and lose their integrity. Surfactants like SDS have been shown to interact with the core of micelles and disrupt the integrity of micelles. Addition of 10 % SDS to ICG micelles disrupted the core of micelles with two fold increase in the fluorescence intensity of ICG conjugated micelles (**Figure 3.5 E & F**). Disruption of micelles and dequenching effect of SDS was also confirmed by Licor Pearl imaging system.
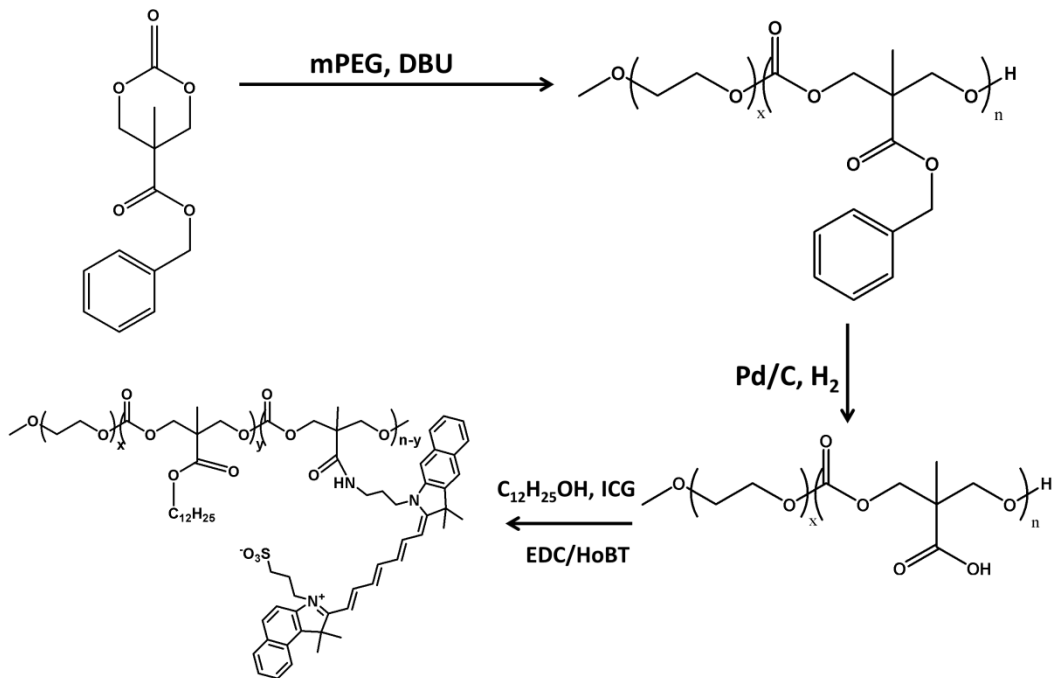
Figure 3-2. **Schematic representation of synthesis and characterization of ICG polymer conjugate**

(I) Ring opening polymerization of monomer 2-Methyl-2-Benzyloxycarbonyl-Propylene Carbonate using DBU as catalyst (II) Catalytic hydrogenation of PEG- PBC (III) Carbodiimide coupling of amino ICG to pedant carboxyl groups of PEG-PCC

A
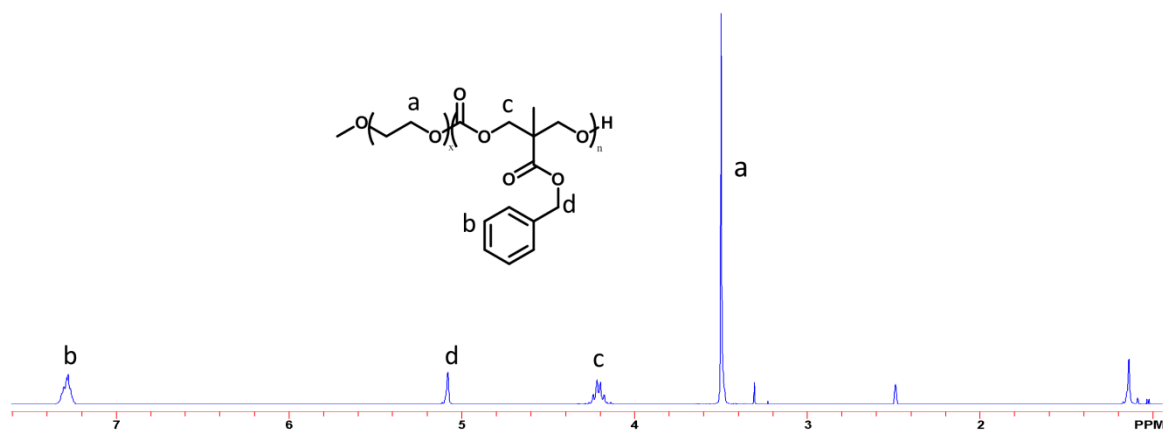
B
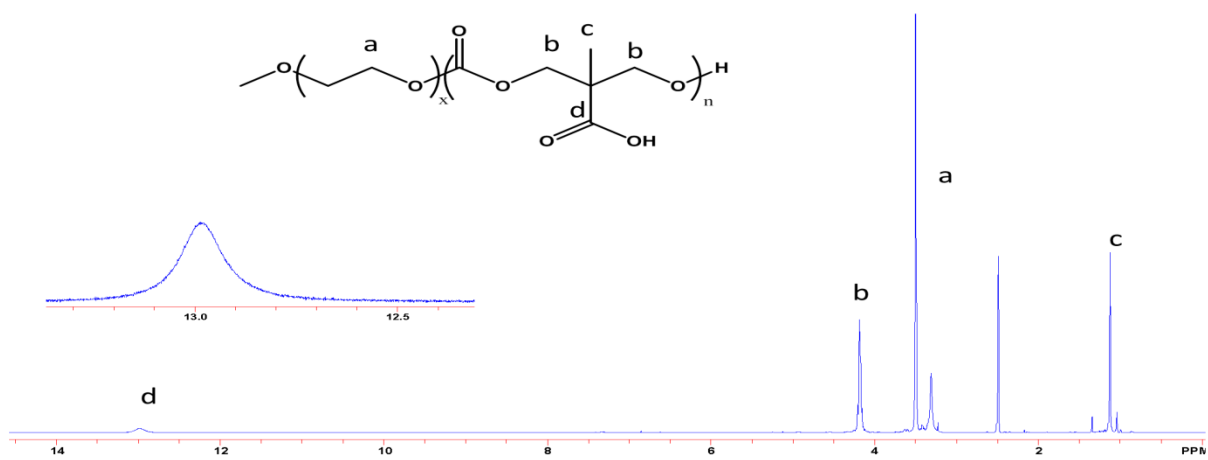
Figure 3-3. ^{1}H NMR of polymers (A) PEG-PBC and (B) PEG-PCC in DMSO-d6.

49

	NMR	Mw (GPC)	Mn (GPC)	PDI
PEG MBC$_{37}$	14500	11216	9802	1.144

B
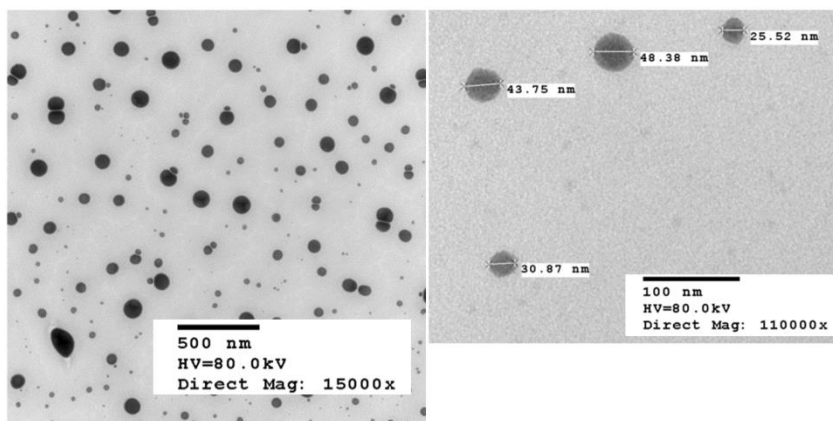
Figure 3-4.   Characterization of synthesized polymer and ICG conjugated micelles.

(A) Characterization of weight average molecular weight, number average molecular weight and polydispersity index using GPC and ^{1}H NMR. (B) TEM image of ICG conjugated micelles which were stained with vanadium based negative staining. Size of ICG conjugated micelles was approximately 30-50 nm as determined by TEM image.

3.3.4 Generation of singlet oxygen

Generation of singlet oxygen in solution was determined by measuring the fluorescence of SOSG upon irradiation of ICG conjugated micelles. Intracellular generation of singlet oxygen was determined using cell permeable DHE (155). Control group showed a faint background signal compared to ICG conjugated micelles, but quenching of singlet oxygen with ROS scavenger, sodium azide reduced red fluorescence (**Figure 3.6A**). There was concentration dependent increase in SOSG fluorescence intensity upon irradiation and exhibited 8 fold increase in the fluorescence intensity at 50 µg compared to the control, but quenching with sodium azide reversed SOSG fluorescence intensity to background levels (**Figure 3.6B**), confirming the specificity of generation of singlet oxygen.

3.3.5 Cell cytotoxicity and cell uptake studies

ICG upon excitation with NIR light at 800 nm generates reactive oxygen species and local heat. ROS results in lethal DNA and protein damage which leads to cell death. Cells were exposed to ICG solution and ICG conjugated micelles for 24 h followed by NIR light exposure at 2W for 2 min. ICG solution caused significant cytotoxicity with 50 % and 5 % cell viability at 8 and 16 µg respectively (**Figure 3.7A**). Correspondingly, ICG conjugated micelles were cytotoxic at 30 and 50 µg with 23 and 13 % viability respectively with no toxicity in ICG micelles alone or laser alone group (**Figure 3.7B**). To further study the contribution of PTT and PDT towards cell killing, cells were radiated at 4 °C or in the presence of 100 mM ROS scavenger sodium azide which blocks the cytotoxic effect of ROS. Sodium azide completely reversed the cytotoxic effect of ICG solution at 8 µg but failed to reverse the cytotoxicity at 15 µg. Reversal of PTT effect

did not alter the cytotoxicity of ICG solution demonstrating PDT as major mechanism of cell killing. This was further confirmed by partial reversal of cytotoxicity at 15 µg when both PDT and PTT effect after radiation of ICG solution was blocked. Contrastingly, PTT effect is the major mechanism of ICG conjugated micelles cytotoxicity as evident from the reversal of cytotoxicity of ICG micelles upon irradiation at 4°C. Calcein AM/ Propidium iodide staining was applied to visually evaluate and observe live dead cells after PT. Fluorescent images corroborated the quantitative findings of MTT assay with PDT and PTT as major mechanism of cytotoxicity for ICG solution and ICG micelles respectively (**Figure 3.7 C**). Moreover, PTT effect alone by ICG micelles does not completely kill the cells as evident from green viable cells (Figure 5C, NaN3 group). PTT effect alone only slows down proliferation of cancer cells and it is combination of PTT and PDT effect that effectively kills cancer cells (**Figure 3.7C, micelles**). To further explain this anomaly in the cytotoxicity mechanism of ICG solution ICG conjugated micelles, we determined the cellular uptake of ICG in solution and micelle group using z stacks imaging by confocal microscope. As reported previously for various nanocarriers, cellular uptake of ICG micelles was by endocytic mechanism (**Figure 3.8D**). However, there is significant difference in the cell internalization of ICG solution and ICG conjugated micelles as shown in orthogonal cell uptake images (**Figure 3.8A & B**),. Solution exhibits much higher ICG cellular uptake (green staining) as compared to ICG conjugated micelles. This finding was affirmed by the quantitatively measuring the cellular uptake of ICG. Cellular uptake of free ICG was 5 fold higher as compared to ICG micelles (**Figure 3.8C**) confirming the confocal images. Cytotoxicity of ICG was also studied by removing the cell culture medium containing ICG after 24 h

exposure of ICG solution and ICG conjugated micelles. Absence of ICG in the cell culture medium did not affect the cytotoxicity of free ICG group as compared to ICG conjugated micelles (**Figure 3.9A**). Removal of ICG conjugated micelles from cell culture medium completely repealed the phototoxicity of micelles group. These studies suggest that both solution and micelles group exhibit concentration dependent strong phototoxicity and intracellular accumulation of ICG solution and ICG conjugated micelles determine the mechanism of cytotoxicity. ICG micelles also showed time dependent toxicity with enhanced cell killings upon NIR radiation for longer period of times (**Figure 3.9B**).
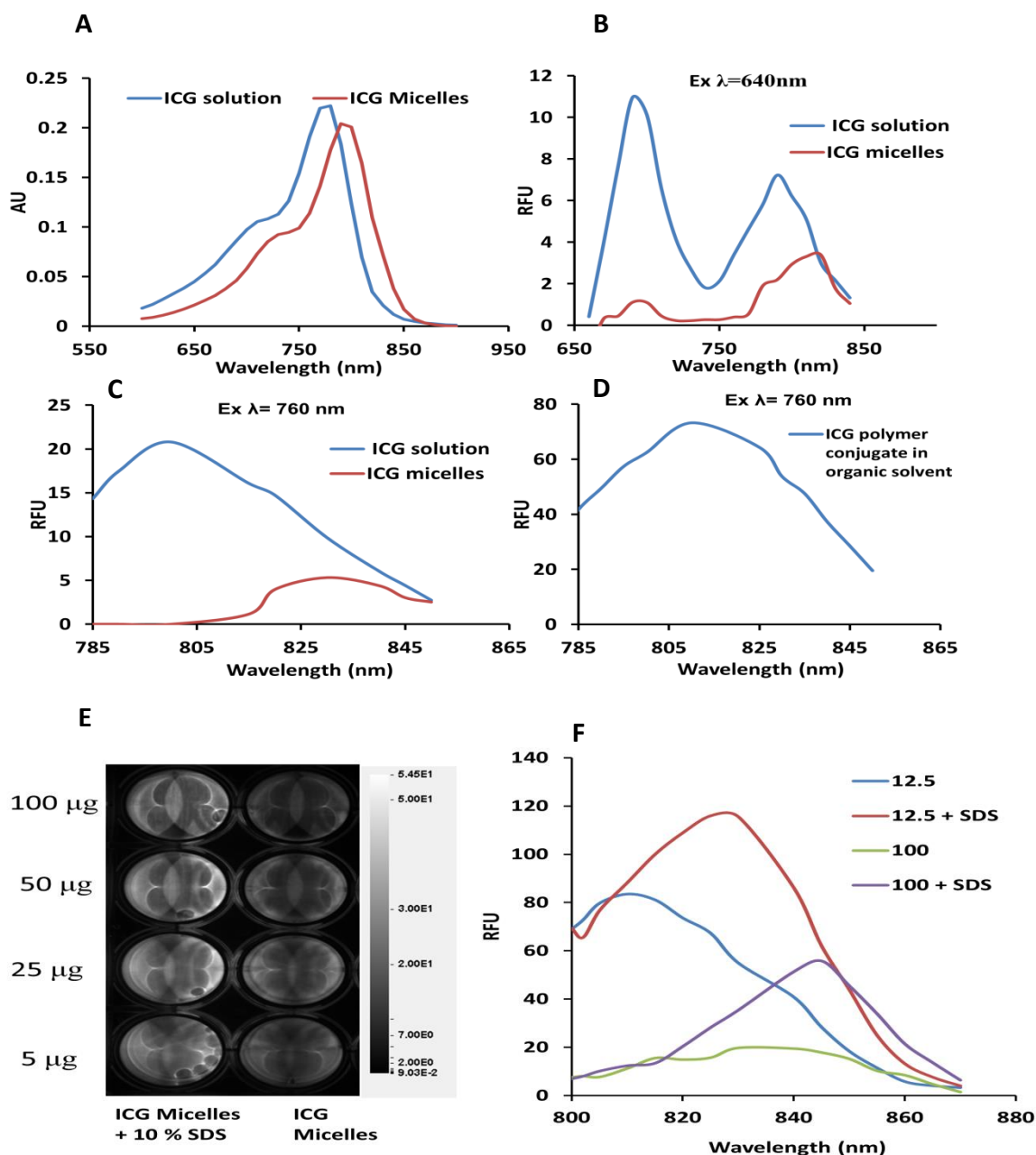
Figure 3-5.   Characterization of spectroscopic properties of ICG solution and ICG conjugated micelles.

(A) Absorption spectrum (B &C) Fluorescence spectrum upon excitation at 640 nm and 760 nm respectively (D) Fluorescence spectrum of polymer ICG conjugate in organic solvent upon excitation at 760 nm (E) Near infra-red fluorescence image of ICG micelles with 10 % SDS solution (right) or ICG micelles (left) at 5-100 µg (F) Quantitative fluorescence measurement of ICG micelles with 10 % SDS solution and ICG conjugated micelles alone at 12.5 and 100 µg.

A
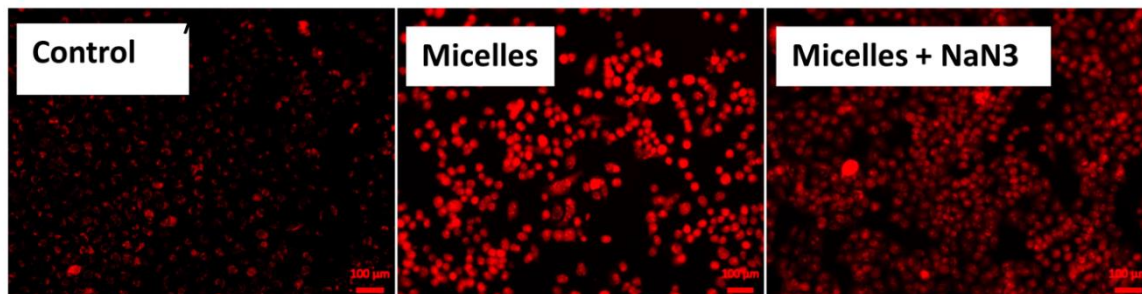
B
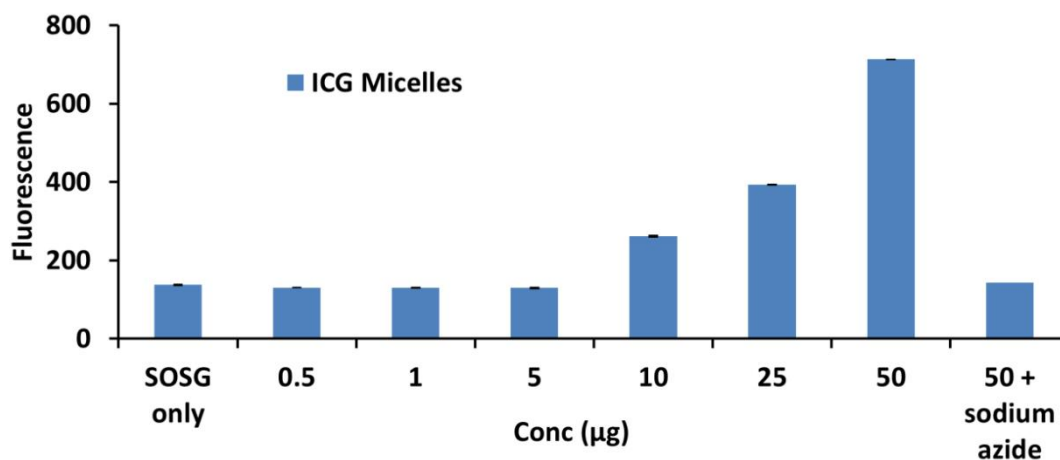
Figure 3-6.   Generation of singlet oxygen from ICG conjugated micelles.

(A) Representative fluorescent images of A375 cells treated with ICG conjugated micelles using DHE staining for singlet oxygen detection at 20 and 50 µg and using NaN3 pretreatment (800 nm, 2 W, 5 min). (B) Quantitative estimation of generation of singlet oxygen upon radiation of ICG conjugated micelles in solution using singlet oxygen sensor green. Data are shown as mean ± SD (n=3)
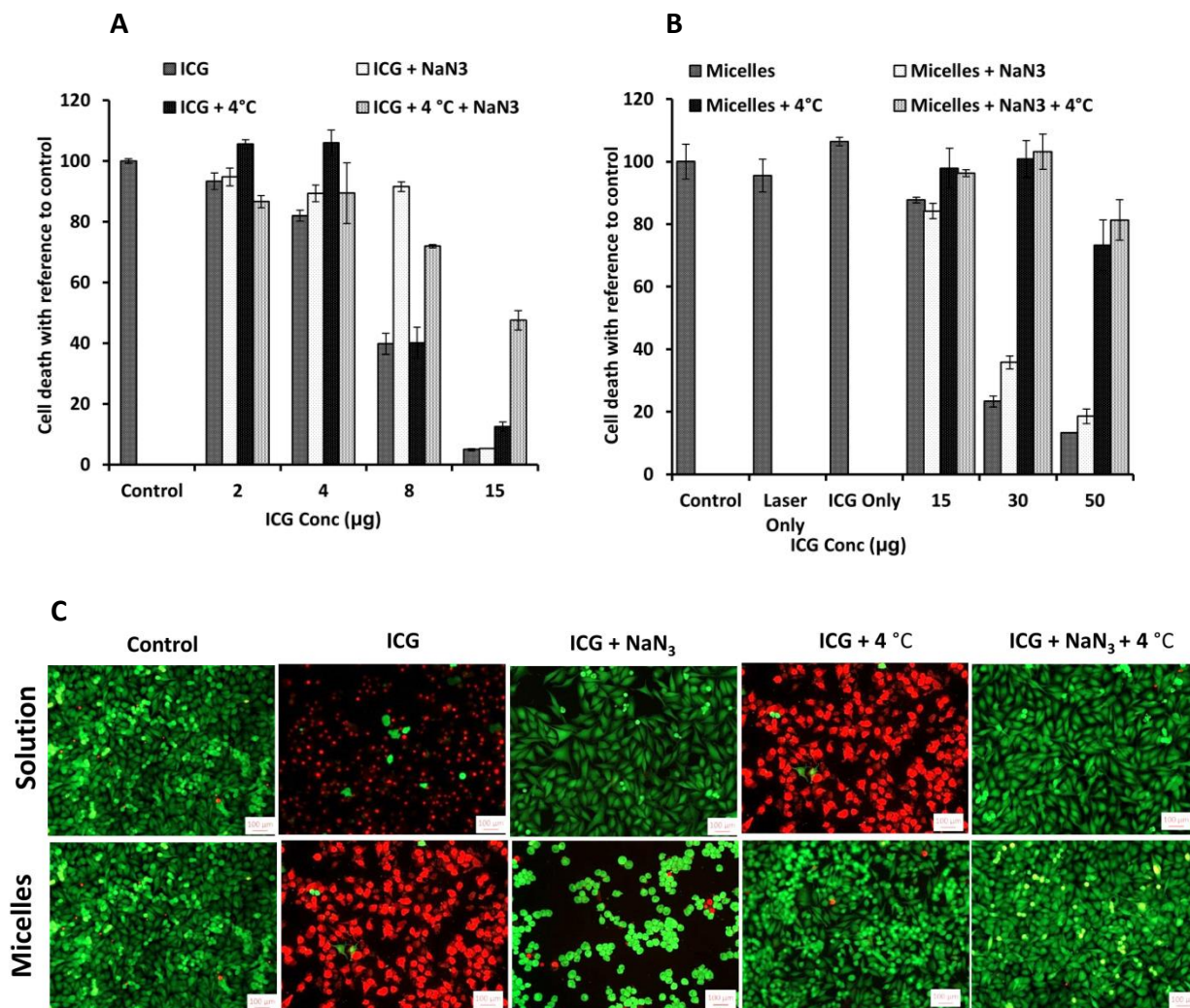
Figure 3-7.   Quantitative measurement and assessment of mechanism of cytotoxicity after NIR radiation.

Cell cytotoxicity of (A) ICG solution and (B) ICG conjugated micelles in A375 cells at 24 h. Data are presented as mean ± SD (n=3) (C) Fluorescent images of live dead staining after NIR radiation of ICG solution and ICG conjugated micelles in A375 cells alone, in the presence of 100 mM sodium azide, at 4°C and at 4°C in the presence of 100 mM sodium azide. Calcein AM stains live cells as green and propidium iodide stains dead cells as red.
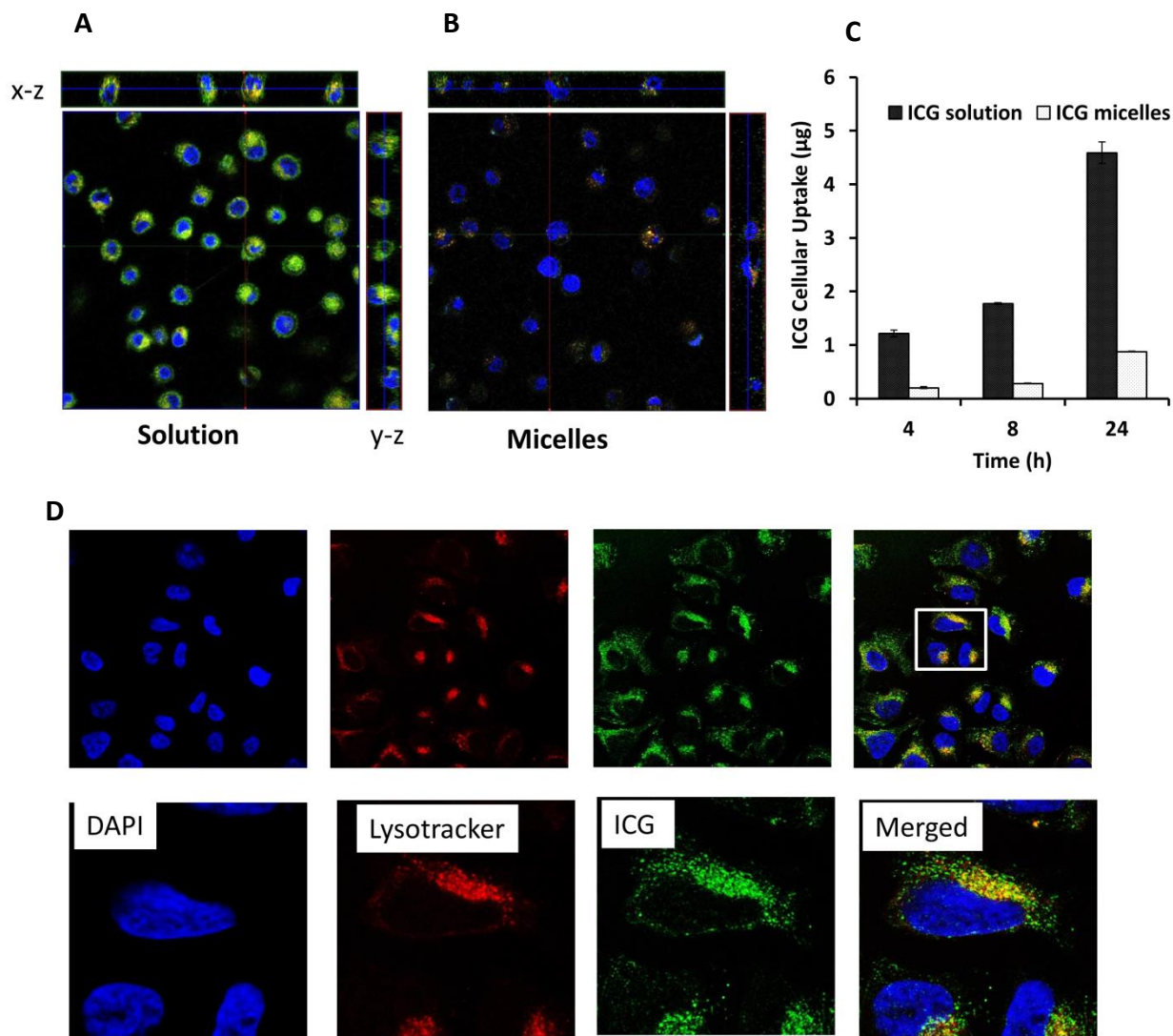
Figure 3-8.   Cell uptake study of ICG conjugated micelles and its quantification.

Orthogonal projections of confocal sections of cellular uptake of (A) ICG solution and (B) ICG conjugated micelles showing minimum cellular uptake of ICG micelles at midpoint of cross sections after 24 h incubation at 37 C. (C) Quantification of cellular uptake of ICG solution and ICG conjugated micelles after 4, 8 and 24 h incubation of A375 cells with 20 µg equivalent of ICG. (D) Confocal FL images of A375 cells and subcellular localization of ICG conjugated micelles after 4 h incubation. Nuclei were stained with DAPI (blue), lysosomes were stained with Lysotracker (red), green fluorescence was derived from ICG solution and ICG conjugated micelles and yellow represents co-localization of lysosomes and ICG.
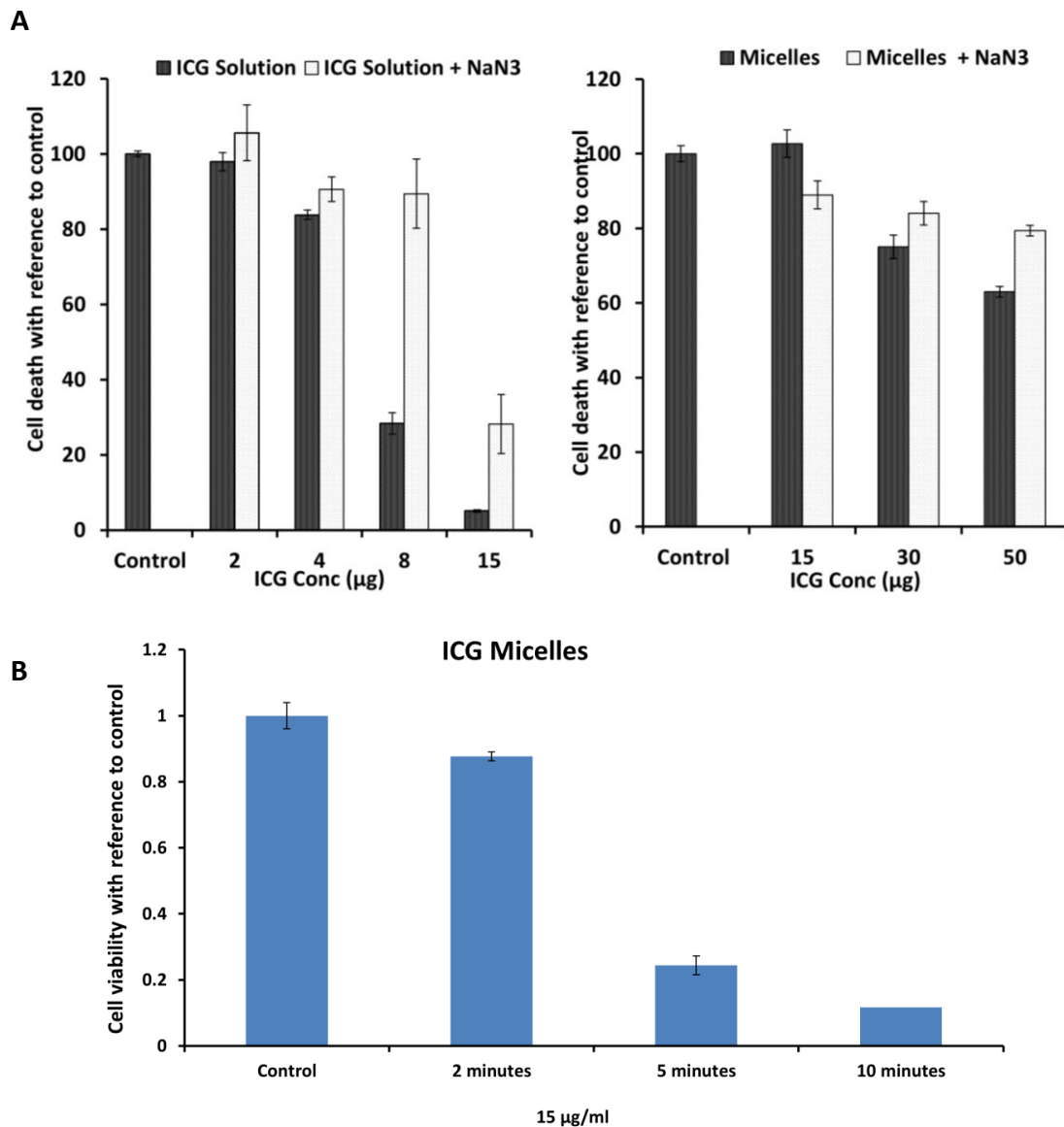
Figure 3-9.   Cytotoxicity assay of ICG conjugated micelles.

 (A) Quantitative measurement of cytotoxicity of free ICG and ICG conjugated micelles with replacement of the cell culture medium containing free ICG and ICG micelles after 24 h with fresh medium followed by NIR radiation for 2 min at 2W. (B) Exposure dependent cytotoxicity of ICG conjugated micelles against A375 cells as analyzed by MTT assay. A375 cells were incubated with ICG conjugated micelles equivalent to 15 µg for 24 h, followed by 2, 5, and 10 min photoirradiation at 800 nm.

3.3.6 In vivo and ex vivo NIR imaging

Increase in systemic circulation and enhanced tumor accumulation of ICG conjugated micelles was confirmed by in vivo whole body NIR fluorescence imaging. As shown in **Figure 3.10A**, ICG conjugated micelles demonstrated significantly higher whole body signal at 24 h due to prolonged circulation and limited renal elimination of ICG conjugated micelles. In tune with the whole body levels, ICG conjugated micelles also exhibited enhanced tumor accumulation at 6 and 24 h as compared to ICG solution (**Figure 3.10A**). The mean fluorescence intensity of ICG conjugated micelles in tumor tissue at 24 h is approximately 2.5 fold higher than that of solution (p<<.001). This increase in tumor accumulated indicated preferential tumor accumulation of ICG micelles by EPR effect. In contrast, whole body fluorescence intensity of ICG conjugated micelles was much lower at 1 and 3 h due to the quenching of ICG signals. Quenching of the ICG signal confirmed the close packing of ICG within the core of micelles indicating excellent in vivo kinetic stability of micelles against plasma proteins and dilution. Organ biodistribution by ex vivo imaging showed that ICG conjugated micelles efficiently accumulated in the tumor with fluorescence intensity signal equivalent to highly perfused organ, liver indicating improved tumor accumulation by EPR effect. Kidney isolated from animal receiving ICG solution have highest fluorescence signal, signifying rapid renal elimination of ICG and short plasma half-life. Ex vivo imaging of vital organs reaffirmed the in vivo findings of reduced clearance, enhanced biodistribution and tumor accumulation of ICG conjugated micelles (**Figure 3.10 C&D**).
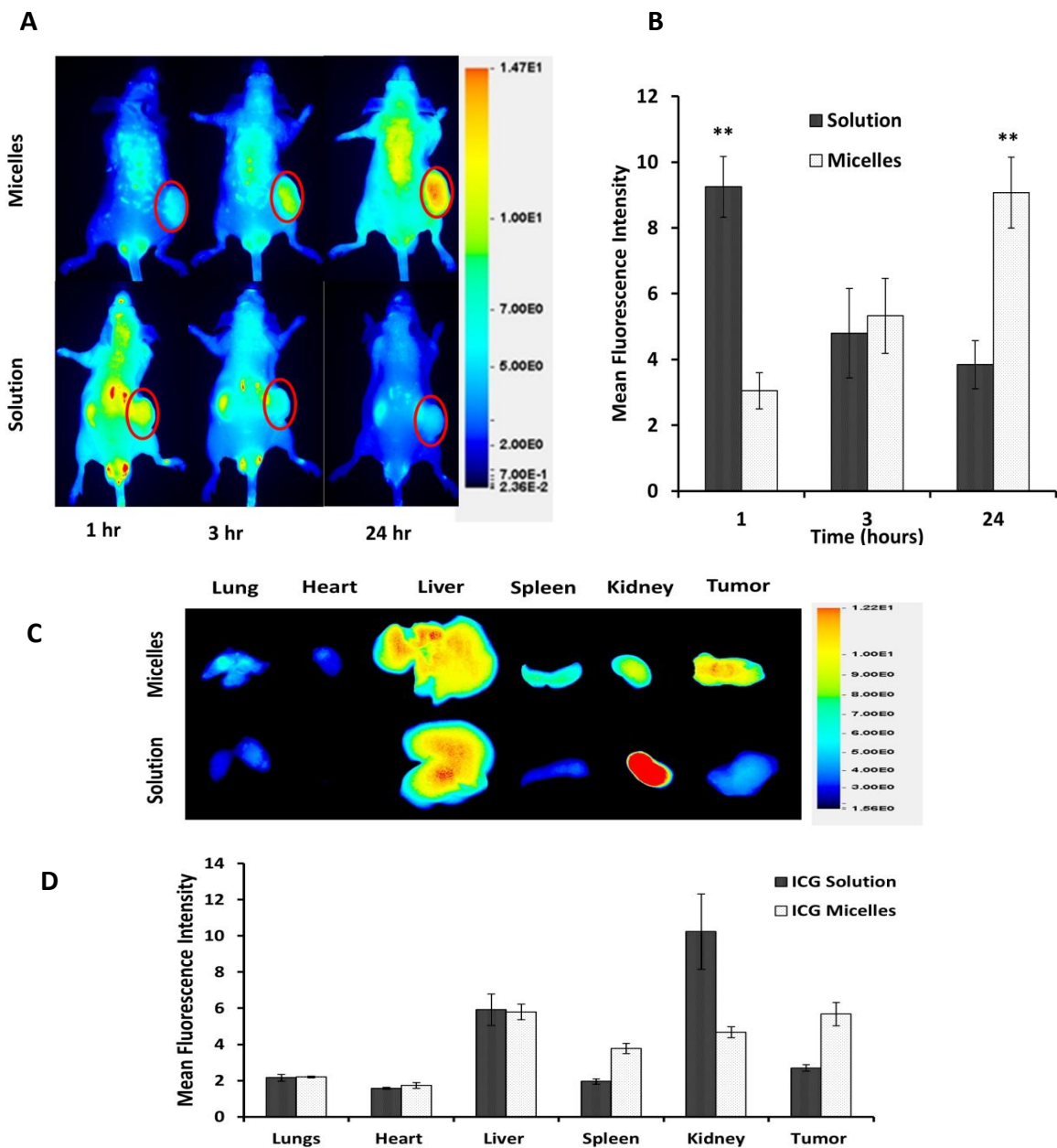
Figure 3-10.   In vivo NIR fluorescence imaging in A375 subcutaneous melanoma model.

NIR fluorescence imaging of athymic nude mice of ICG conjugated micelles and ICG solution at 800 nm spectral channel. (A) Representative image with ellipse indicating tumor accumulation of ICG. (B) Mean fluorescence signal counts of tumor accumulated ICG as calculated by ellipse representing region of interest. Data are presented as mean ± SD (n=5) (C) Ex vivo fluorescent images of peripheral organs 24 h after ICG injection (D) Mean fluorescence signal counts of major organs of ICG solution and ICG conjugated micelles group. Data are presented as mean ± SD (n=3)

3.3.7 Effect of phototherapy on tumor growth

Encouraged by the *in vitro* efficacy and *in vivo* NIR fluorescence biodistribution data, we tested the efficacy of PT of ICG formulations in A375 human melanoma model in athymic nude mice. After systemic administration of ICG solution and ICG conjugated micelles, tumors were irradiated with 800 nm laser for 5 min at 2W after 6 h post injection along with radiation of ICG solution group at 1 h. Mice receiving ICG conjugated micelles showed complete eradication of the tumor mass next day with no tumor relapse up to 55 days (**Figure 3.11A**). Conversely, mice receiving ICG solution followed by laser irradiation did not exhibit any tumor shrinkage or reduction.. Tumor growth in ICG solution group did not differ from the control group indicating inefficient tumor accumulation of ICG for effective phototherapy. To demonstrate the poor efficacy with ICG solution, irradiation of tumor also was performed at 1 h after the systemic administration of ICG solution. In this group half of the mice responded with no signs of tumor relapse upto 9 days whereas half mice showed only slight reduction in tumor volume with no difference as compared to control at the end of study. It is important to note that mice did not show any tumor relapse upto 55 days whereas in solution group (1 h radiation) all mice had tumor at the end of 17 days which suggest significant improvement in tumor accumulation ICG conjugated by formulation it as ICG conjugated micelles. Mouse body weight was measured every 2 days to observe any signs of toxicity due to radiation. Mice receiving radiation did not show any significant drop (less than 5 % reduction) in the body weight over the course of study indicating that PT was well tolerated (**Figure 3.11B**). Post euthanasia, tumors were excised which confirmed that PT with ICG conjugated micelles completely eradicated the tumor with little difference between control and ICG solution group (**Figure 3.11 C & D**).
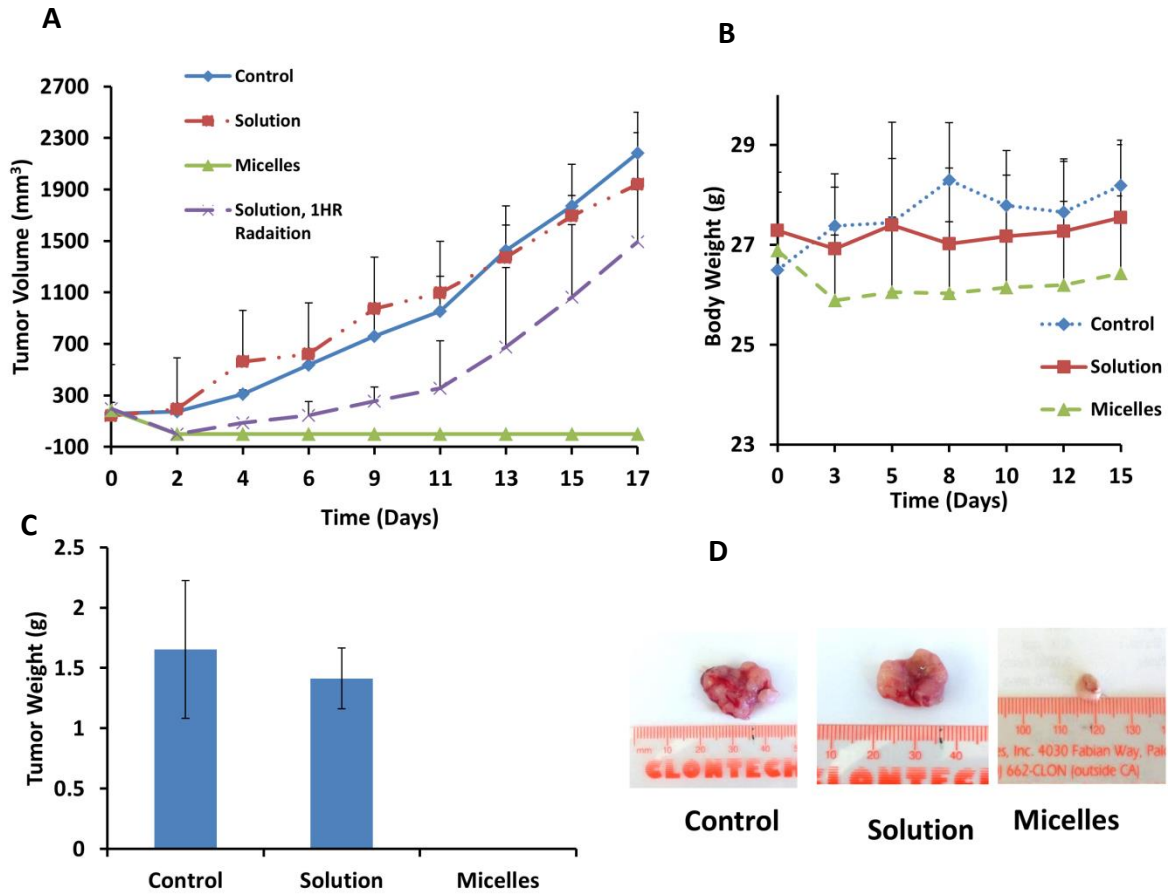
Figure 3-11.   In vivo efficacy of phototherapy in A375 subcutaneous melanoma model.

In vivo efficacy of phototherapy in A375 xenograft melanoma model after NIR irradiation at 800 nm and 2 W for 5 mins, 6 h post i.v. administration. (A) Tumor volume growth curves of control, ICG solution and ICG conjugated micelles as measured by vernier calipers. Data are presented as mean ± SD (n=6). (B) Total body weight of tumor-bearing mice throughout the course of treatment to observe toxicity. (C) Weight measurement of excised tumors for all the groups. Data are presented as mean ± SD (n=6) (D) Representative image of the excised tumor in control, free ICG and ICG conjugated micelles groups at the end of 17 days.

3.4 Discussion

Melanoma originated from melanocytes is the most aggressive form of skin cancer (156). Although systemic chemotherapy remains the mainstay of treating melanoma, development of resistance and dose limiting toxicity restrict the efficacy of chemotherapeutics. PT, a combination of inert photosensitizer and light of particular wavelength has been demonstrated to produce highly cytotoxic effects with little toxicity. ICG with large safety dose and absorption in the NIR range is an excellent photosensitizer but with limited vascular extravasation and tumor accumulation. Numerous nanocarriers have been reported to improve the plasma circulation high life and tumor accumulation of ICG for phototherapy (157). Saxena et al. reported polymeric ICG nanoparticles with 350 nm size, ICG loading of 0.20 % w/w and 78% release within 8 hours (149). Liposomes formulation of ICG has also been recently reported with insignificant improvement of its half-life due to premature ICG release (151). Adsorption and π-π interaction of ICG with silica nanoparticles and carbon nanotubes have also been reported respectively (152, 153). However, weak non-covalent interactions between nanocarriers and ICG could not prevent premature release in vivo and thereby, could not enhance the peripheral organ distribution. Large particle size, poor loading and rapid in vivo release are the major limitations of the ICG loaded nanocarriers (158). Covalent conjugation of ICG derivatives for formulation has been reported previously to enhance loading and reduce the release but the particle size of these nanoparticles lie on the upper limit of the preferred size range for in vivo applications (150, 159). In this study, we have formulated biodegradable ICG conjugated micelles with particle size of 50 nm, increased ICG loading and little premature release for photodynamic therapy of melanoma. Amphiphilic copolymer with pendant carboxyl groups was synthesized and

characterized using mPEG as macroinitator. Data from ^{1}H NMR and GPC characterization of PEG-MBC and PEG-PCC confirmed the synthesis of copolymer with desired molecular weight and narrow PDI distribution (Figure 3.3 and 3.4). ICG-NH$_2$ was conjugated to the pendant carboxyl group using EDC/HOBT coupling chemistry with conjugation efficiency of around 80% (Figure 3.2). Dodecanol was conjugated to enhance the hydrophobic interaction as well as to counter negative contribution towards micelle stability from hydrophilicity and ionic charge of remaining pendant carboxyl group. Attachment of multiple DC chains facilitated the hydrophobic interaction within the core of micelles as well as improved the self-assembly of micelles (160).

Micelles prepared by nanoprecipitation were sub 50 nm in size (Figure 3.4) which is important for efficient tumor penetration by enhanced extravasation and slow tumor clearance (161, 162). Moreover, the high PEG coverage of ICG conjugated micelles surface will lead to brush confirmation enhancing the circulatory half-life as well as stabilization of micelles core (163). Stability of ICG conjugated micelles was also evident from the strong self-quenching of fluorescent signal as ICG molecules were closely packed within the core of micelles (Figure 3.5 B & C). Micelles stability was also studied by partial recovery of ICG fluorescence after addition of SDS as destabilizing agent (Figure 3.5 E & F). Increase in the ICG fluorescence by SDS indicated that SDS can disassemble the micelles for enhanced generation of singlet oxygen. Generation of singlet oxygen upon radiation of ICG conjugated micelles was demonstrated by observing the fluorescence intensity of SOSG and DHE.

Both ICG conjugated micelles and ICG solution exhibited significant phototoxicity with distinct mechanism of action (Figure 3.7 A, B & C). PTT effect is the predominant

mechanism of cytotoxicity by ICG conjugated micelles which can be attributed to the short half-life of singlet oxygen. Singlet oxygen with a radius of action of around 20 nm and a half-life of 40 nanoseconds requires deep intracellular penetration of photosensitizer. However, slow cell uptake of polymeric micelles restricts the uptake of polymer conjugated photosensitizer. Previously, Xu et al. have shown that polymeric micelles are not readily taken up by the cells and in case of physical encapsulation, drug released extracellularly from micelles exhibited rapid cellular uptake (164). Slow release of covalently conjugated ICG molecules along with slow cellular uptake and intracellular accumulation of ICG conjugated micelles limited intracellular penetration of ICG (165-167). Orthogonal images of confocal section of cell uptake studies confirmed the slow uptake of ICG conjugated micelles with substantial lower intracellular accumulation of ICG (Figure 3.8 A, B & C).

In vivo biodistribution and enhanced tumor accumulation by EPR effect was studied by non-invasive NIR fluorescence imaging. Due to quenching of ICG signal, ICG conjugated micelles exhibited significantly lower signal at 1 and 3 h which is in contrasts with all the previous reports of ICG loaded nanocarriers (Figure 3.10 A & B). These reported ICG nanocarriers have shown significant in vitro quenching with little in vivo quenching of ICG fluorescent signal which suggest premature release of ICG or disassembly of nanocarriers during circulation (119, 151, 168). In contrast, we observed significant quenching which confirmed the *in vivo* stability of micelles for at least 3 h probably due to the hydrophobic interaction between the DC within the core of micelles. Such *in vivo* stability of micelles is prerequisite for their prolonged circulation and tumor accumulation by EPR effect (169). Although ICG solution showed better *in vitro* toxicity,

reduction in tumor volume was negligible which can be attributed to inefficient tumor accumulation of ICG. Prolonged circulation of ICG conjugated micelles and their marked tumor accumulation by EPR effect permits marked elevation of tumor temperature and generation of singlet oxygen which is high enough to ablate the tumor (Figure 3.11 A and D).

3.5 Conclusion

In this study, we have designed ICG micelles by covalently conjugating ICG-NH$_2$ to an amphiphillic biocompatible polymer. ICG polymer conjugate self-assembled as 50nm micelles with excellent *in vitro* and *in vivo* stability. ICG conjugated micelles exhibited photothermal mediated phototoxicity due to limited cellular uptake of micelles. *In vivo* NIR fluorescent imaging results showed that the ICG conjugated micelles exhibited excellent *in vivo* stability, prolonged circulation and selective accumulation to the tumor site through the EPR effect. Enhanced accumulation of ICG conjugated micelles significantly improved the therapeutic efficacy of ICG mediated phototherapy with no tumor relapse up to 50 days. These results suggest the ICG conjugated micelles have the can be utilized for phototherapy and imaging of cancer.

CHAPTER 4 SYSTEMIC DELIVERY OF NANOPARTICLE FORMULATION OF NOVEL TUBULIN INHIBITOR FOR TREATING METASTATIC MELANOMA*

4.1 Introduction

Melanoma is the fifth most common cancer in the Unites States and its incidence is increasing by 1.9% annually (170). Due to the high propensity of melanoma for metastasis to lungs, liver, brain and bones, its treatment remains a challenge and is associated with the poor survival rate. While surgery and radiation are the first line therapy for treating localized melanoma, systemic therapy is the cornerstone of clinical management of metastatic melanoma (1). Currently dacarbazine (DTIC) and kinase inhibitors are the FDA approved drugs for the treatment of metastatic melanoma. DTIC, an alkylating agent, exhibits modest efficacy and does not significantly prolong the survival benefit (171) (less than 5 % complete remission), whereas resistance develops invariably upon treatment with kinase inhibitors which restricts the prolonged systemic therapy with these inhibitors (3, 4).

Tubulin inhibitors like vinca alkaloids and taxanes such as paclitaxel have been clinically prescribed as a single agent or in combination with other chemotherapeutic agents (5, 172). Encouraged by the clinical utility of tubulin inhibitors, our collaborator previously reported the synthesis of tubulin inhibitors with antiproliferative IC_{50} in nanomolar range for the treatment of metastatic melanoma (17).

(2-(1H-Indol-5-yl) thiazol- 4-yl) 3, 4, 5-trimethoxyphenyl methanone (LY293), a 5 indole derivative analog, binds to colchicine binding site and does not exhibit clinically prevalent drug resistance mechanism such as multidrug resistance (MDR) protein, breast cancer resistance protein (BCRP) and P-glycoprotein (P-gp) (6, 17, 173).

Like paclitaxel, poor aqueous solubility of LY293 necessitates the use of cosolvent for its systemic delivery (174). Due to poor aqueous solubility, we have previously administered PEG300 solution of LY293 structure analog through intraperitoneal route for efficacy studies in lung metastasis melanoma model (174). LY293 dosed at 25 mg/kg showed better lung metastasis inhibition than standard care of therapy DTIC at 60 mg/kg (Figure 4.1B). In subcutaneous model, after 31 days of treatment LY293 analogues dosed at 25 mg/kg inhibited melanoma tumor growth by 69%; dacarbazine at 60 mg/kg inhibited growth by 52% (Figure 4.1A). However, prolonged administration of drugs using cosolvents as solubilizing agent is associated with hemolysis and acute hypersensitivity reactions which require administration of antihistamines and steroids (175, 176). Additionally, non-specific distribution of tubulin inhibitors like paclitaxel is associated with dose limiting toxicity of myelosuppression and peripheral neuropathy. Biodegradable polymeric nanoparticles are attractive formulation strategies for solubilizing the hydrophobic drug within their core and modulate the drug release (40, 177, 178). Modulation of drug release and preferential accumulation of nanoparticles at tumor through EPR effect reduces dose limiting toxicity like peripheral neuropathy and myelosuppression (179, 180). Amphiphillic poly(ethylene glycol) (PEG) based diblock polyester copolymers of lactide, glycolide and caprolactone have been synthesized for preparing nanoparticles for delivery of hydrophobic drugs (178). We have previously

engineered the hydrophobic core of the polyester component of the copolymer into polyester/polycarbonate component to improve the drug loading of (2-(1H-Indol-5-yl) thiazol-4-yl) 3, 4, 5-trimethoxyphenyl methanone (LY293) (40, 41).

In this study, we have synthesized mPEG-b-P (CB-co-LA) copolymer for effective encapsulation of LY293 in nanocarriers as well as for enhanced tumor accumulation compared to free drug. Synthesized mPEG-b-P (CB-co-LA) diblock random copolymer of lactide and carbonate was characterized and utilized for nanoparticle formulation of LY293. Concentration dependent effect of LY293 loaded nanoparticles on cell cycle and mechanism of apoptosis was studied. Finally, efficacy of LY293 loaded nanoparticles in syngeneic B16F10 lung metastatic melanoma mouse model was evaluated against cosolvent solution of LY293.

4.2 Materials and methods

4.2.1 Materials

2, 2-Bis (hydroxymethyl) propionic acid, methoxy poly (ethylene glycol) (mPEG,Mn = 5000), 8-diazabicycloundec-7-ene (DBU), 1, 5, 7-triazabicyclodecene (TBD) benzyl bromide, 2,2-bis(hydroxymethyl) propionic acid and L-lactide were purchased from Sigma-Aldrich (St. Louis, MO) and used as received. Dulbecco's Modified Eagle Medium (DMEM) medium was purchased from Invitrogen (Carlsbad, CA). All primary antibodies were purchased from Cell Signaling (Beverly, MA). B16F10 mouse melanoma cell line and A375 human melanoma cell line was acquired from American Type Culture Collection and no authentication was performed by us. All other reagents were obtained from Sigma‑Aldrich (St. Louis, MO) unless otherwise stated

and were used as received. Cells were cultured in DMEM supplemented with 10% FBS (Atlanta Biologicals) and 1% antibiotic/antimycotic mixture (Invitogen).

4.2.2 Synthesis and characterization of LY293

LY293 was synthesized by modifying the A ring of SMART series of analogs(8). Briefly, tetrahydrofuran (THF) solution of 3, 4, 5-trimethoxybromobenzene (2.47 mmol) was added to THF solution of *n*-butyllithium (n-BuLi) (1.6 M, 1.7 mL) under -78 ºC. The mixture was allowed to stir for 2 h and a solution of Weinreb amide of (R)-N-methoxy-N-methyl-2-(1-(phenylsulfonyl)-1H-indol-5-yl)-4,5-dihydrothiazole -4-carboxamide (1.24 mmol) was charged (6). The temperature was allowed to increase to room temperature (RT) and stirred overnight followed by quenching of reaction mixture with saturated NH_4Cl. Product was extracted with ethyl ether, and dried with $MgSO_4$. Crude product was refluxed in ethanol solution of 1 N NaOH to obtain the deprotected compound LY293 which was purified by column chromatography to obtain pure compound as a light-yellow solid.

4.2.3 Synthesis of mPEG-b-P (CB-co-LA)

Benzyl 2, 2-bis (methylol) propionate was synthesized as reported previously by reacting 2,2-bis(hydroxymethyl) propionic acid with benzyl bromide at 100°C for 15 h (40). Monomer 5-methyl-5-benzyloxycarbonyl-1, 3-dioxane-2-one (MBC) was synthesized by reacting the intermediate with triphosgene at -78°C in pyridine and dichloromethane. Random MBC and lactide block copolymer (mPEG-b-P (CB-co-LA)) of target molecular weight of 30,000 Da was obtained by ring opening polymerization of L-lactide and MBC using mPEG as macroinitator and   8-diazabicycloundec-7-ene (DBU) (2.5 mol relative to mPEG) catalyst (181, 182). Reaction was carried out in DCM

at room temperature for 6 h, after which benzoic acid was added to quench the catalyst. The resulting solution was concentrated to approximately 50% of the initial volume and added dropwise into excess of cold isopropanol for polymer precipitation. Following synthesis, the copolymer was characterized by ^{1}H NMR and GPC. For ^{1}H NMR, chemical shifts were calibrated using tetramethylsilane as reference and reported as parts per million. The molecular weight and polydispersity index (PDI) of mPEG-b-P (CB-co-LA) polymers were determined by GPC using a Shimadzu GPC system equipped with a Styragel HR 4E GPC column and a differential refractive index detector. Dimethyl formamide (DMF) was used as an eluent at a flow rate of 0.5 mL/min. Narrow PEG standards (5,800-71,700 g/mol) from American polymer standards corp were used for generating standard curves and the data was processed using LC Solution ver.1.21 GPC option software.

4.2.4 Preparation and characterization of nanoparticles

Blank and LY293 loaded nanoparticles were prepared by o/w emulsification using 1% polyvinyl alcohol as an emulsifier (41). mPEG-b-P (CB-co-LA) and drug dissolved in dichloromethane and acetone mixture (1:1 ratio) were emulsified using a Misonix ultrasonic liquid processor (Farmingdale, NY) at amplitude of 20 for 2 min. Organic phase was removed by a rotavapor to obtain stabilized nanoparticles and concentrated by ultracentrifugation at 20,000 rpm for 30 min followed by washing with water to remove polyvinyl alcohol and unentrapped drug. Mean particle diameter and size distribution of drug-loaded nanoparticles were determined via dynamic light scattering (DLS) using a Malvern Zetasizer Nano Series (Worcestershire, UK). Surface morphology and particle size of nanoparticles was determined using a transmission

electron microscope (TEM) (JEM-100S Japan). Suspension of nanoparticles on a copper grid was negatively stained with NanoVan®. The grid was visualized at 60 kV with magnifications ranging from 50, 000X to 100,000X.

Drug loading was estimated by reverse phase high performance liquid chromatography (RP-HPLC, Shimadzu) at 290 nm wavelength using a C18 column (250 mm x 4.6 mm, Alltech, Deerfield, IL). Mobile phase composed of 65:35 V/V of acetonitrile and water was used. LY293 concentration was calculated using the peak area from a standard curve with R^2=0.9987 and lower quantification limit of 73.42 ng/ml. Drug loading was determined by the following formula

$$Percentage\ drug\ loading = \frac{weight\ of\ drug}{weight\ of\ nanoparticle}\ X\ 100$$

4.2.5 In vitro drug release from nanoparticles

Dialysis technique was employed to determine the drug release from mPEG-b-P (CB-co-LA) nanoparticles. mPEG-b-P (CB-co-LA) nanoparticles were placed in a dialysis membrane of 8,000 Dalton cut-off and dialyzed against 50 mL of 0.1 % Tween 80 phosphate buffered saline (PBS) (pH 7.2) in a thermo-controlled shaker with a stirring speed of 180 rpm. Samples of 1 mL were withdrawn at specified times (4, 8, 12, 24, 36, 48, 72, 96, 120, 168 and 216 h) and replaced with fresh media. Release samples were assayed using RP-HPLC as described for drug loading estimation. The cumulative amount of drug released into the media at each time point was evaluated as the percentage of total drug release to the initial amount of the drug. All experiments were performed in triplicate and the data is reported as the mean of the three individual experiments.

4.2.6 Cell cytotoxicity assay

A375 and B16F10 cells were cultured in DMEM media supplemented with 10% fetal bovine serum (FBS) and 1% antibiotic–antimycotic at 37°C in humidified environment of 5% CO_2. Cells were seeded overnight in 24 well plates at a density of 25,000 cells per well and thereafter treated with DMSO solution of LY293 and LY293 loaded nanoparticles for 72 h. At the end of 72 h, cell culture medium was replaced with 50 μL of 5 mg/mL 3-(4, 5-dimethyl-thiazol-2-yl)-2, 5-diphenyl tetrazolium bromide (MTT) solution and incubated for 3 h at 37°C. Cell culture medium was removed and formazan crystals were dissolved in 500 μL of DMSO for measuring the absorbance. Absorbance was measured by a microplate reader at a wavelength of 560 nm. Cell viability was expressed as the percentage of the control group. DMSO control and blank nanoparticles were included in all experiments.

4.2.7 Propidium iodide staining and cell cycle analysis

A375 and B16F10 cells were cultured overnight in a 6 well plate followed by thymidine blockade for 12 h. Cells were then incubated with LY293 loaded nanoparticles for 48 h. Treated cells were trypsinized and fixed in 90% ice-cold ethanol overnight. After washing with PBS containing RNase (1 mg/mL), cell pellet was re-suspended in 5 μg/mL propidium iodide staining solution for 30 min at the room temperature. Cell cycle distribution was measured by flow cytometry (Becton, Dickinson, NJ, USA). Results from 10,000 fluorescent events were obtained for cell cycle analysis.

4.2.8 Western Blot Analysis

A375 cells cultured overnight in a 12 well plate were treated with LY293 for 24 h. Subsequently, cells were lysed using RIPA buffer (Sigma- Aldrich, St. Louis, MO) and

protein concentration was measured with bicinchoninic acid (BCA) protein assay kit (Pierce, Rockford, IL). The lysate was boiled for 5 min, subjected to a 15 % SDS-PAGE and transferred to a PVDF membrane using iBlot™ system (Invitrogen, Carlsbad, CA). Membranes were blocked with 3% BSA in 1x Tris buffered saline (TBS) at room temperature for 1h and then incubated with primary antibodies at 4 °C overnight, followed by incubation with anti-goat or anti-rabbit IRDye 800CW secondary antibodies for 1h at room temperature. All the blots were re-probed with total β-actin antibody as control. The signal of target proteins was detected Li-COR Odyssey® infrared imaging system (Li-COR, Lincoln, NE).

4.2.9 Calcein acetoxymethylester (Calcein AM) assay and cell cytotoxicity assay in Pgp overexpressing melanoma cell lines

MDA-MB435 and MDA-MB435/LCC6 MDR1 cells were seeded into black wall clear bottom 96 well plates at a density of 50,000 cells per well a day before the experiment. Media was removed and cells were washed twice with PBS. After treating cells with various concentrations of test compounds in 50 µL of PBS for 15 min at 37°C, 50 µL calcein AM (10 µM) in PBS was added to each well and incubated at 37°C for additional 15 min. Fluorescent intensity was determined using a SpectraMax M2/M2e spectrofluorometer (Sunnyvale, CA) at the excitation wavelength of 485 nm and emission wavelength of 525 nm.

Cytotoxic or antiproliferative activity of LY293 analogues (ABI270) was investigated by our collaborator in MDA-MB435 and MDA-MB435/LCC6 MDR1 by using the sulforhodamine B (SRB) assay. Cultured cells were plated in 96-well plates and incubated with titration of the test compounds. The cells were stained with SRB after 96 h treatment

4.2.10 In vivo anticancer efficacy study

All animal experiments were performed in accordance with the NIH animal use guidelines and protocol approved by the Institutional Animal Care and Use Committee (IACUC) at the University of Nebraska Medical Center (UNMC, Omaha, NE). Lung metastasis in C57/BL6 mice (6−8 weeks old, weight around 20 g) was used as a tumor model. Mice were injected intravenously with 100 µL of B16F10 cell suspension containing 10^5 cells through tail vein. Post one week, mice were divided into three groups (n =6): control, LY293 in 35 % of cosolvent (composed of propylene glycol, cremophor EL and ethanol (50:30:20 ratio) and 65 % of dextrose solution and LY293 loaded nanoparticles. Formulations were injected into the tail vein of mice thrice a week at the dose of 15 mg/kg. Mice were sacrificed at the end of the treatment, and lungs were separated and expanded with 10% formalin buffer. The number of lung metastasis nodules was noted and tumor index was calculated using formula 1*a + 2*b + 3*c where a is the number of nodules with size <1 mm; b is the number of nodules with size between 1 and 2 mm; and c is number of nodules with size >2 mm. Animal mobility and body weight were monitored during the entire experiment period to assess any toxicity. In addition, tumor tissues were fixed in formalin buffer and sections were stained with hematoxylin and eosin (H&E). For immunohistochemistry (IHC) analysis, sections of 5−7 µm thickness were cut and immunostained with rabbit anti-Caspase-3, anti-Ki67 and anti-S100 primary antibodies, respectively. The immunoreactivity was detected using goat anti-rabbit IgG, H&L chain specific peroxidase conjugate and subsequent incubation with DAB substrate.

4.2.11 Statistical analysis

Statistical significance of the difference between the two groups was determined by an unpaired Student's t-test and between several groups by one-way analysis of variance.

4.3 Results

4.3.1 Synthesis and characterization of LY293

LY293 was synthesized by Dr. Yan Lu as shown in **Figure 4.2A** and the chemical structure of synthesized LY293 was ascertained by ^{1}H NMR (**Figure 4.2B**), and ESI-MS. ^{1}H NMR (300M, CDCl3) δ 8.36 (br, s, 1 H), 8.31 (s, 1 H), 8.21 (s, 1 H), 7.89 (dd, 1 H, J = 1.8, 2.7 Hz), 7.46 (d, 1 H), 7.62 (s, 2 H, J = 8.7 Hz), 7.29 (t, 1 H, J = 2.7 Hz), 6.64 (br, 1 H), 3.95 (s, 6 H), 3.89 (s, 3 H). MS (ESI) had m/z ratio of 417.1 (M + Na) [+] and 392.9 (M - H) [-].

4.3.2 Synthesis and characterization of mPEG-b-P(CB-co-LA)

DBU, an organic base with low nucleophilicity and mPEG as macroinitator was utilized for synthesis of mPEG-b-P(CB-co-LA) copolymer in solution at ambient temperature with high conversion rate. Synthesized mPEG-b-P(CB-co-LA) copolymer was characterized by ^{1}H NMR and GPC. ^{1}H NMR spectra was used to confirm the polymerization and calculation of molecular weight of the copolymer (**Figure 4.3A**). The emergence of the multiplet peak at δ: 4.25–4.35 ppm, δ: 7.3 ppm from the carbonate monomer and one methylene proton of lactide at δ= 5.12 ppm confirms the successful ring opening polymerization and formation of mPEG-b-P(CB-co-LA) copolymers. The relative molecular weight of the LA and MBC block was estimated based on the peak areas of three fifth of the 5.12 ppm signal and the five protons associated with the phenyl ring in the carbonate monomer at 7.3 ppm. From ^{1}H NMR, calculated molecular

weight of mPEG-b-P(CB-co-LA) was 31200 with 90 % conversion rate for LA and 60 % conversion rate for MBC (**Figure 4.3C**). As PEG was used as a macroinitator for ring opening polymerization, narrow PEG standards (5,800, 10,225, 14,500, 20000, 31,380, 50,450 and 71,700 g/mol) were used to generate standard curve for GPC analysis. We characterized mPEG-b-P(CB-co-LA) copolymer by GPC, which indicated a narrow molecular weight distribution with a PDI of 1.20 **(Figure 4.3 C & B)**. The molecular weight values determined by GPC were 29671 for weight average molecular weight (Mw) and 24650 for number average molecular weight (Mn). NMR and GPC data confirmed the synthesis of copolymer with controlled molecular weight with narrow molecular weight distribution.
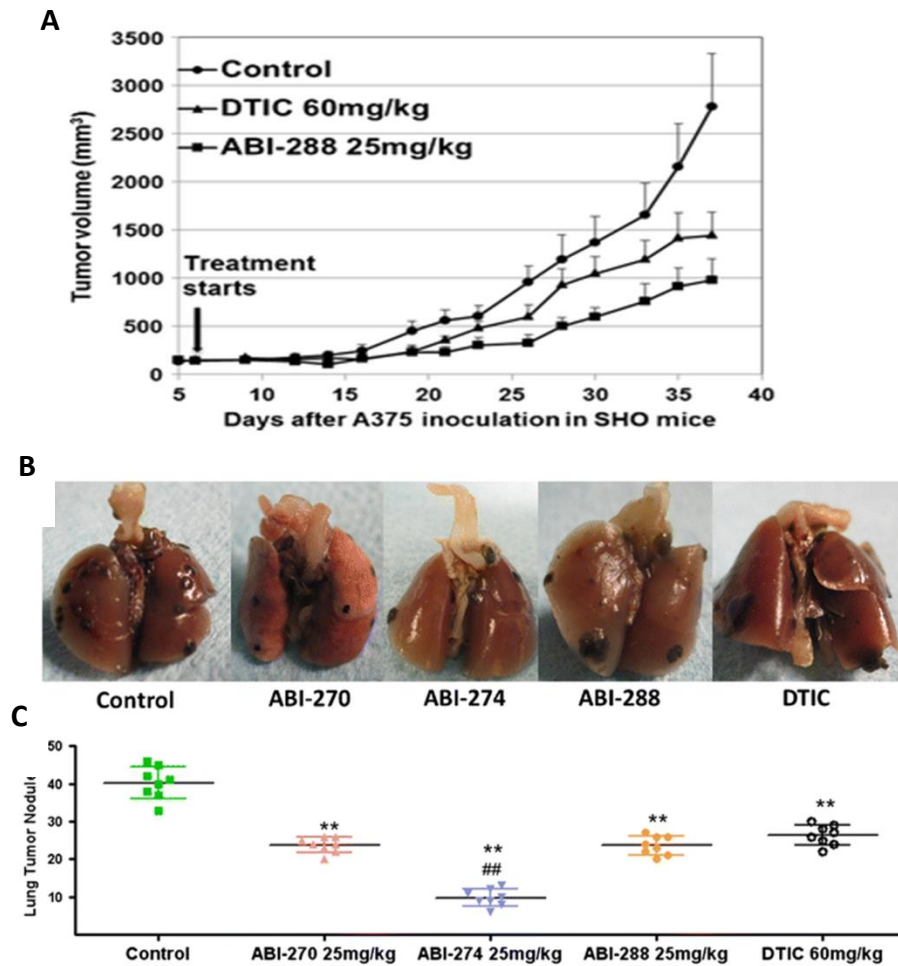
Figure 4-1.   In vivo efficacy study of LY293 analog, ABI compounds in xenografted human A375 model and in B16-F10 melanoma lung metastasis model

(A) LY293 analog, ABI-288 treatment inhibited xenografted human A375 melanoma tumor growth on SHO mice. Tumor growth curves ($n = 5$ per group). Treatment was i.p. injection once daily for 31 days. (B) ABIs and DTIC treatment inhibited B16-F10 melanoma cell metastasis to lungs of C57BL/6 mice after tail vein inoculation. Representative photos of lungs with melanoma nodules (black dots) on them ($n = 8$ per group). Treatment was i.p. injection 5 days/week for 2 weeks. (**C**) Number of melanoma nodules on each lung. Points: individual nodule number; long line in the middle: mean; short line on the top and bottom: 95 % confidence intervals. **(Adapted from Ref 174)**
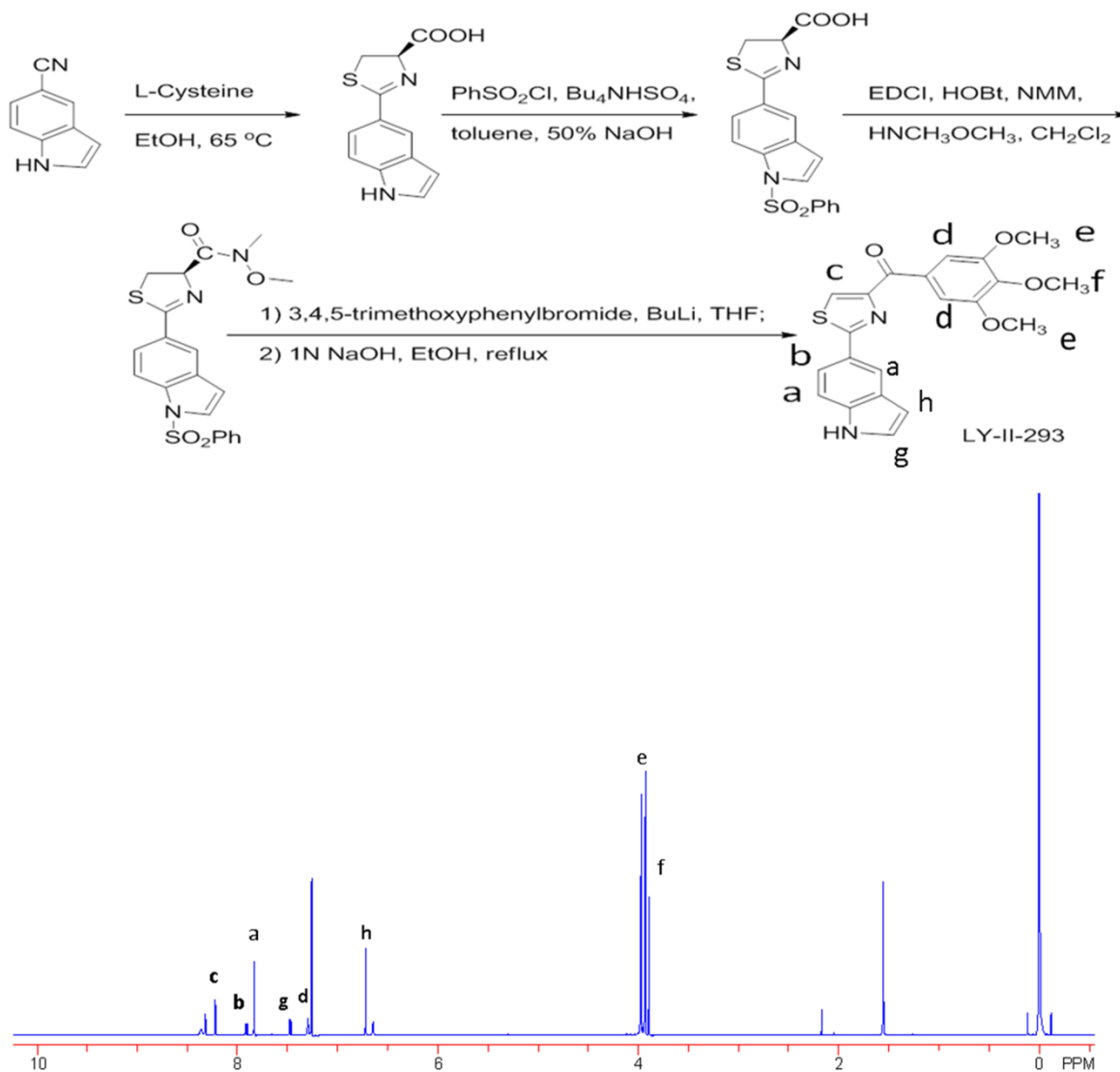
Figure 4-2.   Synthesis and characterization of (2-(1H-Indol-5-yl) thiazol- 4-yl) 3, 4, 5-trimethoxyphenyl methanone (LY293).

(A) Synthesis scheme of LY293. (B) ^{1}H NMR spectrum of LY293

A

B

C

Polymer	Mn (NMR)	Mw (GPC)	Mn (GPC)	PDI
PEG$_{114}$-b-P(CB$_{40}$-co-LA$_{225}$)	31200	29671	24650	1.20
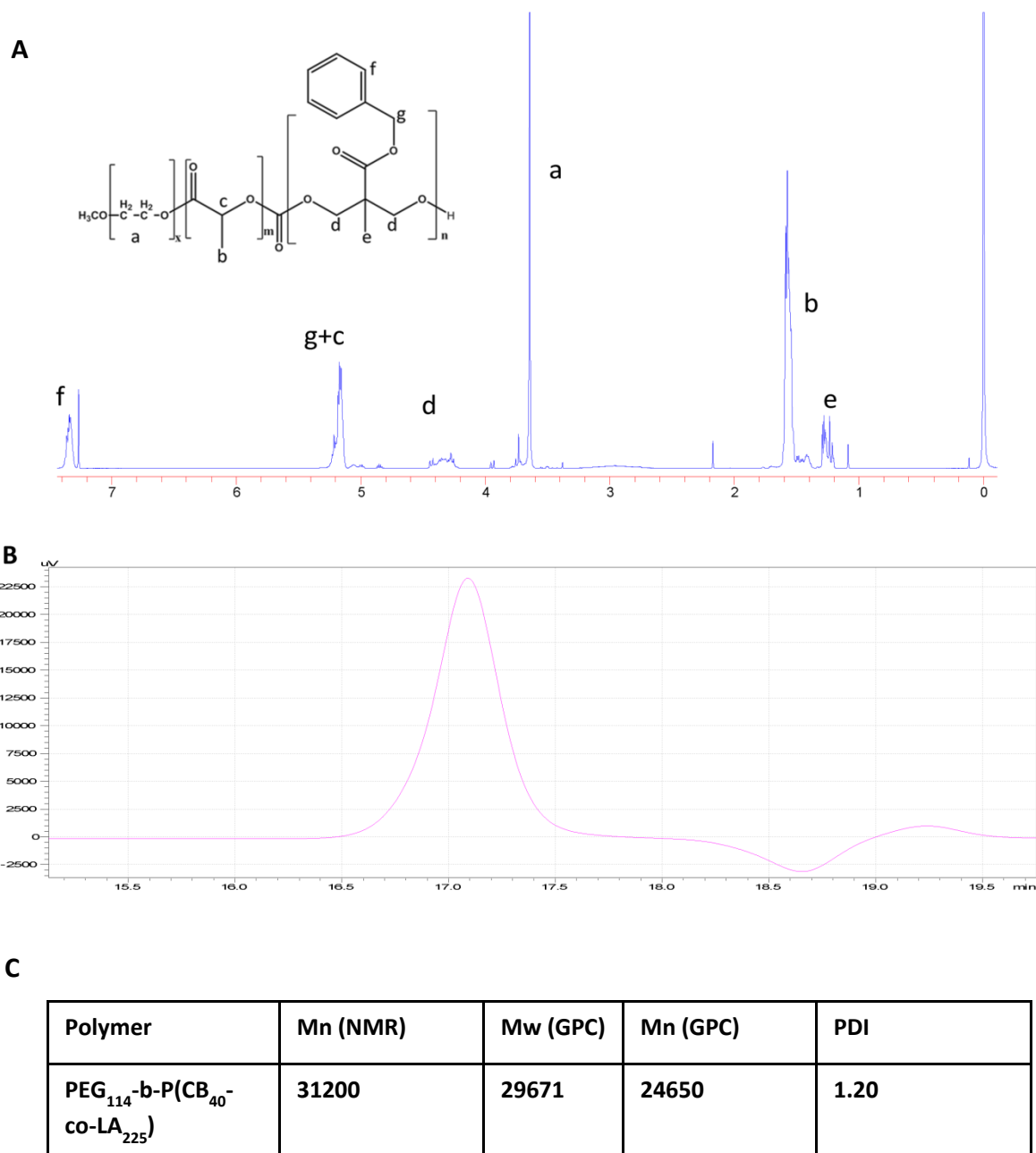
Figure 4-3.   Synthesis and characterization of mPEG-b-P (CB-co-LA) copolymer.

(A) ^{1}H NMR spectrum of mPEG-b-P(CB-co-LA) in DMSO-d6 and chemical structure of mPEG-b-P(CB-co-LA) copolymer. (B) Representative GPC chromatogram of mPEG-b-P(CB-co-LA). (C) Characterization of mPEG-b-P (CB-co-LA) copolymer by GPC for molecular weight and polydispersity index. Mw and Mn weight and number average molecular weights respectively as determined by GPC; PDI (Mw/Mn).

4.3.3 Formulation, characterization and in vitro cytotoxicity of nanoparticles

The mean particle size of mPEG-b-P(CB-co-LA) nanoparticles was 150 nm with a PDI of 0.068 as determined by DLS (**Figure 4.4A**). Drug loading and ultracentrifugation did not alter the particle size and its uniform distribution. TEM confirmed the uniform spherical particle of 50-70nm (**Figure 4.5B**). Drug loading calculated by HPLC was 2.5, 4.11 and 7.40 % at the theoretical loadings of 2.5, 5 and 10 %, respectively (**Figure 4.4 C**). The cumulative percentage of LY293 released from mPEG-b-P (CB-co-LA) nanoparticles with two different drug loadings is shown in **Figure 4.5**. These nanoparticles did not show any burst release and less than 10 % of drug was released after 10 h (13). Absence of burst release indicated excellent encapsulation of the drug within the nanoparticles and miscibility of drug within the polymeric core. However, 5 % drug loaded nanoparticles showed a faster drug release as compared to 2.5 % nanoparticles. Similarity factor (f2) was calculated to compare the drug release profiles of 2.5 and 5 % drug loaded nanoparticles. The similarity factor was 41.16 for (2.5 vs. 5 % NP) indicating nanoparticles with two different drug loadings showed different release profiles as the release profiles are considered different when the similarity factor is less than 50.

LY293 loaded nanoparticles inhibited the cancer cell proliferation as efficiently as DMSO solution of LY293 with an IC_{50} of 17.5 nM in A375 and B16F10 cells (**Figure 4.6**). Blank nanoparticles did not elicit any cytotoxicity to the cells as expected with biodegradable polymers.

A

B

C

Theoretical loading	Drug loading	% Loading efficiency	Particle size (nm)	PDI
2.5 %	2.5 ± 0.23 %	100.0	148 ±10	0.090
5 %	4.11 ± 0.21%	82.2	148 ±10	0.080
10 %	7.40 ± 0.36%	74.0	154 ± 6	0.10
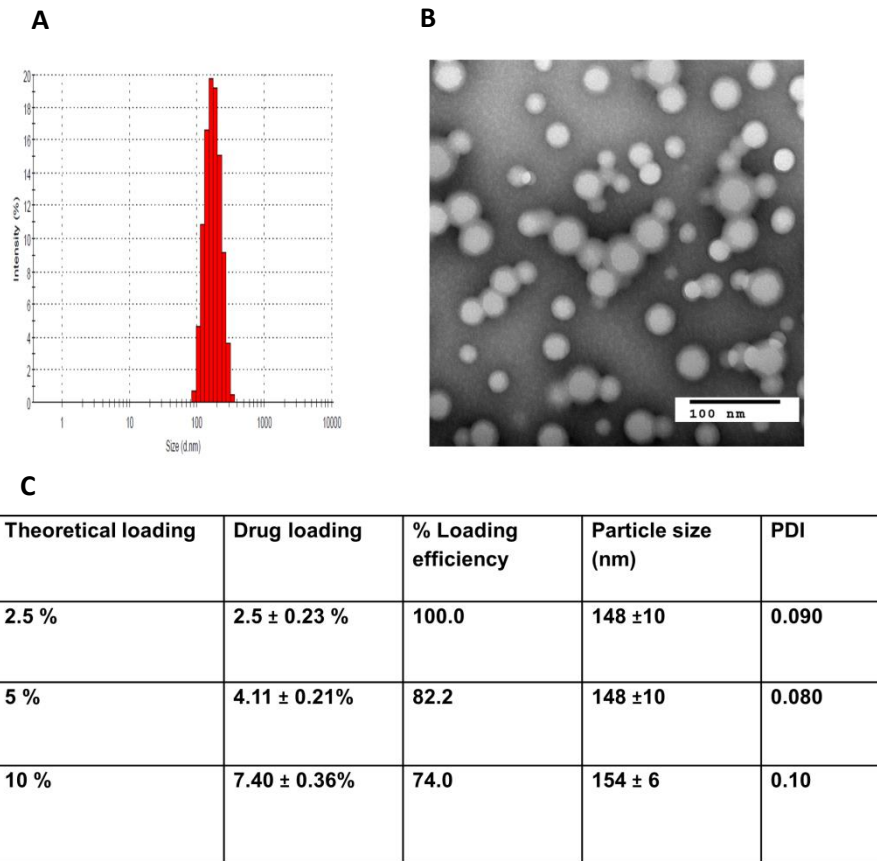
Figure 4-4.   Characterization of nanoparticle for size distribution, morphology and drug loading.

(A) Dynamic light scattering histogram; and (B) transmission electron micrograph obtained negative staining. (C) Effect of theoretical loading on particle size and loading efficiency
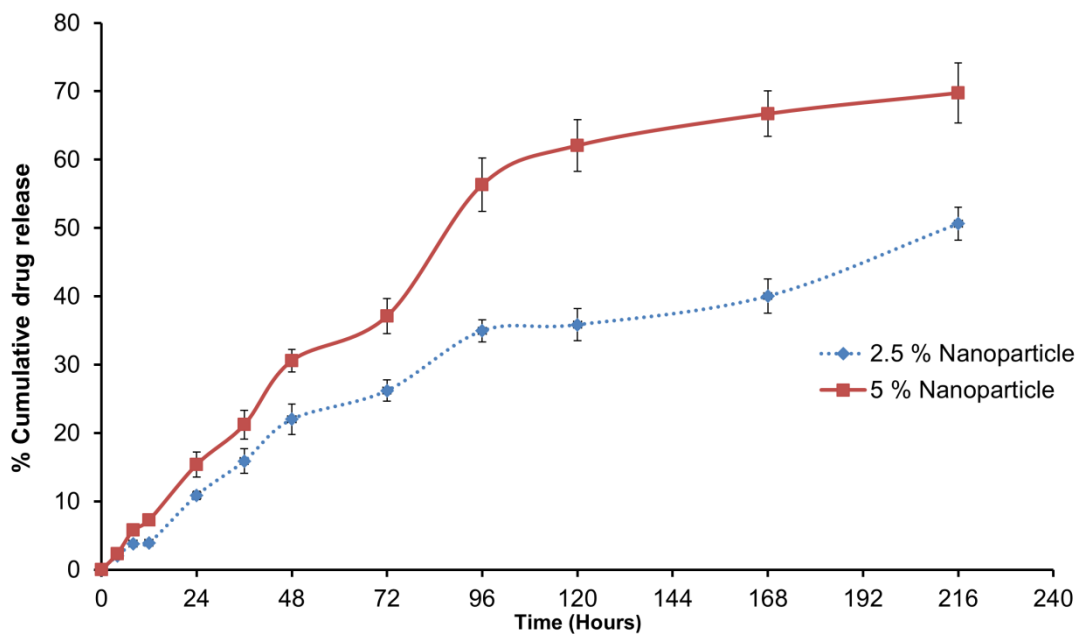
Figure 4-5.   In vitro drug release from mPEG-b-P(CB-LA) nanoparticles.

In vitro release of LY293 of 2.5 and 5 % loaded mPEG-b-P(CB-co-LA) nanoparticles. Results are expressed as the mean ± SD (n = 3).
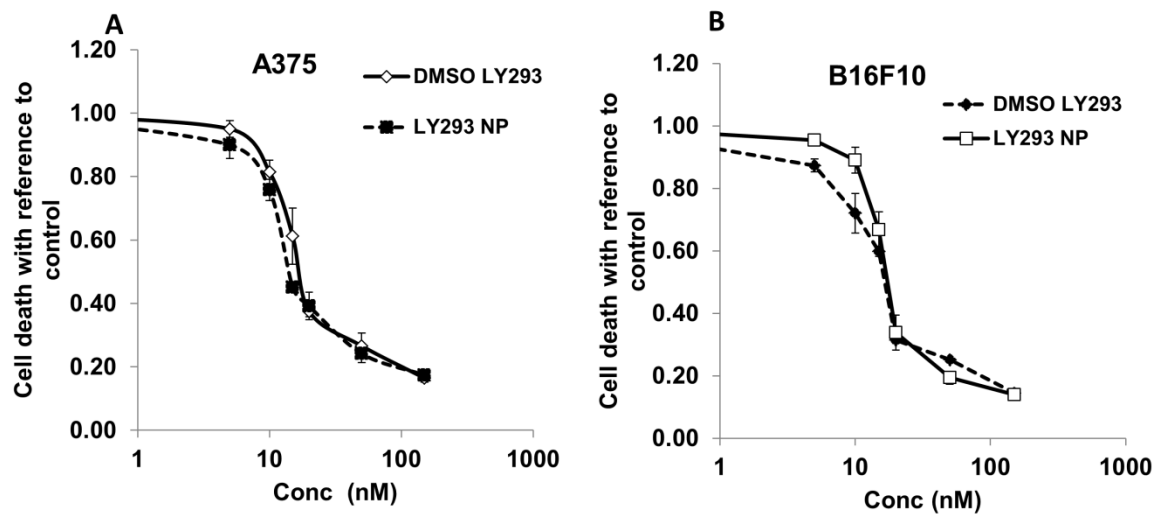
Figure 4-6.   Cell cytotoxicity of DMSO solution of LY293 and LY293 loaded nanoparticles.

(A) A375 and (B) B16F10 cell death after 72h of treatment. Cytotoxicity was determined by MTT Assay and expressed as % of control. Blank nanoparticles used as control for LY293 loaded nanoparticles group. Results are expressed as the mean ± SD (n = 4).

4.3.4 Effect of LY293 loaded mPEG-b-P(CB-co-LA) nanoparticles on cell cycle and apoptosis

Tubulin polymerization inhibitors bind to tubulin and arrest the cell cycle in G2/M phase. As shown in **Figure. 4.7 A&B**, 48h treatment of A375 and B16F10 cells with LY293 loaded nanoparticles led to cell cycle arrest in G2/M phase while no effect was observed upon treatment with blank nanoparticles. Anti-mitotic activities of LY293 resulted in significant increase in G2/M phase from 14.13±0.60 % in the control group to 54.33±0.085% and 76.19±0.94 % at 15 nM and 250 nM of LY293 loaded nanoparticles group in A375 (p< 0.005).

Disruption of the cell cycle progression and arrest of cells in G2/M activates apoptotic cell mechanism. Treatment with LY293 loaded nanoparticles significantly increased the protein levels of cleaved PARP with a corresponding decrease in the levels of total PARP levels (**Figure 4.7C**). In addition, the cells in sub G1 phase were also increased from 2.005±0.25% in control to 28.35±0.92 % and 41.9±1.76% for 48 h at 15 and 250 nM, respectively (p<0.005). The increase of cell population in sub G1 phase indicated that apoptotic cells were increased as LY293 loaded nanoparticle treatment arrested cells in G2/M phase (**Figure 4.7 D**).
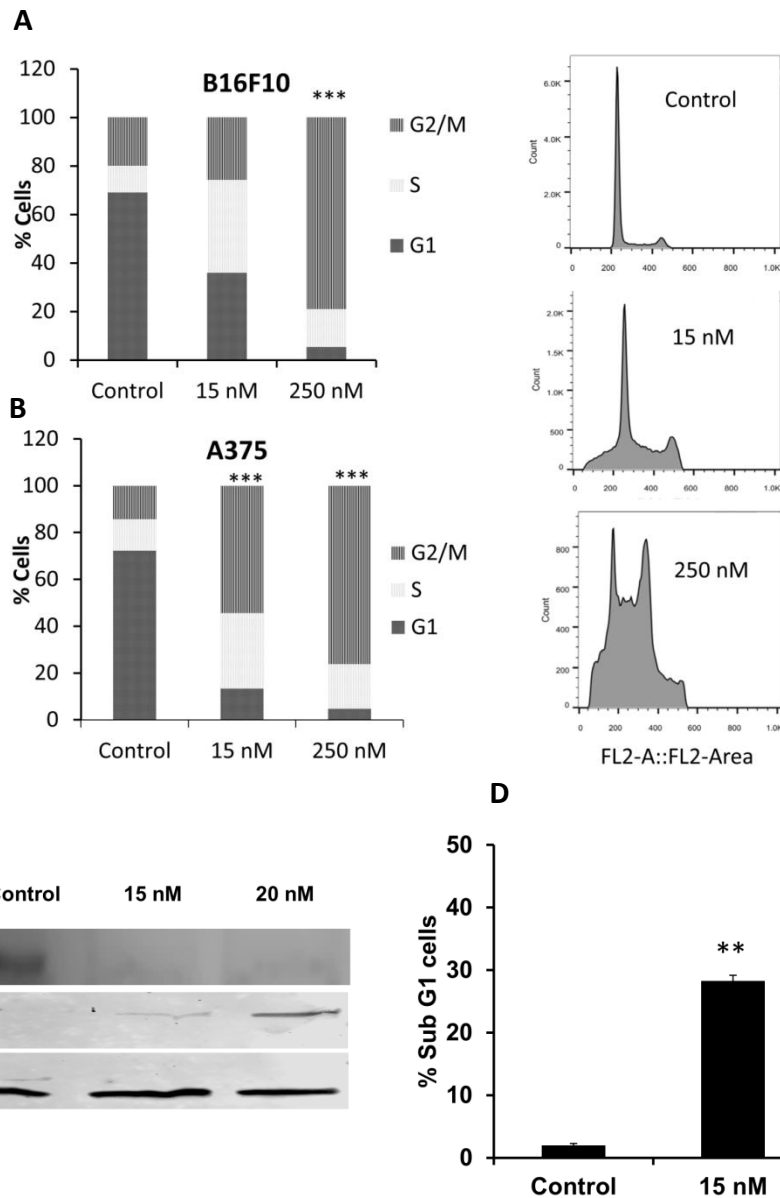
Figure 4-7.   Concentration dependent effect of LY293 loaded nanoparticles on cell cycle distribution.

Cells were treated with LY293 loaded nanoparticles (15 and 250 nM) for 48 h, stained with propidium iodide and analyzed on a flow cytometer (A) B16F10 (B) A375. Results are expressed as the mean ± SD (n=3). ***p<0.0005 for cells in G2/M phase using Student's unpaired t test. (C) A375 were treated with LY293 loaded nanoparticles at 15 and 20 nm, protein was isolated at 24h. Total and cleaved PARP expression at protein level was determined using Western blot. Representative beta actin blot is shown. (D) A375 cells were treated with LY293 loaded nanoparticles for 24 h and quantitative analysis of apoptotic cells as determined by staining with propidium iodide and analyzed on a flow cytometer. Results are expressed as the mean ± SD (n=3). **p<0.005 using Student's unpaired t test.

4.3.5 Effect of LY293 on Pgp activity

To determine the inhibitory activity of LY293 on Pgp, intracellular level of calcein AM (viability dye) was measured by fluorescence spectroscopy. Pgp overexpressing MDA-MB435/LCC6 MDR1 cells were treated with Verapamil, LY293 and paclitaxel. Verapamil is a well-known inhibitor of Pgp activity and leads to intra cellular accumulation of calcein AM. LY293 lead to significant intra cellular accumulation of calcein AM at a concentration of 5 and 50 µM as compared to untreated and paclitaxel treated cells (**Figure 4.8**).

4.3.6 In vivo efficacy study

Melanoma is highly metastatic, and lung is one of the major target organs for metastasis. We used an experimental lung metastasis mouse model established via tail vein injection of melanoma cells to test the efficacy of LY293 loaded nanoparticles in preventing tumor lung metastasis. After 2 weeks of experimental treatment, the tumor index was 84, 38, and 30 in control, the cosolvent solution of LY293 and LY293 loaded nanoparticle groups, respectively (**Figure 4.9A**). Tumor index was significantly different between the control and LY293 loaded nanoparticle treated groups (p<0.00005). Treatment with LY293 significantly reduced the nodule count and black cellular mass associated with the lungs (**Figure 4.9A**). H&E staining of lung tissue confirmed the inhibition of proliferation of metastatic cells. In the control group, normal lung parenchyma was not visible and was completely covered with the dense metastatic tissue. Significant inhibition of proliferation of melanoma cells by LY293 loaded nanoparticle treatment group was further confirmed by the reduced density of S100 immunostains (**Figure 4.10**). Ki67 positive staining showed significant proliferation in control group as compared to LY293 treated group. We observed the reduction in body

weight across all groups including control after treatment started. There was statistical difference for reduction in body weight between the control and LY293 loaded nanoparticle treatment group (p<0.05). Systemic administration of LY293 loaded nanoparticles and cosolvents did not exhibit any toxicity which was confirmed by the absence of necrosis or inflammation in H&E staining of liver and kidney sections (**Figure 4.10**).

A

B

1 µM LY293 5 µM LY293 50 µM LY293

C

	IC$_{50}$ ± SEM (nM) (n = 3)		
	MDA-MB-435	MDA-MB-435/LCC6MDR1	resistance index
LY293 analogue (ABI-270)	24 ± 2	30 ± 4	1.3
paclitaxel	4 ± 1	277 ± 41	69.3
vinblastine	0.4 ± 0.1	11 ± 1	27.5
colchicine	10 ± 1	658 ± 50	65.8
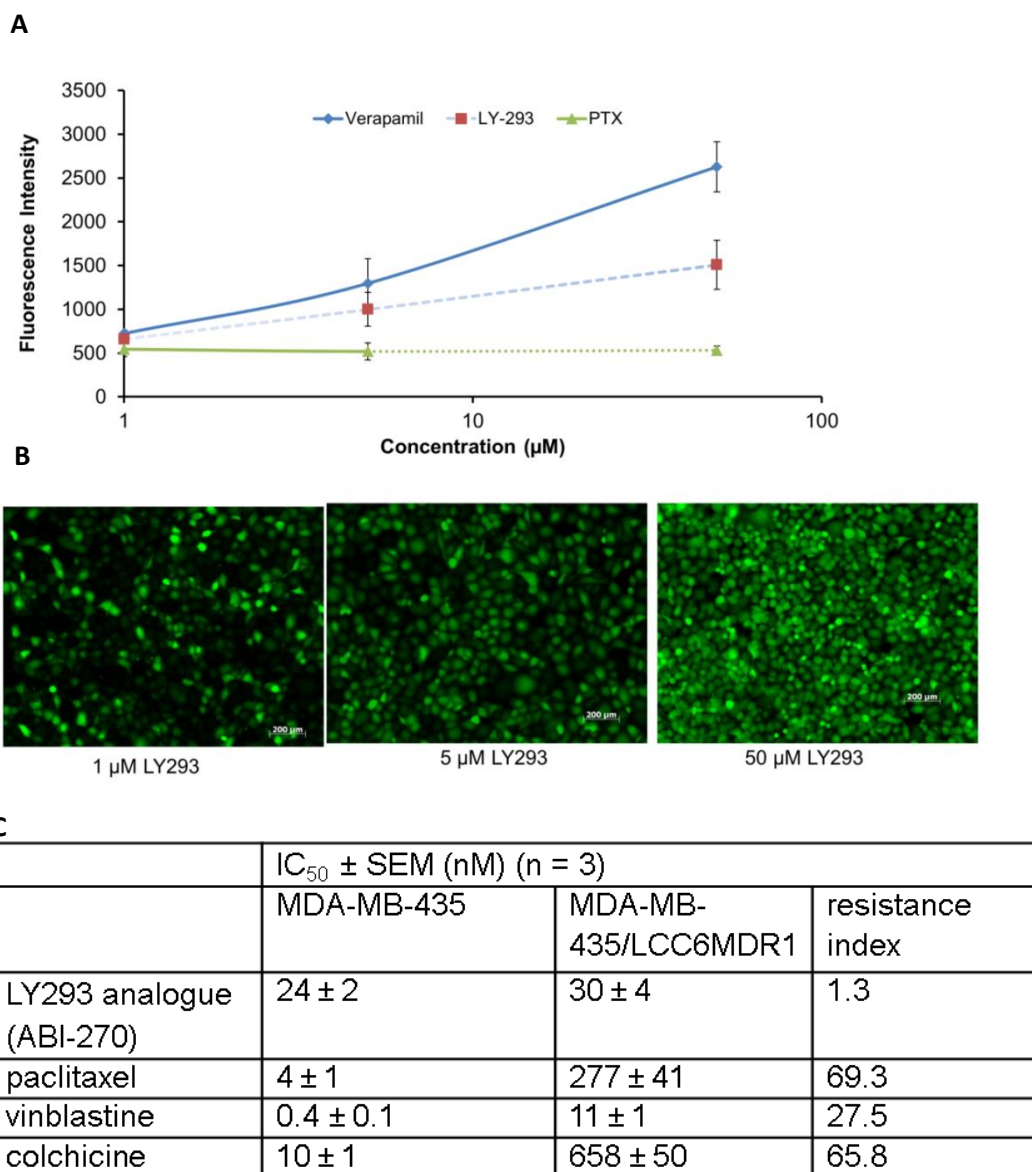
Figure 4-8. Effect of LY293 on Pgp activity and cell cytotoxicity in resistant melanoma cell line (MDR cell) and the matching sensitive parent cell line.

(A) Intracellular calcein accumulation in MDA-MB435/LCC6MDR1 after 30 min treatment with Verapamil, LY293 and PTX. Results are expressed as the mean ± SE (n=3). (B) Fluorescent images depicting dose-dependent increase in intracellular calcein fluorescence in MDA-MB435/LCC6 MDR1 following 30 min treatment with LY293. (C) In vitro growth inhibitory effects of the ABI compounds in comparison to other anticancer drugs on multidrug-resistant melanoma cell line (MDR cell) and the matching sensitive parent cell line (Normal Melanoma cell). Resistance indexes were calculated by dividing IC50 values on multidrug-resistant cell line MDA-MB-435/LCC6MDR1 by IC50 values on the matching sensitive parental cell line MDA-MB-435. **(Adapted from Ref 174)**
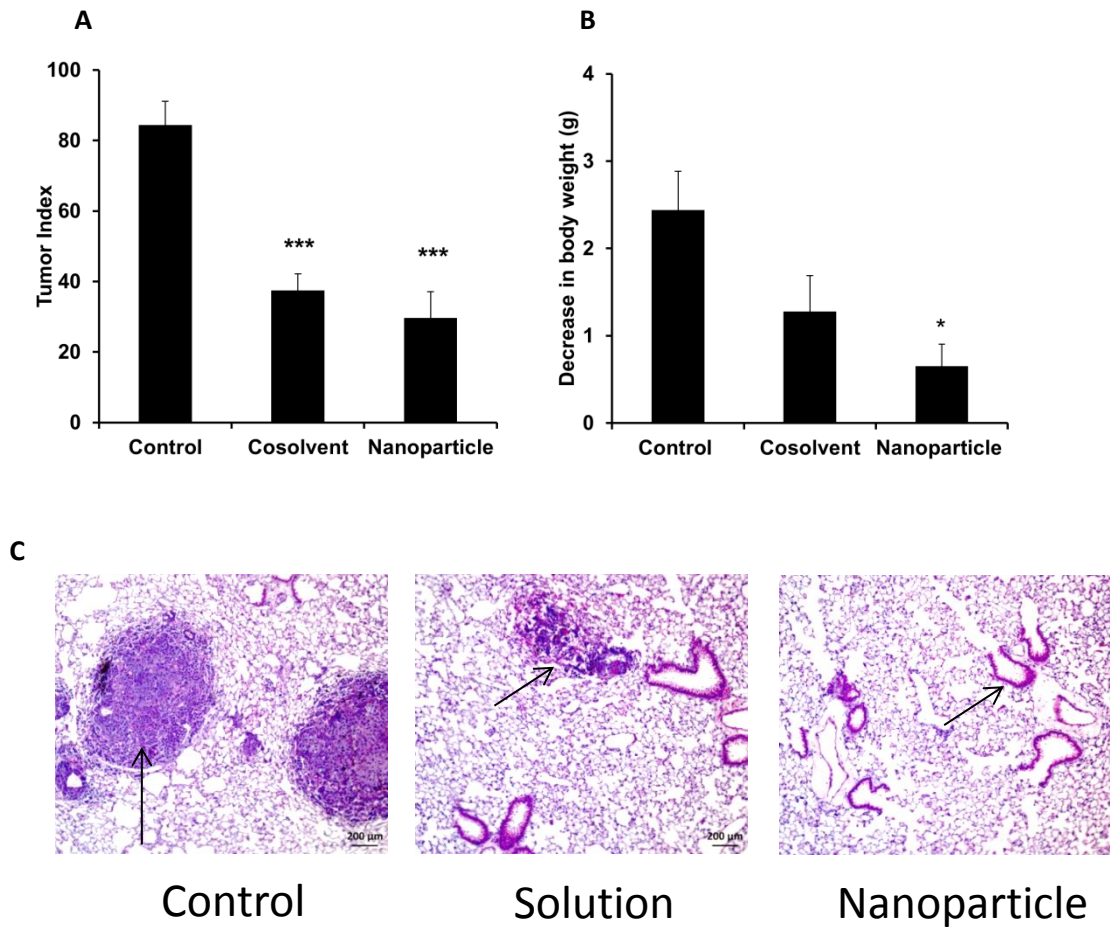
Figure 4-9. **Effect of systemic therapy of LY293 cosolvent solution and LY293 loaded nanoparticles on proliferation of lung metastasized melanoma.**

(A) Tumor index in B16F10 lung metastasis mouse melanoma model at three weeks after intravenous injection of different formulations. ***p<0.00005 using Student's unpaired t test. (B) Change in body weight in of mice at the end of the study. Results are presented as mean ± SD (n = 6). (C) Representative photos of lungs with melanoma nodules (black dots) on them (C) H&E stained images of treated group showed normal lung parenchyma with limited mass of metastatic growth (arrow) as compared to dense metastatic tissue in the control group (Solid arrow). Black bar represents 200 μm.
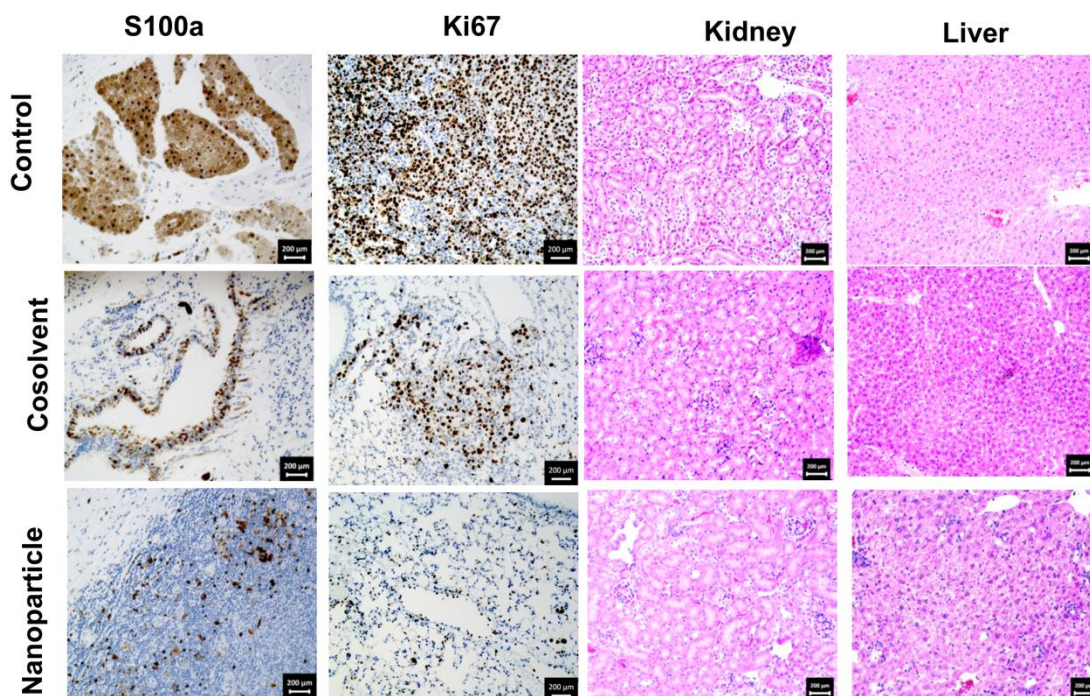
Figure 4-10.   Immunohistochemistry staining of isolated lungs for S100 and Ki67.

Representative IHC images for S100 and Ki67 staining of lung tissue sections after 2 weeks of treatment. White bar represents 200 µm. H&E staining of liver and kidney confirmed the absence of nanoparticle toxicity to vital organs.

4.4 Discussion

Prognosis of metastatic melanoma is poor and associated with a survival rate of less than 15 % at the end of five years (170, 183). Inherent ability of melanocytes to survive under duress as well as the development of resistance to cytotoxic drugs remains key challenges for poor prognosis of metastatic melanoma (184). For the last three decades since its initial FDA approval, dacarbazine remains the standard care of therapy for metastatic melanoma. However, treatment with dacarbazine leads to the development of resistance and has a poor response rate of approximately 7.5% (1). In spite of the clinical potential of paclitaxel and other tubulin inhibitors, ATP dependent efflux of these drugs by transporters contributes to the development of resistance (185, 186). To overcome MDR resistance and enhance the efficacy, we have previously synthesized potent tubulin inhibitor, phenyl thiazole (PAT) analogs with identical nanomolar efficacy in both parent and MDR overexpressing resistant cell lines (6). Although calcein AM efflux assay suggested that LY293 is a Pgp substrate (41) and should not have identical IC_{50} in MDR overexpressing cell lines, this anomaly can be attributed to the excellent permeability (33 x 10^{-6} cm/s) of LY293 analogs (187). Unlike paclitaxel, vinblastine and colchicine, LY293 has very high permeability and efflux by Pgp does not limit its intracellular accumulation (188, 189).

In addition to MDR resistance, poor solubility and non-specific distribution of tubulin inhibitors leading to the dose limiting toxicity are barriers for their systemic delivery. Nanodelivery systems have been designed to solubilize the poorly soluble drug and for effective tumor accumulation of drug through EPR effect. Enhanced tumor accumulation of nanoparticles will reduce the peripheral exposure and associated toxicity like peripheral neuropathy and myelosuppression. Herein, we have synthesized random

diblock copolymer of PEG block and block comprised of carbonate and lactide for systemic delivery of LY293. This copolymer consisted of mPEG (5000 Dalton) block that forms hydrophilic outer shell while the hydrophobic core is composed of lactide and carbonate. Previously, we have shown that modification of the core with carbonate monomer improved drug encapsulation and its release from nanocarriers (40). We have synthesized mPEG-b-P(CB-co-LA) copolymer by ring opening polymerization (ROP) of lactide and MBC using hydroxyl group of mPEG with N heterocyclic carbenes (NHCs). NHCs are strong organic bases, which allow ROP in solution at room temperature. For the synthesis of polymer of desired molecular weight with low PDI, two different NHCs, DBU and TBD at molar ratios of 1, 2.5 and 5 relative to mPEG were utilized. Based on the GPC and NMR data (Figure 4.3), we found that DBU at 2.5 molar ratio for 6 h were the optimum reactions conditions. With TBD, we could synthesize the polymer of desired molecular weight but PDI was higher as compared to DBU catalyst. This can be attributed to the higher basicity of TBD which makes it highly reactive leading to transesterification and backbiting side reaction (190). Nederberg et al have reported ROP of lactide and carbonate monomer of desired degree of polymerization using 1 molar of DBU (181, 182). This difference in the molar ratio of a catalyst can be attributed to the initiator used for ROP and the targeted molecular weight of the polymer.

Nanoparticles were formulated by film evaporation, dialysis, nanoprecipitation and o/w emulsification method. However, nanoparticles formulated only by o/w emulsification method had acceptable size and drug loading. We were able to encapsulate LY293 with high efficiency (Figure 4.4), which can be attributed to the

ability of the hydrophobic core to solubilize LY293. In addition to the appreciable drug loading, the hydrophilic mPEG shell could prevent the aggregation by steric hindrance and possibly reduce uptake by the reticuloendothelial system (RES) for longer blood circulation (191). We observed that an increase in initial drug loading led to decrease in the encapsulation efficiency of LY293 which can be attributed to the limited holding capacity of the hydrophobic core, reaching saturation at higher initial drug loading with a subsequent decrease in LY293 encapsulation (Figure 4.4 C).

In vitro cytotoxicity of LY293 loaded nanoparticles showed no loss of LY293 activity upon its formulation as nanoparticles against melanoma cancer cell lines (Figure 4.6). As a microtubule polymerization inhibitor, LY293 exerts its antiproliferative effect by targeting and destabilizing microtubules. The cell cycle analysis indicated that after treatment with LY293 loaded nanoparticles. LY293 loaded nanoparticles led to the concentration dependent arrest of A375 and B16F10 cells in G2/M phase (Figure 4.7). Tubulin polymerization is essential for rapid proliferation of cancer cells by mitotic division and the inhibition of tubulin polymerization results in the activation of intrinsic apoptotic pathway. Cell cycle analysis confirmed that the anticancer mechanism of LY293 is through the arrest of cell cycle in G2/M phase and subsequent activation of intrinsic apoptotic cellular machinery. In addition, LY293 loaded nanoparticle treatment resulted in significant increase in fraction of cells in sub-G1 phase (Figure 4.7). This increase in cell population in sub-G1 phase indicated the fraction of cells undergoing DNA damage and apoptosis by LY293 loaded nanoparticles.

After demonstrating excellent efficacy of LY293 loaded nanoparticles against melanoma cell lines, we tested the in vivo efficacy of LY293 loaded nanoparticles in

syngeneic B16F10 lung metastasis mouse model, which is an extremely aggressive metastatic model. Tumor burden as well as H&E data clearly showed that LY293 loaded nanoparticles inhibited the proliferation of metastatic B16F10 nodules (Figure 4.9). However, there was no significant difference between cosolvent solution and LY293 loaded nanoparticles, which can be attributed to premature release of the encapsulated drug from the nanoparticle core. Rapid diffusion of the encapsulated drug across the hydrophobic core led to premature release during circulation and did not significantly alter the distribution of LY293 towards tumor. To minimize the premature drug release and further improve the tumor accumulation, polymeric drug conjugates have improved stability in the circulation with enhanced tumor accumulation. For future studies, we plan to redesign the polymeric nanocarriers for allowing chemical conjugation of the drug analogs for preferential tumor accumulation and reduction of peripheral toxicity on systemic administration.

Chapter 5 GENETICALLY MODIFIED HUMAN BONE MARROW DERIVED MESENCHYMAL STEM CELLS FOR IMPROVING THE OUTCOME OF HUMAN ISLET TRANSPLANTATION*

5.1 Introduction

Type I diabetes is an autoimmune disease characterized by the destruction of islets. Transplantation of human islets has been clinically used to achieve insulin independence. However, in addition to long term graft rejection, clinical success of islet transplantation is limited by primary non-function (PNF) of islets (192). PNF is characterized by poor glycemic response due to β-cell death in the first two weeks after transplantation (193). There is marked β-cell death immediately after transplantation due to hypoxia and exposure to inflammatory cytokines released by infiltrating immune cells (194). Human islets upon exposure to inflammatory cytokines show increased expression of apoptosis markers (195). Interleukin -1 beta (IL-1β) produced by islets and macrophages plays a key role in the islet apoptosis after transplantation (196). hIL-1Ra competitively blocks IL-1β binding and has been shown to minimize the detrimental effect of IL-1β on islet viability (196, 197) .

Islets in pancreas have dense network of capillaries, much higher as compared to surrounding exocrine tissues (198, 199). Besides rich blood supply, there is an endothelial endocrine axis within adult pancreas, which is essential for the proliferation of β cells (200). Islet isolation and purification process not only destroys external vasculature but also adversely affects the intra islet endothelial cells (201). Revascularization of islet grafts is an essential event for the success of islet transplantation (202).

It has been demonstrated that vascular endothelial growth factor (VEGF) stimulates angiogenic capacity of intra islet endothelial cells and also recruits recipient endothelial cells to form new micro vessels (203, 204).

We previously demonstrated that bicistronic adenoviral vector encoding hVEGF and hIL-1Ra can improve the viability and revascularization of transplanted islets (7). However, adenovirus transduction of islets results in immune response especially when relatively higher multiplicity of infection (MOI) is used to get desired transgene expression (9, 196). To resolve this potential issue, we have used human bone marrow mesenchymal stem cells (hBMSCs) as gene delivery vehicles. In addition, hBMSCs also provide immune and anti-inflammatory protection to islet grafts (205) .

In this report, we have shown that hBMSCs were transduced with bicistronic adenoviral vector to coerexpress hVEGF and hIL-1Ra. The effect of Adv-hVEGF-hIL-1Ra transduced hBMSCs on islet viability and glucose stimulation was determined. Islets were co-transplanted with transduced hBMSCs under the kidney capsule of diabetic NSG mice to determine the effect of stem cells and gene therapy on the glycemic control and revascularization of transplanted islets.

5.2 Materials and methods

5.2.1 Materials

Replication-deficient (ΔE1/ΔE3) Adv-hVEGF-hIL-1Ra containing a cytomegalovirus (CMV) promoter, hVEGF cDNA, and rabbit β-globin poly A in the E-1 region, and a CMV promoter, hIL-1Ra cDNA, and rabbit β-globin poly A in the E-3 region was constructed amplified, and the titer was measured in our laboratory as previously described (206). Primary hBMSCs, HyClone Advanced Stem Cell Medium and Medium Supplement

were purchased from Thermo Fisher Scientific (Waltham, MA). Human islets were received from Integrated Islet Distribution Program (Duarte, CA). CMRL-1066 medium for islet culture, propidium iodide (PI) and 6- diamidino-2-phenylindole (DAPI) were purchased from Sigma Aldrich (St. Louis, MO). Fetal bovine serum (FBS) was purchased from MediaTech Cellgro (Herndon, VA). Phosphate-buffered saline (PBS) was purchased from GIBCO-BRL (Gaithersburg, MD). hVEGF and hIL-1Ra ELISA kits and recombinant inflammatory cytokines (IL-1β, TNF-α and IFN-γ) were purchased from R&D Systems (Minneapolis, MN). Human insulin and c-peptide ELISA kits were purchased from Alpco Diagnostics (Windham, NH). The primary antibodies for human insulin, human von-willebrand factor (vWF), and the Dylight 488-conjugated secondary antibody were purchased from Abcam (Cambridge, MA). Alexa Fluor 568- conjugated secondary antibody and 0.25% trypsin were purchased from Invitrogen (Carlsbad, CA). Eight-well Lab Tek Chamber slides were purchased from Nalge Nunc. (Rochester, NY). Ultrasensitive One Touch glucose test strips and One Touch Ultra glucometer were purchased from LifeScan (Milpitas, CA). Tissue-Tek optimal cutting temperature (O.C.T.) compounds were purchased from Sakura Finetek (Torrance, CA).

5.2.2 Characterization, transduction and differentiation of hBMSCs

Fluorochrome-coupled antibodies specific for Stro-1, CD73, CD90, CD105 and CD146 were used to analyze surface markers. Flow cytometric data were acquired using LSR II Special Option Flow Cytometer (BD Biosciences) and analyzed using FACSDiva software (BD Biosciences).

hBMSCs were plated at a density of 0.2 million cells in 6 well plates for 24 h and transduced with Adv-hVEGF-hIL-1Ra for 3 h at MOIs of 100 and 200. hBMSCs were

then washed thrice with PBS and subsequently cultured for 10 days. Cell culture media was collected every two days to estimate the expression of hVEGF and hIL-1Ra by ELISA. Total cellular RNA was isolated using an RNeasy mini kit (Qiagen, Valencia, CA) and the extracted RNA (1 μg) was reverse transcribed to generate the first strand cDNA. Two microliters of cDNA were used as a template and analyzed by SYBR Green-I dye universal PCR master mix on a LightCycler 480 Instrument. To assess the specificity of the amplified PCR product, melting curve analysis was performed on a LightCycler 480 Instrument. The results of stem cell markers (Nanog and Oct4) mRNA levels were compared by calculating the cross point value and normalized for GAPDH reference gene.

To determine the effect of Adv-hVEGF-hIL-1Ra transduction on hBMSCs differentiation, hBMSCs were cultured in MEM alpha media containing 10% FBS, 1% antibiotics (streptopmycin + penicillin), 1 μM dexamethasone, 0.5 mM 3-isobutyl- 1-methylxanthine, 0.2 mM indomethacin and 10 μg/ml insulin after transduction at 200 MOI for 3 h. Adipogenic differentiation media was replaced every 3–4 days for two weeks. Adipogenic differentiation of hBMSCs was assessed using Oil Red staining. For osteogenic differentiation, transduced hBMSCs were incubated at 50-70 percent confluence in MEM alpha media containing 10 M dexamethasone, 0.2 mM ascorbic acid mM and β-glycerolphosphate. The medium was replaced every 3–4 days for 21 days before fixing and Alizarin Red S staining.

5.2.3 Islet viability study

After transduction with Adv-hVEGF-hIL-1Ra at 200 MOI for 3 h, 5×10^5 hBMSCs were trypsinized (0.25%) and co-cultured with 500 IEs in a 10 cm dish of CMRL-1066

medium with 10% FBS for 2 days. The islet/hBMSCs co-culture was stimulated with cytokine cocktail (5 ng/ml IL-1β, 10 ng/ml TNF-α and 50 ng/ml IFN-γ) for 10 days and stained with 5 µg/ml calcein-AM and 2 µg/ ml propidium iodide for 30 min to assess islet viability under a fluorescent microscope.

Insulin production of human islets was quantified by the static insulin release method. Briefly, 500 IEs were cultured alone or with 5×10^5 untransduced or with 5×10^5 Adv-hVEGF-IL-1Ra transduced hBMSCs (200 MOI) in a 10 cm dish containing CMRL-1066 medium with 10% FBS for 10 days. Cytokine cocktail was added on day 2 and the islet/hBMSC co-culture was incubated with cytokine cocktail for 8 days. Insulin release from islets was measured at day 10 by sequentially stimulating islets with Kreb's buffer containing 2.5 mM (basal) and 22 mM glucose (stimulated) at 37°C for 1 h.

5.2.4 Islet transplantation

Animal experiments were performed in accordance with the NIH guidelines using a protocol approved by the Institutional Animal Care and Use Committee (IACUC) of the University of Tennessee Health Science Center. Diabetes was induced by intraperitoneal injection of low dose streptozotocin (STZ) (70mg/kg) to NSG mice for 2 consecutive days. Animals were classified as diabetic when two consecutive measurements of blood glucose were ≥ 400mg/dl with a glucometer. Prior to receiving human islets from the Integrated Islet Distribution Program distribution centers, hBMSCs were transduced with Adv-hVEGF-hIL-1Ra at an MOI of 200. Islets and hBMSCs were co-transplanted under the kidney capsules of STZ induced diabetic mice. Three shots of insulin (5U/kg) were given to each mouse on the first 3 days after transplantation to relieve the hyperglycemic stress to the newly-transplanted islets (207). The non-fasted glucose levels of all the mice were measured from the snipped

tail of each animal at 14.00 h during the first week after surgery and then weekly. At the end of study, the mice were anaesthetized by isoflurane inhalation to collect blood to measure human serum insulin and c-peptide levels by ELISA.

5.2.5 Intraperitoneal glucose tolerance test

Fifteen days after islet transplantation, glucose tolerance was determined in overnight-fasted mice, which were subjected to intraperitoneal injection of glucose at 2 g/kg of body weight (208). Blood samples were obtained from the snipped tail at 15, 30, 60, 90 and 120 min after injection and analyzed for glucose levels with a glucometer.

5.2.6 Immunofluorescence staining

Mice from each group were sacrificed at the end of study and the kidneys bearing islets were removed, washed with PBS, fixed in 4% paraformaldehyde overnight, and embedded in optimal cutting temperature (O.C.T.). Frozen sections of 10mm thickness were cut. To detect insulin positive human islets, the slides were stained with guinea pig anti-human insulin primary antibody (dilution 1:200) at 4 °C overnight and Alexa Fluor 568-conjugated goat anti-guinea pig secondary antibody (dilution 1:500) at room temperature for 1 h. To detect revascularization, the slides were stained with rabbit anti-human vWF primary antibody (dilution 1:500) at 4 °C overnight and Dylight 488-conjugated goat anti-rabbit secondary antibody (dilution 1:500) at room temperature for 1 h. Slides were counter-stained with DAPI.

5.2.7 Statistical analysis

Statistical significance of the difference between the two groups was determined by an unpaired Student's t-test and between several groups by one-way analysis of variance.

5.3 Results

5.3.1 Characterization, transduction and differentiation of hBMSCs

Flow cytometric analysis showed hBMSCs were positive for cell surface markers CD73, CD146, CD105, CD90 and Stro-1 (**Figure 5.1A**). Nanog, Oct4 and Sox 2 are known pluripotency markers and their expression indicates stem cell immaturity. Real Time RT-PCR data have shown that expression of these markers was not affected by the adenovirus transduction suggesting that hBMSCs can be used as gene delivery vehicles without affecting their stemness (**Figure 5.1B**).

Transduction of hBMSCs with Adv-hVEGF-hIL-1Ra resulted in significant overexpression of hVEGF and hIL-1Ra, which peaked at day 4 and gradually returned to basal levels at day 10 (**Figure 5.2 A & B**). We observed dose and time dependent expression of hVEGF and hIL-1Ra. Overexpression of transgenes is transient as adenoviral vector does not result in integration of genome.

Transduction of hBMSCs with adenovirus did not affect the differentiation potential of hBMSCs as evident from oil red staining of adipocytes from differentiated hBMSCs (**Figure 5.1C**). We did observe osteogenic differentiation of transduced hBMSCs, however it did affect osteogenic differentiation which was evident from the extent of area of alizarin red positive cells.
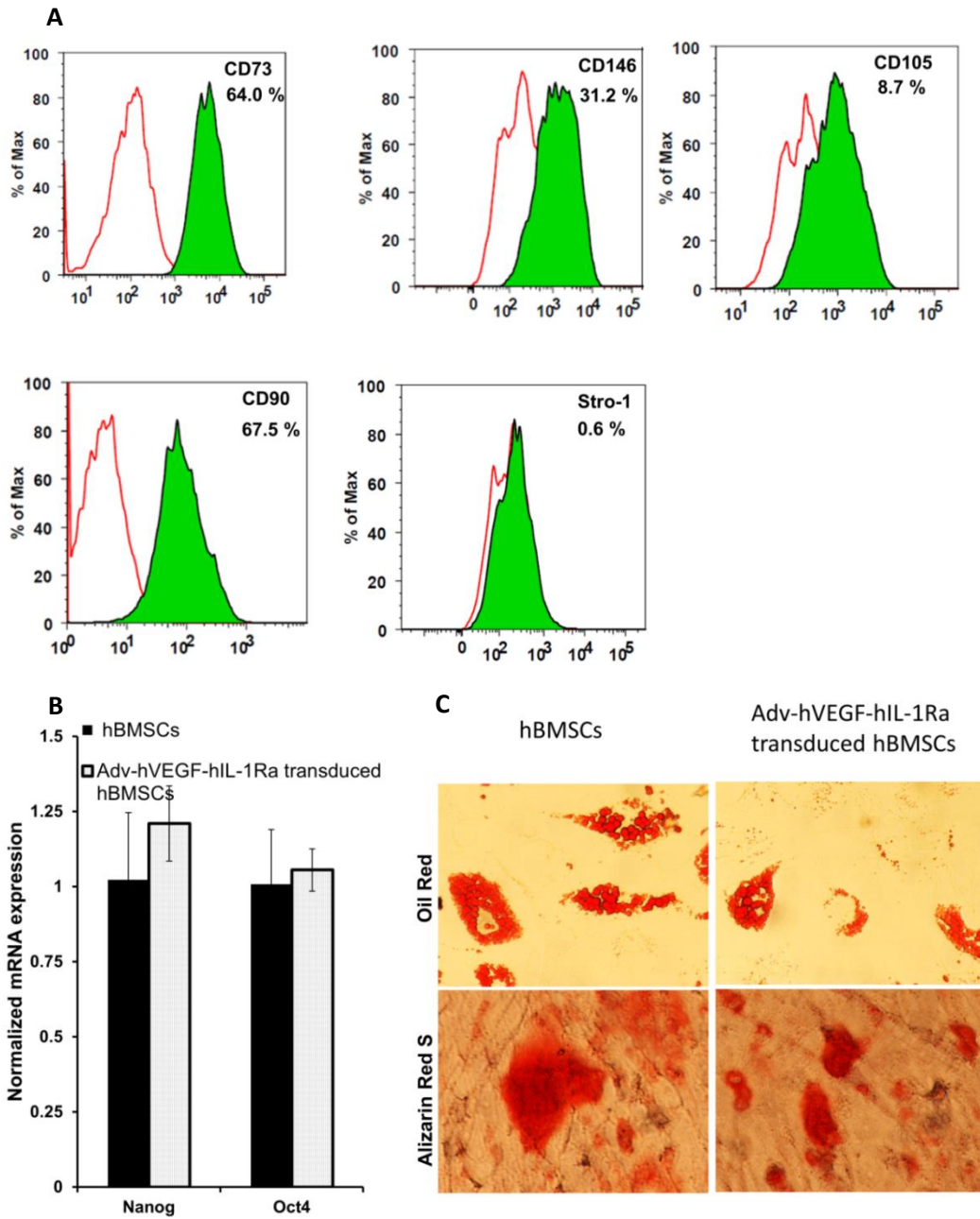
Figure 5-1. **Phenotypic characterization of cultured hBMSCs.**

(A) Flow cytometry analysis for expression of hBMSCs surface markers. hBMSCs are positive for CD73, CD146, CD105, CD90 and Stro1. Open peaks indicate the isotype of each cell and solid peaks represent expression of each marker. Numbers in the box specify the percentage of positive cells as compared to isotype control. (B) Expression of stem cell markers after transduction of hBMSCs with Adv-hVEGF-hIL-1Ra at 200 MOI. Real Time RT-PCR analysis to quantify change in the expression of Nanog and Oct4 stemness markers. Data are represented as the mean ± SD, n=3. (C) Differentiation of Adv-hVEGF-hIL-1Ra transduced hBMSCs. Oil red and alizarin red S staining of hBMSCs after culture in adipogenic and osteogenic differentiation media was performed respectively.
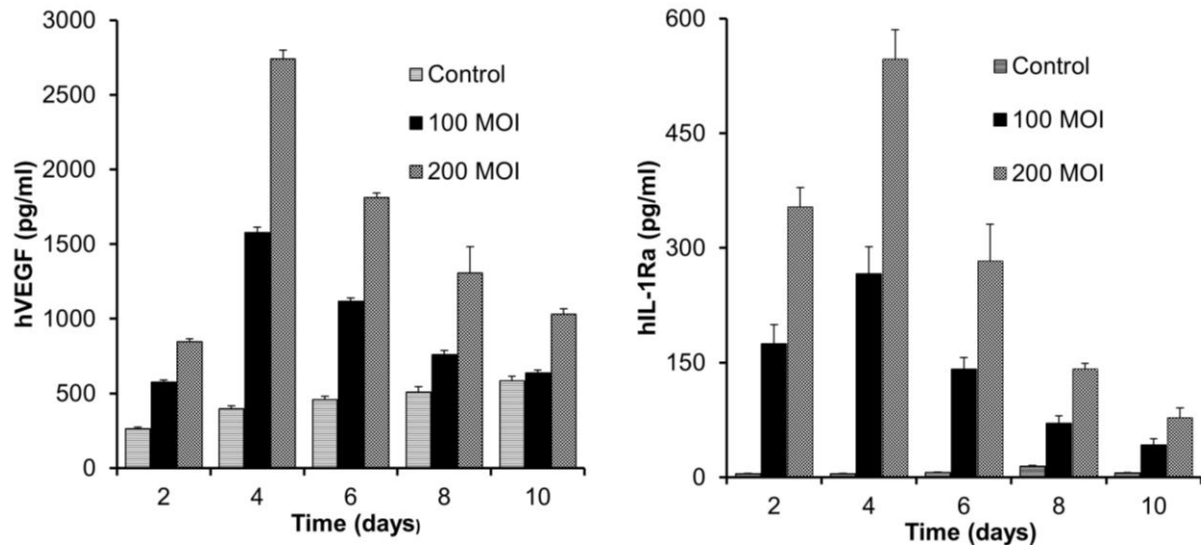
Figure 5-2.   Quantification of expression of (A) hVEGF and (B) hIL-1Ra after transduction of hBMSCs.

Expression of (A) hVEGF and (B) hIL-1Ra measured by ELISA after transduction of hBMSCs with Adv-hVEGF-hIL-1Ra at MOI of 100 and 200. Data are represented as the mean ± SD, n=3.

5.3.2 Islet viability study

PNF of islets after transplantation is the primary reason for the loss of islet function. Inflammatory cytokine cocktail was used to simulate PNF. Prevention of PNF of islets by hBMSCs overexpressing hIL-1Ra was measured by the membrane fluorescent staining method. Islets upon exposure to inflammatory cytokines showed significant cell death as evident from red PI staining in the core of islets (**Figure 5.3A**). We demonstrated that overexpression of hIL-1Ra by hBMSCs prevented the islet cell death as there are only few PI stained red cells in the islet. While hBMSCs reduced the level of islet cell death, overexpression of hIL-1Ra could significantly reduce the islet cell death (**Figure 5.3A**).

Islets alone upon culture for 10 days maintained insulin releasing function upon stimulation with glucose (SI =1.52). Co-culture of hBMSCs alone with islets could not prevent the islet cell death, resulting in the SI of insulin less than 1 (SI = 0.88) (**Figure 5.3B**). However, overexpression of hIL-1Ra by hBMSCs restored insulin release by the islets in response to stimulatory glucose concentrations (SI=1.53). Islet viability by membrane fluorescent staining and glucose stimulated insulin release assay have shown that overexpression of hIL-1Ra by hBMSCs could prevent the PNF and maintain insulin releasing function of islets to stimulatory glucose concentration.

A

Islets

Islets + hBMSCs

Islets + Adv -hVEGF-hIL-1Ra transduced hBMSCs

B
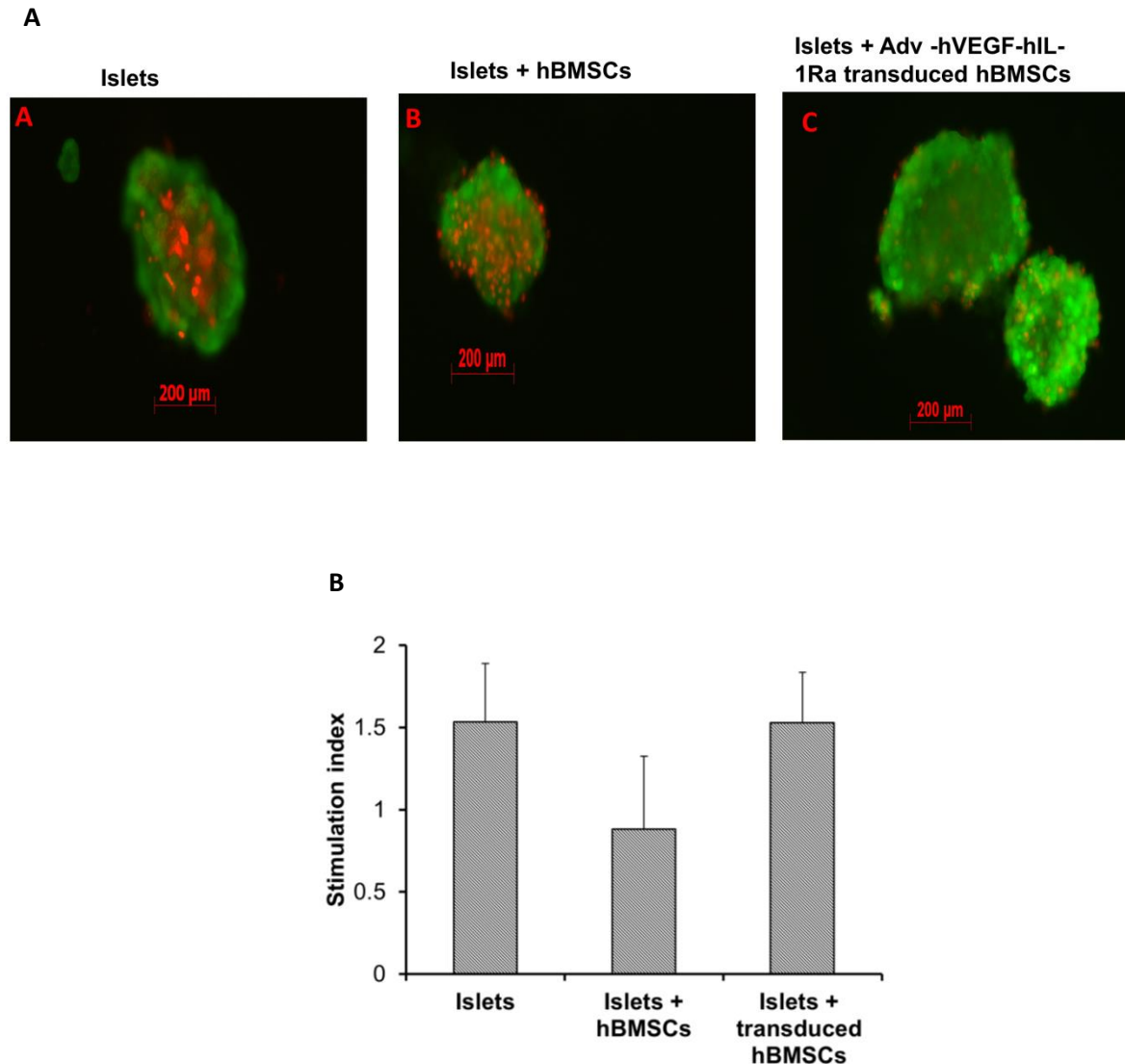
Figure 5-3.   Protection of islets by transduced hBMSCs against cytokines.

(A) Calcein AM and PI staining Islets, islets with hBMSCs and islets with transduced hBMSCs with Adv-hVEGF-hIL-1Ra at the ratio of 1 islet equivalent to 100 hBMSCs. (B) Stimulation index (SI) of human islets after incubation with inflammatory cytokine cocktail of 5 ng/ml IL-1β, 10 ng/ml TNF-α and 50 ng/ml IFN-γ for 10 days. Non-transduced islets were used as controls. SI was determined as the ratio of insulin released from islets when they are incubated in Kreb's buffer containing 22mM and 2.2 mM glucose. Data are presented as the mean ± SE (n=3)

5.3.3 Cotransplantation of hBMSCs overexpressing hVEGF and hIL-1Ra improved islet transplantation

Transplantation of 2000 islet equivalents (IEs) was able to reverse diabetes in all the transplanted animals. However, co-transplantation of islets with hBMSCs overexpressing hVEGF and hIL-1Ra resulted in better glycemic control in terms of the mean blood glucose level, duration of normoglycemia and response to glucose challenge. Islets alone could reverse diabetes only up to 21 days in most of the animals (**Figure 5.4A**). Although hBMSCs improved the islet transplantation outcome, there was still rapid increase in blood glucose level when untransduced hBMSCs were utilized. In contrast, co-transplantation of islets with Adv-hVEGF-hIL-1Ra transduced hBMSCs significantly increased the diabetes reversal ratio, suggesting the positive role of Adv-hVEGF-hIL-1Ra transduced hBMSCs on islet transplantation (**Figure 5.4D**). To determine the functional viability of islet grafts after islet transplantation, the mice were anesthetized to collect blood to measure human serum insulin and C-peptide levels by ELISA. The levels of human insulin and C-peptide of the mice co-transplanted with Adv-hVEGF-hIL-1Ra-transduced hBMSCs were significantly higher than those of the mice transplanted with islets alone (**Figure 5.5 C&D**).

This improvement in islet transplantation was confirmed by performing intraperitoneal glucose challenge. Blood glucose levels increased immediately after glucose (2 g/kg) injection, peaked at 15 min in all groups, and then decreased over time. Co-transplantation of islets with transduced hBMSCs showed accelerated glucose clearance resulting in lower blood glucose levels at 15 and 30 min post glucose injection (**Figure 5.5A**). Islets transplanted with Adv-hVEGF-hIL-1Ra transduced hBMSCs had a

better engraftment outcome and led to superior glucose control and tolerance compared to islets or islets with hBMSCs.

5.3.4 Immunofluorescence staining

Immunofluorescence staining of the kidney section bearing transplanted islets showed the engraftment of insulin-positive islets under the kidney capsule. vWF staining was performed to assess the extent of vascularization of islets. vWF staining was undetectable in the kidney sections bearing islets alone and sparse in the kidney sections bearing islets and un-transduced primary hBMSCs (**Figure 5.6 B**). However, vWF staining in the kidney sections bearing islets co-transplanted with Adv-hVEGF-hIL-1Ra transduced primary hBMSCs was detected. Analysis of human insulin and vWF immunofluorescence suggested increased revascularization of islets when co-transplanted with Adv-hVEGF-hIL-1Ra transduced primary hBMSCs (Figure 5.6 A&B).
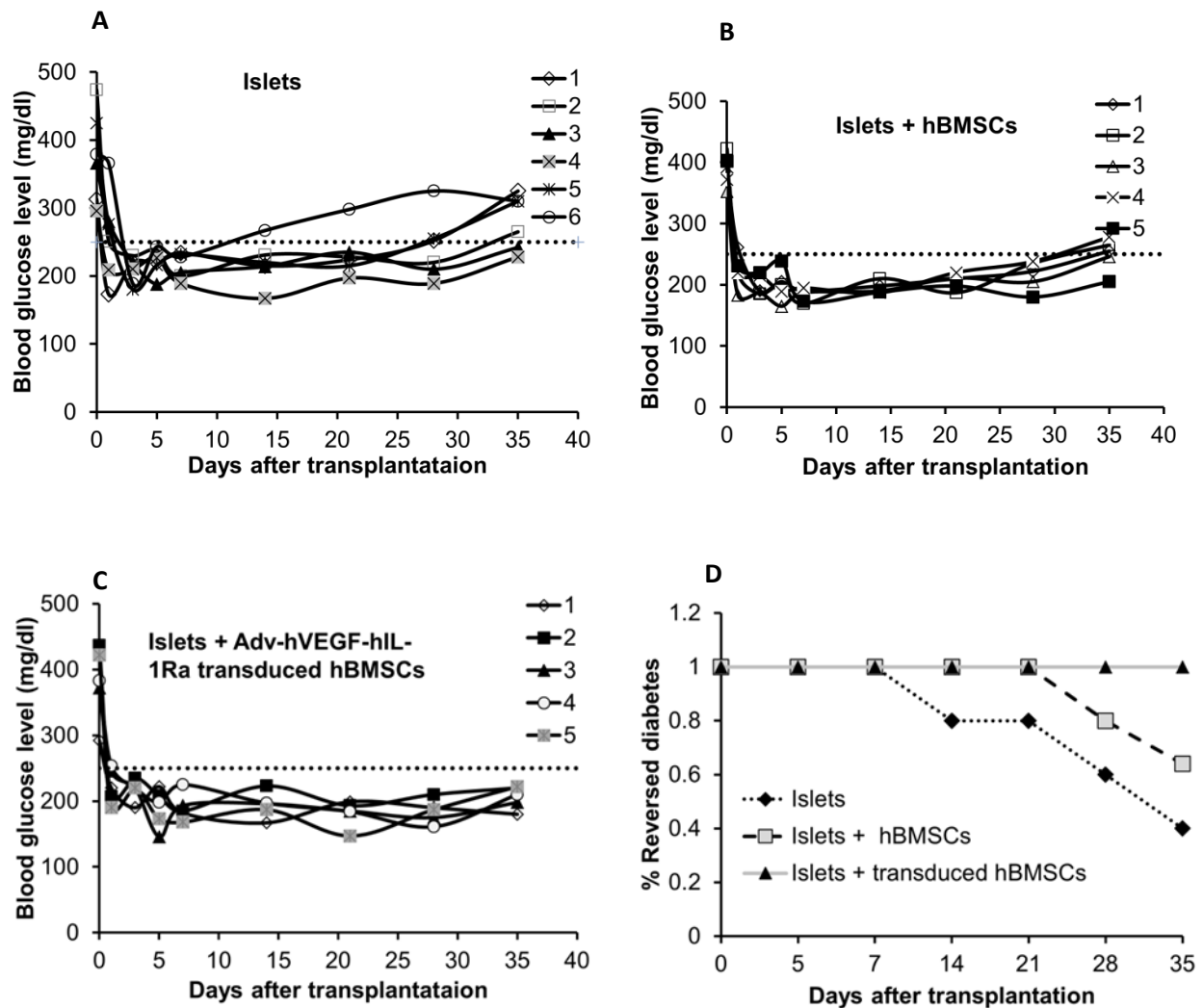
Figure 5-4. **Effect of Adv-hVEGF-hIL-1Ra transduced hBMSCs on the outcome of human islet transplantation.**

(A, B, C) The blood glucose level of every mouse after receiving 2000 human islet equivalent transplanted either alone or hBMSCs before or after transduction with Adv-hVEGF-hIL-1Ra (A-C). (D) Diabetes reversal ratio of the diabetic mice after human islet transplantation. Blood glucose ≤ 250 mg/dl (dashed line) was identified as reversed-diabetes (dashed line in A, B, C). Black triangles indicate mice receiving islets with Adv-hVEGF-hIL-1Ra transduced hBMSCs; Gray squares indicate mice receiving islets with hBMSCs; Black diamond's indicate mice receiving islets only.
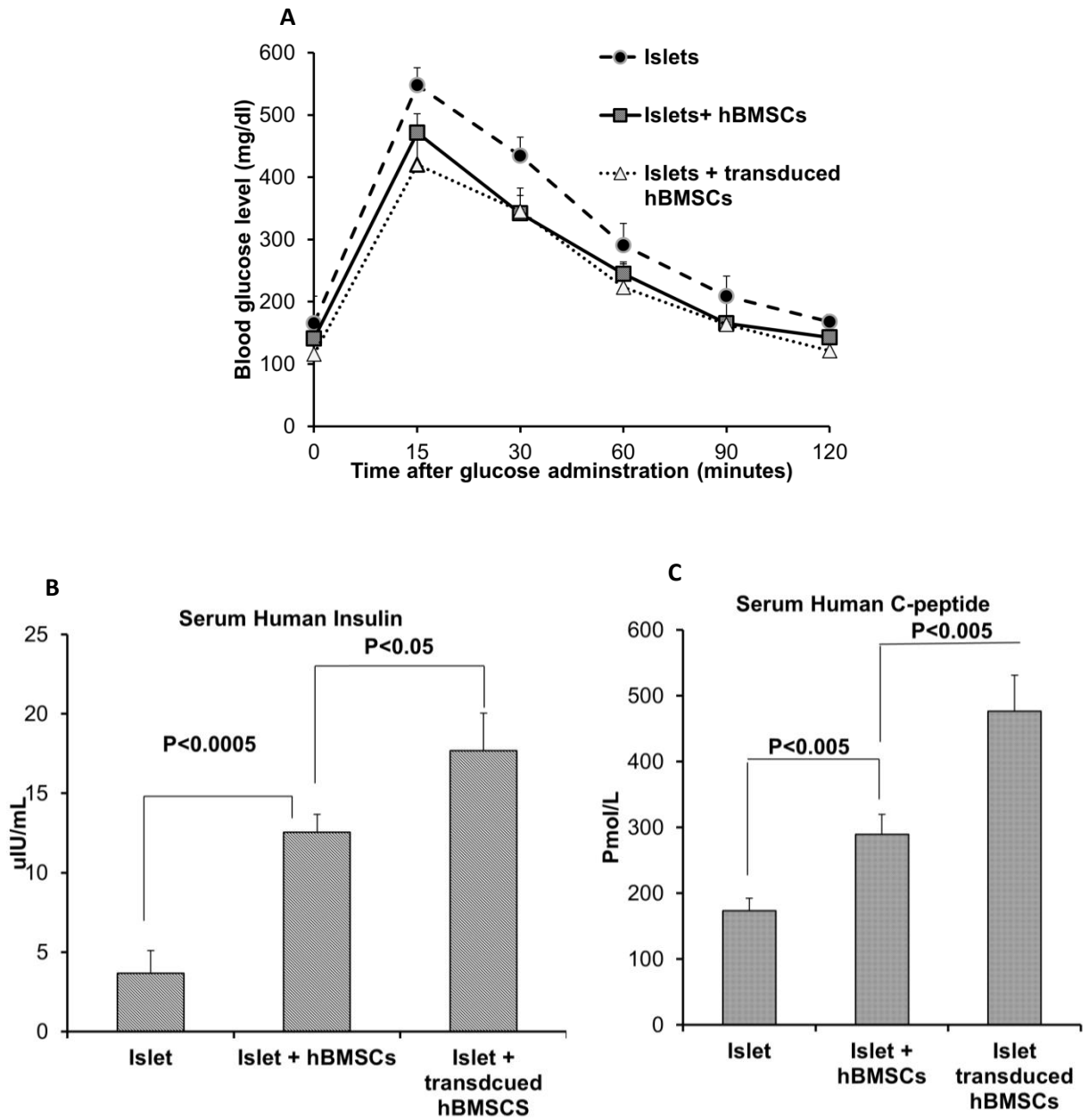
Figure 5-5. **Outcome of islet transplantation assessed by intraperitoneal glucose tolerance test and serum levels of human insulin and C-peptide.**

(A) Intraperitoneal glucose tolerance test after 15 days of islet transplantation by measuring blood glucose level. Data are presented as the mean ± SD (n=5). (B-C) Effect of Adv-hVEGF-hIL-1Ra transduced hBMSCs on human serum insulin and C-peptide levels of diabetic NSG mice transplanted with either islet alone or with hBMSCs only or with Adv-hVEGF-hIL-1Ra transduced hBMSCs at 35 days post transplantation. Data are presented as the mean ± SD, n=5. $P < 0.05$ under t-test.
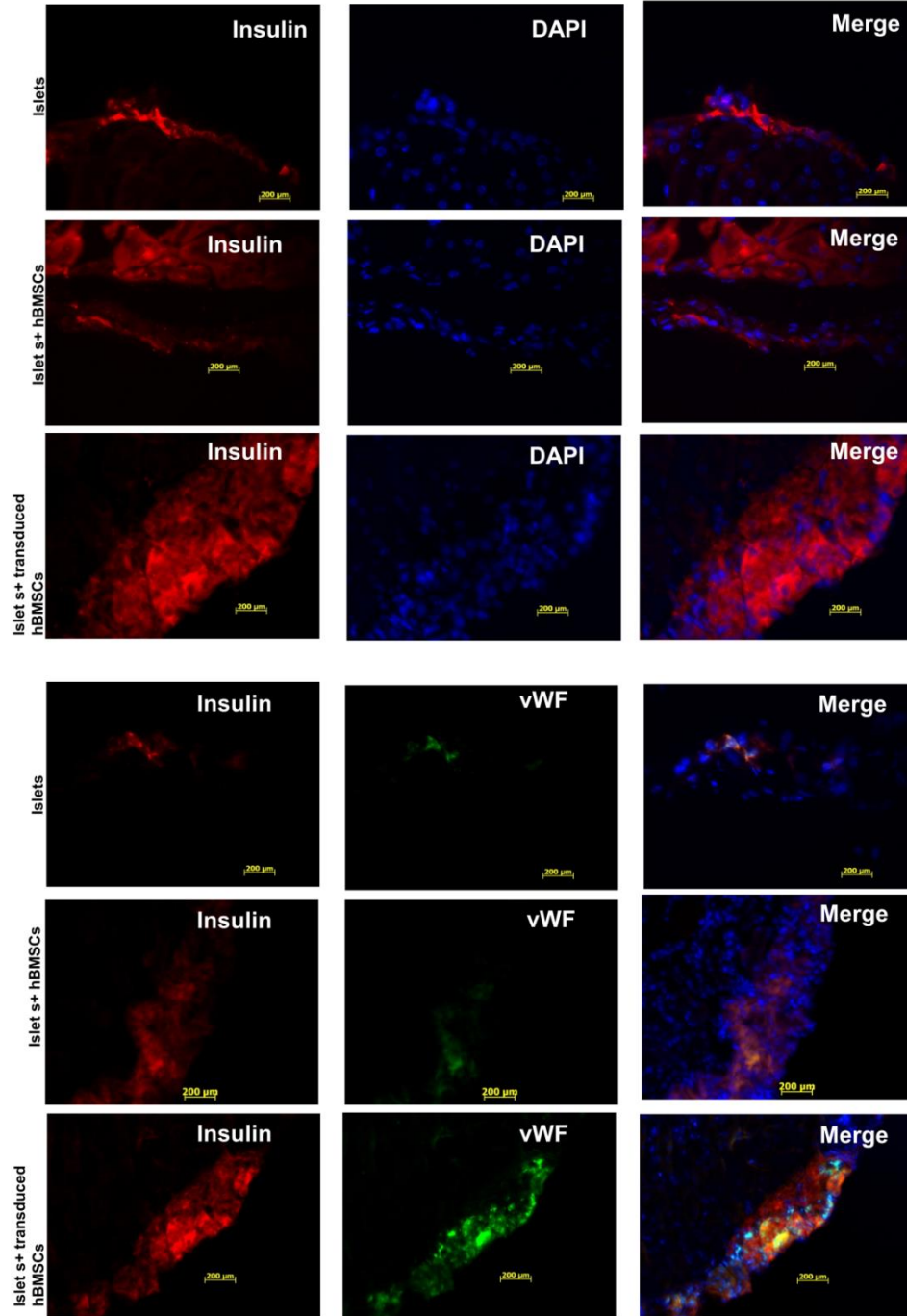
Figure 5-6. **Immunofluorescence staining of the kidney section for insulin and vWF 35 days after islet transplantation.**

Insulin was stained in red to indicate the functional human islets after transplantation. vWF was stained in green to indicate the revascularization of transplanted human islets. Kidney section of mice bearing human islets; human islets co-transplanted with hBMSCs; human islets co-transplanted with Adv-hVEGF-hIL-1Ra transduced hBMSCs.

111

5.4 Discussion

Type I diabetes is characterized by autoimmune destruction of islets and requires lifelong administration of insulin to maintain normoglycemeia. Since the success of Edmonton protocol, islet transplantation has been performed in many patients especially undergoing kidney transplantation (209). However, the proportion of recipients who achieved insulin independence is low and required supplemental administration of insulin to achieve normoglycemeia (210).

Majority of islets undergo apoptosis within a week or two after transplantation due to inflammatory reaction, mediated by inflammatory cytokines like IL-1β, TNF-α and IFN-γ released by infiltrating immune cells (211, 212). Among various inflammatory cytokines, IL-1β is the major inflammatory cytokine whose expression is upregulated during islet isolation procedure, culture and upon exposure to hyperglycemic conditions (213-215). Human islets exposed to IL-1β undergo NFkB activation, Fas upregulation and DNA fragmentation, eventually leading to β-cell death (216, 217). To prevent IL-1β induced β-cell apoptosis, human islets have been genetically modified to overexpress hIL-1Ra locally (196). Our group has also demonstrated that adenovirus mediated overexpression of hIL-1Ra can block IL-1β induced caspase activation, impaired glucose stimulated insulin release, and Fas triggered apoptosis (7, 206).

hBMSCs are heterogeneous population of cells and differ in clonogenicity, proliferation capacity and differentiation potential (218, 219). The International Society for Cell Therapy (ISCT) has proposed expression of cell surface markers CD73, CD90 and CD105 as minimum criteria to characterize hBMSCs (220). Stro-1 is a marker of early mesenchymal stromal precursor cells and strongly linked to hBMSCs colony

forming efficiency, plasticity and other paracrine signaling (221, 222). Level of expression of CD146 has been shown to correlate with the proliferation capacity of MSCs and their differentiation potential (220). Our flow cytometry data (Figure 5.1A) have shown that hBMSCs used in this study adhere to the minimum criteria set by ISCT and have high proliferation potential as evident by Stro-1 and CD146 expression.

hBMSCs can be readily transduced with all the known viral vectors and efficiently overexpress transgene (223, 224). Ease of isolation, absence of immuno co-stimulatory receptors, their immunomodulatory and anti-inflammatory properties make hBMSCs an ideal gene delivery vehicle (225). It is imperative to demonstrate that genetic modification of hBMSCs do not affect their differentiation potential, stemness, immunological properties and secretion of paracrine factors. Adipogenic differentiation of transduced hBMSCs as confirmed by Oil Red staining demonstrated that ex vivo modification of hBMSCs with adenovirus did not alter their differentiation potential (Figure 5.1C). However, we did observe reduction in the extent of osteogenic differentiation of transduced hBMSCs. This reduction in osteogenic differentiation of transduced hBMSCs could be attributed to paracrine effects of accumulated hVEGF and hIL-1Ra in the differentiation media. These results are different from previously published reports that genetic modification of MSCs did not affect their differentiation potential (226) and requires consideration of the effect of accumulated paracrine factors on the differentiation of genetically modified hBMSCs. Tracy et al have also shown that adenovirus transduction of BMSCs did not adversely affect their immunological properties as well as expression of chemokines and chemokine receptors (227). However, they did not determine the effect of genetic modification on stemness as

113

measured by expression of Nanog and Oct4 genes which are the key transcription factors for maintaining pluripotency and self-renewal potential of undifferentiated embryonic stem cells (228). Forced expression of Nanog or Sox2 maintained the expansion and differentiation potential of MSCs (229). Here we have shown that adenovirus modification of hBMSCs did not alter the expression of Nanog and Oct4 (Figure 5.1B). In addition, previously we have shown that transduction of hBMSCs did not alter their paracrine secretions (230). Our results indicate that adenoviral modification of hBMSCs do not alter their proliferation, differentiation potential, expression of surface markers, immunological properties, stemness, and therefore hBMSCs have the potential to be used as gene delivery vehicles.

MSCs as cell therapy has demonstrated efficacy both in the treatment of type 1 diabetes and islet transplantation (231-234). There are conflicting reports whether hBMSCs undergo transdifferentiation to insulin secreting β cells or hBMSCs prevent islet apoptosis through the secretion of growth factors. Ito et al. have shown that secretion of VEGF by BMSCs improved islet revascularization and thereby islet transplantation (233). hBMSCs secrete an array of angiogenesis growth factors which promote islet vascularization and islet growth (235). However, basal secretion of VEGF (Figure 5.2A) and other growth factors by hBMSCs is not enough to support the revascularization of islet graft soon after transplantation. Similarly, secretion of IL-1Ra by MSCs alone could not abrogate IL-1β mediated inflammation. Therefore, lentiviral modification of MSCs to overexpress IL-1Ra has been performed to enhance their anti-inflammatory potential (236).

In this study, we have shown that hBMSCs can be genetically modified with bicistronic adenoviral vector to promote islet revascularization and prevent islet apoptosis. Considering the safety, transduction efficiency and duration of transgene expression, adenovirus was preferred over retrovirus and plasmid DNA. Ex vivo genetic modification of hBMSCs resulted in significant co-expression of hVEGF and hIL-1Ra (Figure 5.2 A & B). This pattern of transgene expression is desirable as islet apoptosis occurs immediately after transplantation. hBMSCs and islets can be either co-cultured together or separated through a cell culture insert. We have co-cultured islet and hBMSCs together as reported previously by Duprez et. al (237). Genetically modified hBMSCs co-cultured with islets protected islets against inflammatory cytokines and improve the islet viability as evident from Calcein AM/PI staining (Figure 5.3A).

To determine whether co-transplantation of human islets with Adv-hVEGF-hIL-1Ra transduced hBMSCs can improve the outcome of islet transplantation, mean blood glucose levels were measured in NSG diabetic mouse model after transplantation of islets alone or with hBMSCs or with Adv-hVEGF-hIL-1Ra transduced hBMSCs (Figure 5.4). Co-transplantation of Adv-hVEGF-hIL-1Ra transduced hBMSCs significantly improved diabetic reversal ratio and response to intra peritoneal glucose challenge (Figure 5.4 & 5.5A). hvWF factor staining as marker of endothelial cell proliferation was more evident in Adv-hVEGF-hIL-1Ra transduced hBMSCs (Figure 5.6). Prominent green staining in Adv-hVEGF-hIL-1Ra transduced hBMSCs indicates that expression of hVEGF enhanced the endothelial cell proliferation of transplanted islet. To correlate the advantage of islet revascularization with the islet mass in the kidney capsule, we also stained for human insulin. Co transplantation of islet with Adv-hVEGF-hIL-1Ra

115

transduced hBMSCs displayed significantly higher levels of insulin content than untransduced hBMSCs or islet alone (Figure 5.6). These findings correlated well with serum human insulin and C-peptide levels (Figure 5.5 B&C) and immunofluorescent staining (Figure 5.6). In conclusion, our results have demonstrated that hBMSCs can be used as gene delivery vehicles without affecting their stemness and differentiation potential. Over expression of VEGF and IL-1Ra protected islet viability, promoted revascularization and significantly improved the glycemic control in diabetic mice model.

Chapter 6 SUMMARY AND FUTURE RESEARCH

6.1 Summary

Melanoma originated from malignant transformation of melanocytes is highly aggressive cancer with multi drug resistance and poor prognosis. Melanocytes proliferate upon exposure to UV radiation and this tendency of melanocytes to survive and proliferate under stress programs them to survive. Additionally, the mutation of oncogene and tumor suppressors which include BRAF, NRAS, Kit and so on drives the process of melanomagenesis. Despite the improvement in survival with the recent advances in targeted therapy (e.g. BRAF inhibitors vemurafenib and dabrafenib; MEK inhibitor trametinib), acquired drug resistance often develops within a few months and the overall survival for malignant melanoma remains low. Therefore, there is an urgent need to develop more effective treatment modalities for treating malignant melanoma. This dissertation is focused on developing and investigating nanocarriers based delivery of photodynamic agent and tubulin binding agents for treatment of melanoma.

Tumor specific localization of photosensitizer and deep tissue penetration of light is essential for application of phototherapy. ICG with absorption in the NIR range with excellent safety profile is a suitable candidate for phototherapy but its clinical potential for phototherapy is limited by short half-life and inefficient tumor accumulation. To improve biodistribution and efficacy of ICG based phototherapy, we designed polymeric micelles of ICG. Amino derivative of ICG was synthesized and characterized for its conjugation to polymeric backbone and its formulation as micelles. Amphiphillic copolymer, poly (ethylene glycol)-block-poly(2- methyl-2-carboxyl-propylene carbonate) (PEG-PCC) with pendant carboxyl group was synthesized for conjugation of amino ICG. Polymeric micelles formulated from ICG polymer conjugate exhibited mean particle size

of 30-50 nm size and drug loading of 10.2%. Micellar formulation demonstrated significant in vitro photothernal cytotoxicity upon irradiation at 800 nm. Unlike micelles, ICG solution exhibited photodynamic toxicity which can be reversed by sodium azide. This contrasting mechanism of cytotoxicity of ICG micelles and ICG solution was elucidated by poor cellular uptake of ICG micelles. ICG conjugated micelles prolonged its circulation and increased tumor accumulation through enhanced permeability and retention effect resulting in complete tumor regression upon irradiation of ICG conjugated micelles compared to free ICG and control in a A375 human melanoma tumor model in athymic nude mice. In vivo NIR fluorescence imaging and efficacy data showed that we were able to design ICG conjugated micelles with excellent in vivo stability which resulted in prolonged plasma circulation and enhanced tumor accumulation with significant efficacy in melanoma.

LY293, a 5 indole derivative tubulin binding agent was synthesized with nanomolar efficacy to overcome Pgp mediated drug resistance. However, poor aqueous solubility of LY293 warranted use of toxic cosolvents for its systemic therapy. Biodegradable polymer with polyester and polycarbonate hydrophobic core was synthesized for systemic therapy of nanoparticulate formulation of LY293. Methoxy polyethylene glycol-b-poly (carbonate-co-lactide) (mPEG-b-P (CB-co-LA)) random copolymer was synthesized and characterized by ^{1}H NMR and GPC. Polymeric nanoparticles formulated using o/w emulsification method had appreciable LY293 loading with no loss of in vitro cytotoxicity as compared to free drug. In vivo, systemic administration of LY293 loaded nanoparticles significantly inhibited the proliferation of metastatic melanoma in syngeneic lung metastasis melanoma mouse model.

Primary non-function of islets and graft rejections remains key obstacles for successful human islet transplantation. We utilized hBMSCs as a novel gene carrier to express two therapeutic genes while avoiding the viral transduction on human islets. hBMSCs transduced with bicistronic adenoviral vectors encoding VEGF and IL-1Ra overexpressed these transgenes to promote revascularization of islets and protect the islets from immune mediated destruction. Genetically modified hBMSCs protected viability of islets against cytokine cocktail as confirmed by live/dead staining. Upon cotransplantation of islets with transduced hBMSCs demonstrated better glycemic control as compared to mice transplanted with islets alone or islets cotransplanted hBMSCs. There was also an associated increase in the serum levels of insulin and c-peptide which was supported by immunofluorescent staining of kidney sections for insulin and human von Willebrand factor (marker for endothelial cells) in islets cotransplanted with genetically modified hBMSCs group. In conclusion, our results demonstrate that hBMSCs may be used as gene carriers and nursing cells to improve the outcome of islet transplantation.

6.2 Future Directions

The findings presented in this thesis demonstrated proof of principle that micelles formulation of ICG improved its plasma circulation and tumor accumulation through EPR effect. Cell uptake and cytotoxicity mechanistic studies demonstrated that polymer conjugated ICG micelles formulation have poor cellular uptake. To improve the cellular uptake of ICG micelles, we would like to explore physical encapsulation as well as conjugation of ICG to the polymeric backbone by tumor overexpressed protease selective peptide (238-240). Moreover, photodynamic property of ICG can also be utilized for photochemical internilzation (155). Reactive oxygen species generated by

photodynamic therapy led to rupture of endosomal membrane and cytosolic release of endosomes entrapped drugs and macromolecules. We would like to evaluate combination of photodynamic therapy and chemotherapeutic agent for the treatment of melanoma (241, 242).

In chapter 4, we have demonstrated that LY293, tubulin inhibitor showed excellent efficacy in lung metastasis melanoma model. However, there was lack of significant difference between nanoparticulate formulation and cosolvent solution of LY293 which may be due to premature release of the encapsulated drug from the nanoparticle core. We would like to perform pharmacokinetic and biodistribution to study difference in plasma profile of nanoparticulate formulation and cosolvent solution. In addition, we would also like to explore alternative nanoparticulate formulation approaches to minimize the premature LY293 release from nanoparticles and further improve the tumor accumulation. Polymeric drug conjugates have been shown to be stable in the circulation resulting in enhanced tumor accumulation. For future studies, we plan to redesign the polymeric nanocarriers as well as synthesize drug analogs with function groups for chemical conjugation which will allow preferential tumor accumulation and reduction of peripheral toxicity on systemic administration.

We demonstrated use of human bone marrow derived mesenchymal stem cells as gene delivery vehicles. Genetically modified hBMSCs improved islet viability against inflammatory cytokines and promoted revascularization of transplanted grafts. However, the level of expression of transgene was significantly lower as compared to genetic modification of islets which can be attributed to low expression of coxsackievirus and adenovirus receptor (CAR) by hBMSCs (243). To improve the transduction

efficiency and increase the transgene expression, we would like to use cationic polymers, peptides or modify the surface of adenovirus for targeting receptors expressed by hBMSCs (244-246). hBMSCs have strong immunosuppressive effect and tropic effect. Further studies evaluating the immunosuppressive effect of genetically modified stem cells will be evaluated in humanized mouse model. Evaluation of efficacy of contransplantation islet with genetically modified hBMSCs in humanized mouse model could be a perfect model and use of humanized mouse model is warranted to assess the islet transplantation in preclinical models.

REFERENCESReferences

1. Bhatia S, Tykodi SS, Thompson JA. Treatment of metastatic melanoma: an overview. Oncology (Williston Park). 2009 May;23(6):488-96.

2. Gray-Schopfer V, Wellbrock C, Marais R. Melanoma biology and new targeted therapy. Nature. 2007 Feb 22;445(7130):851-7.

3. Sun C, Wang L, Huang S, Heynen GJ, Prahallad A, Robert C, et al. Reversible and adaptive resistance to BRAF(V600E) inhibition in melanoma. Nature. 2014 Apr 3;508(7494):118-22.

4. Dummer R, Flaherty KT. Resistance patterns with tyrosine kinase inhibitors in melanoma: new insights. Curr Opin Oncol. 2012 Mar;24(2):150-4.

5. Chang W, Lee SJ, Park S, Choi MK, Hong JY, Kim YS, et al. Effect of paclitaxel/carboplatin salvage chemotherapy in noncutaneous versus cutaneous metastatic melanoma. Melanoma Res. 2013 Apr;23(2):147-51.

6. Lu Y, Li CM, Wang Z, Chen J, Mohler ML, Li W, et al. Design, synthesis, and SAR studies of 4-substituted methoxylbenzoyl-aryl-thiazoles analogues as potent and orally bioavailable anticancer agents. J Med Chem. 2011 Jul 14;54(13):4678-93.

7. Panakanti R, Mahato RI. Bipartite vector encoding hVEGF and hIL-1Ra for ex vivo transduction into human islets. Mol Pharm. 2009 Jan-Feb;6(1):274-84.

8. Wu H, Yoon AR, Li F, Yun CO, Mahato RI. RGD peptide-modified adenovirus expressing hepatocyte growth factor and X-linked inhibitor of apoptosis improves islet transplantation. J Gene Med. 2011 Dec;13(12):658-69.

9. Zhang N, Schroppel B, Chen D, Fu S, Hudkins KL, Zhang H, et al. Adenovirus transduction induces expression of multiple chemokines and chemokine receptors in murine beta cells and pancreatic islets. Am J Transplant. 2003 Oct;3(10):1230-41.

10. Garbe C, Eigentler TK, Keilholz U, Hauschild A, Kirkwood JM. Systematic review of medical treatment in melanoma: current status and future prospects. Oncologist. 2011;16(1):5-24.

11. Erdei E, Torres SM. A new understanding in the epidemiology of melanoma. Expert Rev Anticancer Ther. 2010 Nov;10(11):1811-23.

12. Nazarian R, Shi H, Wang Q, Kong X, Koya RC, Lee H, et al. Melanomas acquire resistance to B-RAF(V600E) inhibition by RTK or N-RAS upregulation. Nature. 2010 Dec 16;468(7326):973-7.

13. Jordan MA, Wilson L. Microtubules as a target for anticancer drugs. Nat Rev Cancer. 2004 Apr;4(4):253-65.

14. Stanton RA, Gernert KM, Nettles JH, Aneja R. Drugs that target dynamic microtubules: a new molecular perspective. Med Res Rev. 2011 May;31(3):443-81.

15. Singh P, Rathinasamy K, Mohan R, Panda D. Microtubule assembly dynamics: an attractive target for anticancer drugs. IUBMB Life. 2008 Jun;60(6):368-75.

16. Lu Y, Chen J, Xiao M, Li W, Miller DD. An overview of tubulin inhibitors that interact with the colchicine binding site. Pharm Res. 2012 Nov;29(11):2943-71.

17. Lu Y, Li CM, Wang Z, Ross CR,2nd, Chen J, Dalton JT, et al. Discovery of 4-substituted methoxybenzoyl-aryl-thiazole as novel anticancer agents: synthesis, biological evaluation, and structure-activity relationships. J Med Chem. 2009 Mar 26;52(6):1701-11.

18. Li F, Lu Y, Li W, Miller DD, Mahato RI. Synthesis, formulation and in vitro evaluation of a novel microtubule destabilizer, SMART-100. J Control Release. 2010 Apr 2;143(1):151-8.

19. Li CM, Wang Z, Lu Y, Ahn S, Narayanan R, Kearbey JD, et al. Biological activity of 4-substituted methoxybenzoyl-aryl-thiazole: an active microtubule inhibitor. Cancer Res. 2011 Jan 1;71(1):216-24.

20. Li CM, Chen J, Lu Y, Narayanan R, Parke DN, Li W, et al. Pharmacokinetic optimization of 4-substituted methoxybenzoyl-aryl-thiazole and 2-aryl-4-benzoyl-imidazole for improving oral bioavailability. Drug Metab Dispos. 2011 Oct;39(10):1833-9.

21. O'Brien ME, Wigler N, Inbar M, Rosso R, Grischke E, Santoro A, et al. Reduced cardiotoxicity and comparable efficacy in a phase III trial of pegylated liposomal doxorubicin HCl (CAELYX/Doxil) versus conventional doxorubicin for first-line treatment of metastatic breast cancer. Ann Oncol. 2004 Mar;15(3):440-9.

22. Rademaker-Lakhai JM, Crul M, Zuur L, Baas P, Beijnen JH, Simis YJ, et al. Relationship between cisplatin administration and the development of ototoxicity. J Clin Oncol. 2006 Feb 20;24(6):918-24.

23. Allen TM, Cullis PR. Drug delivery systems: entering the mainstream. Science. 2004 Mar 19;303(5665):1818-22.

24. Torchilin VP, Lukyanov AN. Peptide and protein drug delivery to and into tumors: challenges and solutions. Drug Discov Today. 2003 Mar 15;8(6):259-66.

25. Matsumura Y, Maeda H. A new concept for macromolecular therapeutics in cancer chemotherapy: mechanism of tumoritropic accumulation of proteins and the antitumor agent smancs. Cancer Res. 1986 Dec;46(12 Pt 1):6387-92.

26. Noguchi Y, Wu J, Duncan R, Strohalm J, Ulbrich K, Akaike T, et al. Early phase tumor accumulation of macromolecules: a great difference in clearance rate between tumor and normal tissues. Jpn J Cancer Res. 1998 Mar;89(3):307-14.

27. Yokoyama M, Miyauchi M, Yamada N, Okano T, Sakurai Y, Kataoka K, et al. Characterization and anticancer activity of the micelle-forming polymeric anticancer drug adriamycin-conjugated poly(ethylene glycol)-poly(aspartic acid) block copolymer. Cancer Res. 1990 Mar 15;50(6):1693-700.

28. Yoo HS, Park TG. Biodegradable polymeric micelles composed of doxorubicin conjugated PLGA-PEG block copolymer. J Control Release. 2001 Jan 29;70(1-2):63-70.

29. Liu J, Zeng F, Allen C. In vivo fate of unimers and micelles of a poly(ethylene glycol)-block-poly(caprolactone) copolymer in mice following intravenous administration. Eur J Pharm Biopharm. 2007 Mar;65(3):309-19.

30. Ramaswamy M, Zhang X, Burt HM, Wasan KM. Human plasma distribution of free paclitaxel and paclitaxel associated with diblock copolymers. J Pharm Sci. 1997 Apr;86(4):460-4.

31. Soppimath KS, Aminabhavi TM, Kulkarni AR, Rudzinski WE. Biodegradable polymeric nanoparticles as drug delivery devices. J Control Release. 2001 Jan 29;70(1-2):1-20.

32. Gaucher G, Dufresne MH, Sant VP, Kang N, Maysinger D, Leroux JC. Block copolymer micelles: preparation, characterization and application in drug delivery. J Control Release. 2005 Dec 5;109(1-3):169-88.

33. Gaucher G, Marchessault RH, Leroux JC. Polyester-based micelles and nanoparticles for the parenteral delivery of taxanes. J Control Release. 2010 Apr 2;143(1):2-12.

34. Kim S, Shi Y, Kim JY, Park K, Cheng JX. Overcoming the barriers in micellar drug delivery: loading efficiency, in vivo stability, and micelle-cell interaction. Expert Opin Drug Deliv. 2010 Jan;7(1):49-62.

35. Lavasanifar A, Samuel J, Kwon GS. Poly(ethylene oxide)-block-poly(L-amino acid) micelles for drug delivery. Adv Drug Deliv Rev. 2002 Feb 21;54(2):169-90.

36. Liu J, Xiao Y, Allen C. Polymer-drug compatibility: a guide to the development of delivery systems for the anticancer agent, ellipticine. J Pharm Sci. 2004 Jan;93(1):132-43.

37. Latere Dwan'Isa JP, Rouxhet L, Preat V, Brewster ME, Arien A. Prediction of drug solubility in amphiphilic di-block copolymer micelles: the role of polymer-drug compatibility. Pharmazie. 2007 Jul;62(7):499-504.

38. Forrest ML, Zhao A, Won CY, Malick AW, Kwon GS. Lipophilic prodrugs of Hsp90 inhibitor geldanamycin for nanoencapsulation in poly(ethylene glycol)-b-poly(epsilon-caprolactone) micelles. J Control Release. 2006 Nov 28;116(2):139-49.

39. Marsac PJ, Shamblin SL, Taylor LS. Theoretical and practical approaches for prediction of drug-polymer miscibility and solubility. Pharm Res. 2006 Oct;23(10):2417-26.

40. Danquah M, Fujiwara T, Mahato RI. Self-assembling methoxypoly(ethylene glycol)-b-poly(carbonate-co-L-lactide) block copolymers for drug delivery. Biomaterials. 2010 Mar;31(8):2358-70.

41. Mundra V, Lu Y, Danquah M, Li W, Miller DD, Mahato RI. Formulation and characterization of polyester/polycarbonate nanoparticles for delivery of a novel microtubule destabilizing agent. Pharm Res. 2012 Nov;29(11):3064-74.

42. Li F, Danquah M, Mahato RI. Synthesis and characterization of amphiphilic lipopolymers for micellar drug delivery. Biomacromolecules. 2010 Oct 11;11(10):2610-20.

43. Mahmud A, Patel S, Molavi O, Choi P, Samuel J, Lavasanifar A. Self-associating poly(ethylene oxide)-b-poly(alpha-cholesteryl carboxylate-epsilon-caprolactone) block copolymer for the solubilization of STAT-3 inhibitor cucurbitacin I. Biomacromolecules. 2009 Mar 9;10(3):471-8.

44. Kataoka K, Matsumoto T, Yokoyama M, Okano T, Sakurai Y, Fukushima S, et al. Doxorubicin-loaded poly(ethylene glycol)-poly(beta-benzyl-L-aspartate) copolymer micelles: their pharmaceutical characteristics and biological significance. J Control Release. 2000 Feb 14;64(1-3):143-53.

45. Deng X, Xu X, Lai Y, He B, Gu Z. Novel nanoparticles generated by polymeric amphiphiles with pi-pi conjugated small molecules for anti-tumor drug delivery. J Biomed Nanotechnol. 2013 Aug;9(8):1336-44.

46. Lai Y, Long Y, Lei Y, Deng X, He B, Sheng M, et al. A novel micelle of coumarin derivative monoend-functionalized PEG for anti-tumor drug delivery: in vitro and in vivo study. J Drug Target. 2012 Apr;20(3):246-54.

47. Shi Y, van Steenbergen MJ, Teunissen EA, Novo L, Gradmann S, Baldus M, et al. Pi-pi stacking increases the stability and loading capacity of thermosensitive polymeric micelles for chemotherapeutic drugs. Biomacromolecules. 2013 Jun 10;14(6):1826-37.

48. Lee J, Lee SC, Acharya G, Chang CJ, Park K. Hydrotropic solubilization of paclitaxel: analysis of chemical structures for hydrotropic property. Pharm Res. 2003 Jul;20(7):1022-30.

49. Kim JY, Kim S, Papp M, Park K, Pinal R. Hydrotropic solubilization of poorly water-soluble drugs. J Pharm Sci. 2010 Sep;99(9):3953-65.

50. Eckman AM, Tsakalozou E, Kang NY, Ponta A, Bae Y. Drug release patterns and cytotoxicity of PEG-poly(aspartate) block copolymer micelles in cancer cells. Pharm Res. 2012 Jul;29(7):1755-67.

51. Kim JO, Kabanov AV, Bronich TK. Polymer micelles with cross-linked polyanion core for delivery of a cationic drug doxorubicin. J Control Release. 2009 Sep 15;138(3):197-204.

52. Gaucher G, Dufresne MH, Sant VP, Kang N, Maysinger D, Leroux JC. Block copolymer micelles: preparation, characterization and application in drug delivery. J Control Release. 2005 Dec 5;109(1-3):169-88.

53. Ye L, Letchford K, Heller M, Liggins R, Guan D, Kizhakkedathu JN, et al. Synthesis and characterization of carboxylic acid conjugated, hydrophobically derivatized, hyperbranched polyglycerols as nanoparticulate drug carriers for cisplatin. Biomacromolecules. 2011 Jan 10;12(1):145-55.

54. Tian Y, Ravi P, Bromberg L, Hatton TA, Tam KC. Synthesis and aggregation behavior of pluronic F87/poly(acrylic acid) block copolymer in the presence of doxorubicin. Langmuir. 2007 Feb 27;23(5):2638-46.

55. Giacomelli C, Schmidt V, Borsali R. Specific interactions improve the loading capacity of block copolymer micelles in aqueous media. Langmuir. 2007 Jun 19;23(13):6947-55.

56. Hamaguchi T, Matsumura Y, Suzuki M, Shimizu K, Goda R, Nakamura I, et al. NK105, a paclitaxel-incorporating micellar nanoparticle formulation, can extend in vivo antitumour activity and reduce the neurotoxicity of paclitaxel. Br J Cancer. 2005 Apr 11;92(7):1240-6.

57. Zhao X, Poon Z, Engler AC, Bonner DK, Hammond PT. Enhanced stability of polymeric micelles based on postfunctionalized poly(ethylene glycol)-b-poly(gamma-propargyl L-glutamate): the substituent effect. Biomacromolecules. 2012 May 14;13(5):1315-22.

58. Kim SH, Tan JP, Nederberg F, Fukushima K, Colson J, Yang C, et al. Hydrogen bonding-enhanced micelle assemblies for drug delivery. Biomaterials. 2010 Nov;31(31):8063-71.

59. Duncan R, Vicent MJ. Do HPMA copolymer conjugates have a future as clinically useful nanomedicines? A critical overview of current status and future opportunities. Adv Drug Deliv Rev. 2010 Feb 17;62(2):272-82.

60. Etrych T, Kovar L, Strohalm J, Chytil P, Rihova B, Ulbrich K. Biodegradable star HPMA polymer-drug conjugates: Biodegradability, distribution and anti-tumor efficacy. J Control Release. 2011 Sep 25;154(3):241-8.

61. Fox ME, Szoka FC, Frechet JM. Soluble polymer carriers for the treatment of cancer: the importance of molecular architecture. Acc Chem Res. 2009 Aug 18;42(8):1141-51.

62. Peterson JJ, Meares CF. Cathepsin substrates as cleavable peptide linkers in bioconjugates, selected from a fluorescence quench combinatorial library. Bioconjug Chem. 1998 Sep-Oct;9(5):618-26.

63. Dubowchik GM, Firestone RA, Padilla L, Willner D, Hofstead SJ, Mosure K, et al. Cathepsin B-labile dipeptide linkers for lysosomal release of doxorubicin from internalizing immunoconjugates: model studies of enzymatic drug release and antigen-specific in vitro anticancer activity. Bioconjug Chem. 2002 Jul-Aug;13(4):855-69.

64. Oldham EA, Li C, Ke S, Wallace S, Huang P. Comparison of action of paclitaxel and poly(L-glutamic acid)-paclitaxel conjugate in human breast cancer cells. Int J Oncol. 2000 Jan;16(1):125-32.

65. Liu J, Bauer H, Callahan J, Kopeckova P, Pan H, Kopecek J. Endocytic uptake of a large array of HPMA copolymers: Elucidation into the dependence on the physicochemical characteristics. J Control Release. 2010 Apr 2;143(1):71-9.

66. Greenwald RB, Gilbert CW, Pendri A, Conover CD, Xia J, Martinez A. Drug delivery systems: water soluble taxol 2'-poly(ethylene glycol) ester prodrugs-design and in vivo effectiveness. J Med Chem. 1996 Jan 19;39(2):424-31.

67. Yamaoka T, Tabata Y, Ikada Y. Distribution and tissue uptake of poly(ethylene glycol) with different molecular weights after intravenous administration to mice. J Pharm Sci. 1994 Apr;83(4):601-6.

68. Zhang X, Li Y, Chen X, Wang X, Xu X, Liang Q, et al. Synthesis and characterization of the paclitaxel/MPEG-PLA block copolymer conjugate. Biomaterials. 2005 May;26(14):2121-8.

69. Xie Z, Guan H, Chen X, Lu C, Chen L, Hu X, et al. A novel polymer-paclitaxel conjugate based on amphiphilic triblock copolymer. J Control Release. 2007 Feb 12;117(2):210-6.

70. Riebeseel K, Biedermann E, Loser R, Breiter N, Hanselmann R, Mulhaupt R, et al. Polyethylene glycol conjugates of methotrexate varying in their molecular weight from MW 750 to MW 40000: synthesis, characterization, and structure-activity relationships in vitro and in vivo. Bioconjug Chem. 2002 Jul-Aug;13(4):773-85.

71. Veronese FM, Schiavon O, Pasut G, Mendichi R, Andersson L, Tsirk A, et al. PEG-doxorubicin conjugates: influence of polymer structure on drug release, in vitro cytotoxicity, biodistribution, and antitumor activity. Bioconjug Chem. 2005 Jul-Aug;16(4):775-84.

72. Kopecek J. Polymer-drug conjugates: origins, progress to date and future directions. Adv Drug Deliv Rev. 2013 Jan;65(1):49-59.

73. Vasey PA, Kaye SB, Morrison R, Twelves C, Wilson P, Duncan R, et al. Phase I clinical and pharmacokinetic study of PK1 [N-(2-hydroxypropyl)methacrylamide copolymer doxorubicin]: first member of a new class of chemotherapeutic agents-drug-polymer conjugates. Cancer Research Campaign Phase I/II Committee. Clin Cancer Res. 1999 Jan;5(1):83-94.

74. Meerum Terwogt JM, ten Bokkel Huinink WW, Schellens JH, Schot M, Mandjes IA, Zurlo MG, et al. Phase I clinical and pharmacokinetic study of PNU166945, a novel water-soluble polymer-conjugated prodrug of paclitaxel. Anticancer Drugs. 2001 Apr;12(4):315-23.

75. Schoemaker NE, van Kesteren C, Rosing H, Jansen S, Swart M, Lieverst J, et al. A phase I and pharmacokinetic study of MAG-CPT, a water-soluble polymer conjugate of camptothecin. Br J Cancer. 2002 Sep 9;87(6):608-14.

76. Etrych T, Sirova M, Starovoytova L, Rihova B, Ulbrich K. HPMA copolymer conjugates of paclitaxel and docetaxel with pH-controlled drug release. Mol Pharm. 2010 Aug 2;7(4):1015-26.

77. Yang J, Luo K, Pan H, Kopeckova P, Kopecek J. Synthesis of Biodegradable Multiblock Copolymers by Click Coupling of RAFT-Generated HeterotelechelicPolyHPMA Conjugates. React Funct Polym. 2011 Mar 1;71(3):294-302.

78. Zhang R, Yang J, Sima M, Zhou Y, Kopecek J. Sequential combination therapy of ovarian cancer with degradable N-(2-hydroxypropyl)methacrylamide copolymer paclitaxel and gemcitabine conjugates. Proc Natl Acad Sci U S A. 2014 Aug 19;111(33):12181-6.

79. Akamatsu K, Yamasaki Y, Nishikawa M, Takakura Y, Hashida M. Development of a hepatocyte-specific prostaglandin E(1) polymeric prodrug and its potential for preventing carbon tetrachloride-induced fulminant hepatitis in mice. J Pharmacol Exp Ther. 1999 Sep;290(3):1242-9.

80. Sumi H, Kawabe K, Nakajima N. Effect of various polyamino acids and D- and L-amino acids on the blood fibrinolytic system. Comp Biochem Physiol B. 1992 May;102(1):159-62.

81. Li C. Poly(L-glutamic acid)--anticancer drug conjugates. Adv Drug Deliv Rev. 2002 Sep 13;54(5):695-713.

82. Hurwitz E, Wilchek M, Pitha J. Soluble macromolecules as carriers for daunorubicin. J Appl Biochem. 1980;2(1):25-35.

83. Zunino F, Pratesi G, Micheloni A. Poly(carboxylic acid) polymers as carriers for anthracyclines. J Controlled Release. 1989;10(1):65-73.

84. Hoes CJT, Grootoonk J, Duncan R, Hume IC, Bhakoo M, Bouma JMW, et al. Biological properties of adriamycin bound to biodegradable polymeric carriers. J Controlled Release. 1993 1;23(1):37-53.

85. Hoes CJT, Potman W, van Heeswijk WAR, Mud J, de Grooth BG, Greve J, et al. Optimization of macromolecular prodrugs of the antitumor antibiotic adriamycin. J Controlled Release. 1985 11;2(0):205-13.

86. Li C, Yu DF, Newman RA, Cabral F, Stephens LC, Hunter N, et al. Complete regression of well-established tumors using a novel water-soluble poly(L-glutamic acid)-paclitaxel conjugate. Cancer Res. 1998 Jun 1;58(11):2404-9.

87. Galanzha EI, Zharov VP. Circulating Tumor Cell Detection and Capture by Photoacoustic Flow Cytometry in Vivo and ex Vivo. Cancers (Basel). 2013 Dec 10;5(4):1691-738.

88. Kim JW, Galanzha EI, Zaharoff DA, Griffin RJ, Zharov VP. Nanotheranostics of circulating tumor cells, infections and other pathological features in vivo. Mol Pharm. 2013 Mar 4;10(3):813-30.

89. Wang CH, Chiou SH, Chou CP, Chen YC, Huang YJ, Peng CA. Photothermolysis of glioblastoma stem-like cells targeted by carbon nanotubes conjugated with CD133 monoclonal antibody. Nanomedicine. 2011 Feb;7(1):69-79.

90. Barth BM, I Altinoglu E, Shanmugavelandy SS, Kaiser JM, Crespo-Gonzalez D, DiVittore NA, et al. Targeted indocyanine-green-loaded calcium phosphosilicate nanoparticles for in vivo photodynamic therapy of leukemia. ACS Nano. 2011 Jul 26;5(7):5325-37.

91. Qiang YG, Yow CM, Huang Z. Combination of photodynamic therapy and immunomodulation: current status and future trends. Med Res Rev. 2008 Jul;28(4):632-44.

92. Almeida JP, Drezek RA, Foster AE. Controlling melanoma at local and systemic levels: is a combination of ablative therapy and immunotherapy the way forward? Immunotherapy. 2014;6(2):109-11.

93. Naylor MF, Chen WR, Teague TK, Perry LA, Nordquist RE. In situ photoimmunotherapy: a tumour-directed treatment for melanoma. Br J Dermatol. 2006 Dec;155(6):1287-92.

94. Li X, Naylor MF, Le H, Nordquist RE, Teague TK, Howard CA, et al. Clinical effects of in situ photoimmunotherapy on late-stage melanoma patients: a preliminary study. Cancer Biol Ther. 2010 Dec 1;10(11):1081-7.

95. Guo L, Yan DD, Yang D, Li Y, Wang X, Zalewski O, et al. Combinatorial photothermal and immuno cancer therapy using chitosan-coated hollow copper sulfide nanoparticles. ACS Nano. 2014 Jun 24;8(6):5670-81.

96. Bear AS, Kennedy LC, Young JK, Perna SK, Mattos Almeida JP, Lin AY, et al. Elimination of metastatic melanoma using gold nanoshell-enabled photothermal therapy and adoptive T cell transfer. PLoS One. 2013 Jul 23;8(7):e69073.

97. Snyder JW, Greco WR, Bellnier DA, Vaughan L, Henderson BW. Photodynamic therapy: a means to enhanced drug delivery to tumors. Cancer Res. 2003 Dec 1;63(23):8126-31.

98. Zhen Z, Tang W, Chuang YJ, Todd T, Zhang W, Lin X, et al. Tumor vasculature targeted photodynamic therapy for enhanced delivery of nanoparticles. ACS Nano. 2014 Jun 24;8(6):6004-13.

99. Selbo PK, Weyergang A, Hogset A, Norum OJ, Berstad MB, Vikdal M, et al. Photochemical internalization provides time- and space-controlled endolysosomal escape of therapeutic molecules. J Control Release. 2010 Nov 20;148(1):2-12.

100. Lou PJ, Lai PS, Shieh MJ, Macrobert AJ, Berg K, Bown SG. Reversal of doxorubicin resistance in breast cancer cells by photochemical internalization. Int J Cancer. 2006 Dec 1;119(11):2692-8.

101. Selbo PK, Rosenblum MG, Cheung LH, Zhang W, Berg K. Multi-modality therapeutics with potent anti-tumor effects: photochemical internalization enhances delivery of the fusion toxin scFvMEL/rGel. PLoS One. 2009 Aug 19;4(8):e6691.

102. Mathews MS, Vo V, Shih EC, Zamora G, Sun CH, Madsen SJ, et al. Photochemical internalization-mediated delivery of chemotherapeutic agents in human breast tumor cell lines. J Environ Pathol Toxicol Oncol. 2012;31(1):49-59.

103. Lu HL, Syu WJ, Nishiyama N, Kataoka K, Lai PS. Dendrimer phthalocyanine-encapsulated polymeric micelle-mediated photochemical internalization extends the

efficacy of photodynamic therapy and overcomes drug-resistance in vivo. J Control Release. 2011 Nov 7;155(3):458-64.

104. Lai PS, Pai CL, Peng CL, Shieh MJ, Berg K, Lou PJ. Enhanced cytotoxicity of saporin by polyamidoamine dendrimer conjugation and photochemical internalization. J Biomed Mater Res A. 2008 Oct;87(1):147-55.

105. Lai PS, Lou PJ, Peng CL, Pai CL, Yen WN, Huang MY, et al. Doxorubicin delivery by polyamidoamine dendrimer conjugation and photochemical internalization for cancer therapy. J Control Release. 2007 Sep 11;122(1):39-46.

106. Bostad M, Olsen CE, Peng Q, Berg K, Hogset A, Selbo PK. Light-controlled endosomal escape of the novel CD133-targeting immunotoxin AC133-saporin by photochemical internalization - A minimally invasive cancer stem cell-targeting strategy. J Control Release. 2015 Mar 7;206:37-48.

107. Ruoslahti E, Bhatia SN, Sailor MJ. Targeting of drugs and nanoparticles to tumors. The Journal of Cell Biology. 2010 March 22;188(6):759-68.

108. Pirollo KF, Chang EH. Does a targeting ligand influence nanoparticle tumor localization or uptake? Trends Biotechnol. 2008 Oct;26(10):552-8.

109. Gu FX, Karnik R, Wang AZ, Alexis F, Levy-Nissenbaum E, Hong S, et al. Targeted nanoparticles for cancer therapy. Nano Today. 2007 6;2(3):14-21.

110. Weis SM, Cheresh DA. alphaV integrins in angiogenesis and cancer. Cold Spring Harb Perspect Med. 2011 Sep;1(1):a006478.

111. Felding-Habermann B, Fransvea E, O'Toole TE, Manzuk L, Faha B, Hensler M. Involvement of tumor cell integrin alpha v beta 3 in hematogenous metastasis of human melanoma cells. Clin Exp Metastasis. 2002;19(5):427-36.

112. Hersel U, Dahmen C, Kessler H. RGD modified polymers: biomaterials for stimulated cell adhesion and beyond. Biomaterials. 2003 Nov;24(24):4385-415.

113. Phillips E, Penate-Medina O, Zanzonico PB, Carvajal RD, Mohan P, Ye Y, et al. Clinical translation of an ultrasmall inorganic optical-PET imaging nanoparticle probe. Sci Transl Med. 2014 Oct 29;6(260):260ra149.

114. Wagner S, Rothweiler F, Anhorn MG, Sauer D, Riemann I, Weiss EC, et al. Enhanced drug targeting by attachment of an anti alphav integrin antibody to doxorubicin loaded human serum albumin nanoparticles. Biomaterials. 2010 Mar;31(8):2388-98.

115. Ledda F, Bravo AI, Adris S, Bover L, Mordoh J, Podhajcer OL. The expression of the secreted protein acidic and rich in cysteine (SPARC) is associated with the neoplastic progression of human melanoma. J Invest Dermatol. 1997 Feb;108(2):210-4.

116. Ikuta Y, Nakatsura T, Kageshita T, Fukushima S, Ito S, Wakamatsu K, et al. Highly sensitive detection of melanoma at an early stage based on the increased serum secreted protein acidic and rich in cysteine and glypican-3 levels. Clin Cancer Res. 2005 Nov 15;11(22):8079-88.

117. Robert G, Gaggioli C, Bailet O, Chavey C, Abbe P, Aberdam E, et al. SPARC represses E-cadherin and induces mesenchymal transition during melanoma development. Cancer Res. 2006 Aug 1;66(15):7516-23.

118. Thomas S, Waterman P, Chen S, Marinelli B, Seaman M, Rodig S, et al. Development of Secreted Protein and Acidic and Rich in Cysteine (SPARC) Targeted Nanoparticles for the Prognostic Molecular Imaging of Metastatic Prostate Cancer. J Nanomed Nanotechnol. 2011 Aug;2(112):2157,7439-2-112.

119. Sheng Z, Hu D, Zheng M, Zhao P, Liu H, Gao D, et al. Smart human serum albumin-indocyanine green nanoparticles generated by programmed assembly for dual-modal imaging-guided cancer synergistic phototherapy. ACS Nano. 2014 Dec 23;8(12):12310-22.

120. Desai N, Trieu V, Damascelli B, Soon-Shiong P. SPARC Expression Correlates with Tumor Response to Albumin-Bound Paclitaxel in Head and Neck Cancer Patients. Transl Oncol. 2009 May;2(2):59-64.

121. Desai NP, Trieu V, Hwang LY, Wu R, Soon-Shiong P, Gradishar WJ. Improved effectiveness of nanoparticle albumin-bound (nab) paclitaxel versus polysorbate-based docetaxel in multiple xenografts as a function of HER2 and SPARC status. Anticancer Drugs. 2008 Oct;19(9):899-909.

122. Schneeweiss A, Seitz J, Smetanay K, Schuetz F, Jaeger D, Bachinger A, et al. Efficacy of nab-paclitaxel does not seem to be associated with SPARC expression in metastatic breast cancer. Anticancer Res. 2014 Nov;34(11):6609-15.

123. Shao H, Tang H, Salavaggione OE, Yu C, Hylander B, Tan W, et al. Improved response to nab-paclitaxel compared with cremophor-solubilized paclitaxel is independent of secreted protein acidic and rich in cysteine expression in non-small cell lung cancer. J Thorac Oncol. 2011 Jun;6(6):998-1005.

124. Neesse A, Frese KK, Chan DS, Bapiro TE, Howat WJ, Richards FM, et al. SPARC independent drug delivery and antitumour effects of nab-paclitaxel in genetically engineered mice. Gut. 2014 Jun;63(6):974-83.

125. Simberg D, Duza T, Park JH, Essler M, Pilch J, Zhang L, et al. Biomimetic amplification of nanoparticle homing to tumors. Proc Natl Acad Sci U S A. 2007 Jan 16;104(3):932-6.

126. Daniels TR, Delgado T, Helguera G, Penichet ML. The transferrin receptor part II: targeted delivery of therapeutic agents into cancer cells. Clin Immunol. 2006 Nov;121(2):159-76.

127. Davis ME, Zuckerman JE, Choi CH, Seligson D, Tolcher A, Alabi CA, et al. Evidence of RNAi in humans from systemically administered siRNA via targeted nanoparticles. Nature. 2010 Apr 15;464(7291):1067-70.

128. Pun SH, Tack F, Bellocq NC, Cheng J, Grubbs BH, Jensen GS, et al. Targeted delivery of RNA-cleaving DNA enzyme (DNAzyme) to tumor tissue by transferrin-modified, cyclodextrin-based particles. Cancer Biol Ther. 2004 Jul;3(7):641-50.

129. Davis ME. The first targeted delivery of siRNA in humans via a self-assembling, cyclodextrin polymer-based nanoparticle: from concept to clinic. Mol Pharm. 2009 May-Jun;6(3):659-68.

130. Dube DH, Bertozzi CR. Glycans in cancer and inflammation--potential for therapeutics and diagnostics. Nat Rev Drug Discov. 2005 Jun;4(6):477-88.

131. Matsumoto A, Cabral H, Sato N, Kataoka K, Miyahara Y. Assessment of tumor metastasis by the direct determination of cell-membrane sialic acid expression. Angew Chem Int Ed Engl. 2010 Jul 26;49(32):5494-7.

132. Matsumoto A, Sato N, Kataoka K, Miyahara Y. Noninvasive sialic acid detection at cell membrane by using phenylboronic acid modified self-assembled monolayer gold electrode. J Am Chem Soc. 2009 Sep 2;131(34):12022-3.

133. Deshayes S, Cabral H, Ishii T, Miura Y, Kobayashi S, Yamashita T, et al. Phenylboronic acid-installed polymeric micelles for targeting sialylated epitopes in solid tumors. J Am Chem Soc. 2013 Oct 16;135(41):15501-7.

134. Siegrist W, Solca F, Stutz S, Giuffre L, Carrel S, Girard J, et al. Characterization of receptors for alpha-melanocyte-stimulating hormone on human melanoma cells. Cancer Res. 1989 Nov 15;49(22):6352-8.

135. Ghanem GE, Libert A, Arnould R, Vercammen A, Lejeune F. Human melanoma targeting with alpha-MSH-melphalan conjugate. Melanoma Res. 1991 Jun-Jul;1(2):105-14.

136. Lu W, Xiong C, Zhang G, Huang Q, Zhang R, Zhang JZ, et al. Targeted photothermal ablation of murine melanomas with melanocyte-stimulating hormone

analog-conjugated hollow gold nanospheres. Clin Cancer Res. 2009 Feb 1;15(3):876-86.

137. Kim C, Cho EC, Chen J, Song KH, Au L, Favazza C, et al. In vivo molecular photoacoustic tomography of melanomas targeted by bioconjugated gold nanocages. ACS Nano. 2010 Aug 24;4(8):4559-64.

138. Falvo E, Tremante E, Fraioli R, Leonetti C, Zamparelli C, Boffi A, et al. Antibody-drug conjugates: targeting melanoma with cisplatin encapsulated in protein-cage nanoparticles based on human ferritin. Nanoscale. 2013 Dec 21;5(24):12278-85.

139. Boussemart L, Routier E, Mateus C, Opletalova K, Sebille G, Kamsu-Kom N, et al. Prospective study of cutaneous side-effects associated with the BRAF inhibitor vemurafenib: a study of 42 patients. Ann Oncol. 2013 Jun;24(6):1691-7.

140. Anforth R, Fernandez-Penas P, Long GV. Cutaneous toxicities of RAF inhibitors. Lancet Oncol. 2013 Jan;14(1):e11-8.

141. Duncan R. Polymer conjugates as anticancer nanomedicines. Nat Rev Cancer. 2006 Sep;6(9):688-701.

142. Davids LM, Kleemann B. Combating melanoma: the use of photodynamic therapy as a novel, adjuvant therapeutic tool. Cancer Treat Rev. 2011 Oct;37(6):465-75.

143. Dolmans DE, Fukumura D, Jain RK. Photodynamic therapy for cancer. Nat Rev Cancer. 2003 May;3(5):380-7.

144. Rai P, Mallidi S, Zheng X, Rahmanzadeh R, Mir Y, Elrington S, et al. Development and applications of photo-triggered theranostic agents. Adv Drug Deliv Rev. 2010 Aug 30;62(11):1094-124.

145. Marshall MV, Rasmussen JC, Tan IC, Aldrich MB, Adams KE, Wang X, et al. Near-Infrared Fluorescence Imaging in Humans with Indocyanine Green: A Review and Update. Open Surg Oncol J. 2010;2(2):12-25.

146. Ott P. Hepatic elimination of indocyanine green with special reference to distribution kinetics and the influence of plasma protein binding. Pharmacol Toxicol. 1998;83 Suppl 2:1-48.

147. Yu J, Javier D, Yaseen MA, Nitin N, Richards-Kortum R, Anvari B, et al. Self-assembly synthesis, tumor cell targeting, and photothermal capabilities of antibody-coated indocyanine green nanocapsules. J Am Chem Soc. 2010 Feb 17;132(6):1929-38.

148. Altinoglu EI, Russin TJ, Kaiser JM, Barth BM, Eklund PC, Kester M, et al. Near-infrared emitting fluorophore-doped calcium phosphate nanoparticles for in vivo imaging of human breast cancer. ACS Nano. 2008 Oct 28;2(10):2075-84.

149. Saxena V, Sadoqi M, Shao J. Indocyanine green-loaded biodegradable nanoparticles: preparation, physicochemical characterization and in vitro release. Int J Pharm. 2004 Jul 8;278(2):293-301.

150. Miki K, Inoue T, Kobayashi Y, Nakano K, Matsuoka H, Yamauchi F, et al. Near-infrared dye-conjugated amphiphilic hyaluronic acid derivatives as a dual contrast agent for in vivo optical and photoacoustic tumor imaging. Biomacromolecules. 2015 Jan 12;16(1):219-27.

151. Shemesh CS, Moshkelani D, Zhang H. Thermosensitive liposome formulated indocyanine green for near-infrared triggered photodynamic therapy: in vivo evaluation for triple-negative breast cancer. Pharm Res. 2015 May;32(5):1604-14.

152. Sharma P, Bengtsson NE, Walter GA, Sohn HB, Zhou G, Iwakuma N, et al. Gadolinium-doped silica nanoparticles encapsulating indocyanine green for near infrared and magnetic resonance imaging. Small. 2012 Sep 24;8(18):2856-68.

153. de la Zerda A, Liu Z, Bodapati S, Teed R, Vaithilingam S, Khuri-Yakub BT, et al. Ultrahigh sensitivity carbon nanotube agents for photoacoustic molecular imaging in living mice. Nano Lett. 2010 Jun 9;10(6):2168-72.

154. Mundra V, Peng Y, Kumar V, Li W, Miller DD, Mahato RI. Systemic delivery of nanoparticle formulation of novel tubulin inhibitor for treating metastatic melanoma. Drug Deliv Transl Res. 2015 Jun;5(3):199-208.

155. Wan Z, Mao H, Guo M, Li Y, Zhu A, Yang H, et al. Highly efficient hierarchical micelles integrating photothermal therapy and singlet oxygen-synergized chemotherapy for cancer eradication. Theranostics. 2014 Jan 29;4(4):399-411.

156. Uong A, Zon LI. Melanocytes in development and cancer. J Cell Physiol. 2010 Jan;222(1):38-41.

157. Sheng Z, Hu D, Xue M, He M, Ping Gong and LC. Indocyanine Green Nanoparticles for Theranostic Applications. Nano-Micro Letters. 2013 -07-25; 2013-07-25;5(3):145-50.

158. Chen H, Kim S, He W, Wang H, Low PS, Park K, et al. Fast release of lipophilic agents from circulating PEG-PDLLA micelles revealed by in vivo forster resonance energy transfer imaging. Langmuir. 2008 May 20;24(10):5213-7.

159. Daniele MA, Shaughnessy ML, Roeder R, Childress A, Bandera YP, Foulger S. Magnetic nanoclusters exhibiting protein-activated near-infrared fluorescence. ACS Nano. 2013 Jan 22;7(1):203-13.

160. Li F, Danquah M, Mahato RI. Synthesis and characterization of amphiphilic lipopolymers for micellar drug delivery. Biomacromolecules. 2010 Oct 11;11(10):2610-20.

161. Tang L, Yang X, Yin Q, Cai K, Wang H, Chaudhury I, et al. Investigating the optimal size of anticancer nanomedicine. Proc Natl Acad Sci U S A. 2014 Oct 28;111(43):15344-9.

162. Meng H, Xue M, Xia T, Ji Z, Tarn DY, Zink JI, et al. Use of size and a copolymer design feature to improve the biodistribution and the enhanced permeability and retention effect of doxorubicin-loaded mesoporous silica nanoparticles in a murine xenograft tumor model. ACS Nano. 2011 May 24;5(5):4131-44.

163. Owen SC, Chan DPY, Shoichet MS. Polymeric micelle stability. Nano Today. 2012 2;7(1):53-65.

164. Xu P, Gullotti E, Tong L, Highley CB, Errabelli DR, Hasan T, et al. Intracellular drug delivery by poly(lactic-co-glycolic acid) nanoparticles, revisited. Mol Pharm. 2009 Jan-Feb;6(1):190-201.

165. Chen H, Kim S, Li L, Wang S, Park K, Cheng JX. Release of hydrophobic molecules from polymer micelles into cell membranes revealed by Forster resonance energy transfer imaging. Proc Natl Acad Sci U S A. 2008 May 6;105(18):6596-601.

166. Ding H, Sumer BD, Kessinger CW, Dong Y, Huang G, Boothman DA, et al. Nanoscopic micelle delivery improves the photophysical properties and efficacy of photodynamic therapy of protoporphyrin IX. J Control Release. 2011 May 10;151(3):271-7.

167. Mundra V, Mahato R. Design of nanocarriers for efficient cellular uptake and endosomal release of small molecule and nucleic acid drugs: learning from virus. Frontiers of Chemical Science and Engineering. 2014 12/01;8(4):387-404.

168. Zheng M, Yue C, Ma Y, Gong P, Zhao P, Zheng C, et al. Single-step assembly of DOX/ICG loaded lipid--polymer nanoparticles for highly effective chemo-photothermal combination therapy. ACS Nano. 2013 Mar 26;7(3):2056-67.

169. Attia AB, Yang C, Tan JP, Gao S, Williams DF, Hedrick JL, et al. The effect of kinetic stability on biodistribution and anti-tumor efficacy of drug-loaded biodegradable polymeric micelles. Biomaterials. 2013 Apr;34(12):3132-40.

170. [Internet]. []. Available from: http://seer.cancer.gov/statfacts/html/melan.html.

171. Gray-Schopfer V, Wellbrock C, Marais R. Melanoma biology and new targeted therapy. Nature. 2007 Feb 22;445(7130):851-7.

172. Hersh EM, O'Day SJ, Ribas A, Samlowski WE, Gordon MS, Shechter DE, et al. A phase 2 clinical trial of nab-paclitaxel in previously treated and chemotherapy-naive patients with metastatic melanoma. Cancer. 2010 Jan 1;116(1):155-63.

173. Lu Y, Chen J, Xiao M, Li W, Miller DD. An overview of tubulin inhibitors that interact with the colchicine binding site. Pharm Res. 2012 Nov;29(11):2943-71.

174. Wang Z, Chen J, Wang J, Ahn S, Li CM, Lu Y, et al. Novel tubulin polymerization inhibitors overcome multidrug resistance and reduce melanoma lung metastasis. Pharm Res. 2012 Nov;29(11):3040-52.

175. ten Bokkel Huinink WW, Eisenhauer E, Swenerton K. Preliminary evaluation of a multicenter, randomized comparative study of TAXOL (paclitaxel) dose and infusion length in platinum-treated ovarian cancer. Canadian-European Taxol Cooperative Trial Group. Cancer Treat Rev. 1993;19 Suppl C:79-86.

176. Hamaguchi T, Kato K, Yasui H, Morizane C, Ikeda M, Ueno H, et al. A phase I and pharmacokinetic study of NK105, a paclitaxel-incorporating micellar nanoparticle formulation. Br J Cancer. 2007 Jul 16;97(2):170-6.

177. Danquah M, Li F, Duke CB,3rd, Miller DD, Mahato RI. Micellar delivery of bicalutamide and embelin for treating prostate cancer. Pharm Res. 2009 Sep;26(9):2081-92.

178. Gaucher G, Marchessault RH, Leroux JC. Polyester-based micelles and nanoparticles for the parenteral delivery of taxanes. J Control Release. 2010 Apr 2;143(1):2-12.

179. Danquah MK, Zhang XA, Mahato RI. Extravasation of polymeric nanomedicines across tumor vasculature. Adv Drug Deliv Rev. 2011 Jul 18;63(8):623-39.

180. Maeda H, Wu J, Sawa T, Matsumura Y, Hori K. Tumor vascular permeability and the EPR effect in macromolecular therapeutics: a review. J Control Release. 2000 Mar 1;65(1-2):271-84.

181. Nederberg F, Lohmeijer BG, Leibfarth F, Pratt RC, Choi J, Dove AP, et al. Organocatalytic ring opening polymerization of trimethylene carbonate. Biomacromolecules. 2007 Jan;8(1):153-60.

182. Lohmeijer B, Pratt RC, Leibfarth F, Logan JW, Long DA, Dove AP, et al. Guanidine and amidine organocatalysts for ring-opening polymerization of cyclic esters. Macromolecules. 2006;39(25):8574-83.

183. Tas F. Metastatic behavior in melanoma: timing, pattern, survival, and influencing factors. J Oncol. 2012;2012:647684.

184. Soengas MS, Lowe SW. Apoptosis and melanoma chemoresistance. Oncogene. 2003 May 19;22(20):3138-51.

185. Frank NY, Margaryan A, Huang Y, Schatton T, Waaga-Gasser AM, Gasser M, et al. ABCB5-mediated doxorubicin transport and chemoresistance in human malignant melanoma. Cancer Res. 2005 May 15;65(10):4320-33.

186. La Porta CA. Drug resistance in melanoma: new perspectives. Curr Med Chem. 2007;14(4):387-91.

187. Li CM, Chen J, Lu Y, Narayanan R, Parke DN, Li W, et al. Pharmacokinetic optimization of 4-substituted methoxybenzoyl-aryl-thiazole and 2-aryl-4-benzoyl-imidazole for improving oral bioavailability. Drug Metab Dispos. 2011 Oct;39(10):1833-9.

188. Dahan A, Sabit H, Amidon GL. Multiple efflux pumps are involved in the transepithelial transport of colchicine: combined effect of p-glycoprotein and multidrug resistance-associated protein 2 leads to decreased intestinal absorption throughout the entire small intestine. Drug Metab Dispos. 2009 Oct;37(10):2028-36.

189. Dahan A, Amidon GL. Grapefruit juice and its constituents augment colchicine intestinal absorption: potential hazardous interaction and the role of p-glycoprotein. Pharm Res. 2009 Apr;26(4):883-92.

190. Seow WY, Yang YY. Functional polycarbonates and their self-assemblies as promising non-viral vectors. J Control Release. 2009 Oct 1;139(1):40-7.

191. Maeda H, Bharate GY, Daruwalla J. Polymeric drugs for efficient tumor-targeted drug delivery based on EPR-effect. Eur J Pharm Biopharm. 2009 Mar;71(3):409-19.

192. Gores PF, Kaufman DB, Sutherland DE. New strategies for clinical islet transplantation. The role of purified grafts and immunosuppressive therapy. Ann N Y Acad Sci. 1993 Nov 30;696:377-89.

193. Barshes NR, Wyllie S, Goss JA. Inflammation-mediated dysfunction and apoptosis in pancreatic islet transplantation: implications for intrahepatic grafts. J Leukoc Biol. 2005 May;77(5):587-97.

194. Ryan EA, Paty BW, Senior PA, Bigam D, Alfadhli E, Kneteman NM, et al. Five-year follow-up after clinical islet transplantation. Diabetes. 2005 Jul;54(7):2060-9.

195. Grunnet LG, Aikin R, Tonnesen MF, Paraskevas S, Blaabjerg L, Storling J, et al. Proinflammatory cytokines activate the intrinsic apoptotic pathway in beta-cells. Diabetes. 2009 Aug;58(8):1807-15.

196. Giannoukakis N, Rudert WA, Ghivizzani SC, Gambotto A, Ricordi C, Trucco M, et al. Adenoviral gene transfer of the interleukin-1 receptor antagonist protein to human islets prevents IL-1beta-induced beta-cell impairment and activation of islet cell apoptosis in vitro. Diabetes. 1999 Sep;48(9):1730-6.

197. Narang AS, Sabek O, Gaber AO, Mahato RI. Co-expression of vascular endothelial growth factor and interleukin-1 receptor antagonist improves human islet survival and function. Pharm Res. 2006 Sep;23(9):1970-82.

198. Henderson JR, Moss MC. A morphometric study of the endocrine and exocrine capillaries of the pancreas. Q J Exp Physiol. 1985 Jul;70(3):347-56.

199. Kuroda M, Oka T, Oka Y, Yamochi T, Ohtsubo K, Mori S, et al. Colocalization of vascular endothelial growth factor (vascular permeability factor) and insulin in pancreatic islet cells. J Clin Endocrinol Metab. 1995 Nov;80(11):3196-200.

200. Johansson M, Mattsson G, Andersson A, Jansson L, Carlsson PO. Islet endothelial cells and pancreatic beta-cell proliferation: studies in vitro and during pregnancy in adult rats. Endocrinology. 2006 May;147(5):2315-24.

201. Nyqvist D, Speier S, Rodriguez-Diaz R, Molano RD, Lipovsek S, Rupnik M, et al. Donor islet endothelial cells in pancreatic islet revascularization. Diabetes. 2011 Oct;60(10):2571-7.

202. Brissova M, Fowler M, Wiebe P, Shostak A, Shiota M, Radhika A, et al. Intraislet endothelial cells contribute to revascularization of transplanted pancreatic islets. Diabetes. 2004 May;53(5):1318-25.

203. Cai Q, Brissova M, Reinert RB, Pan FC, Brahmachary P, Jeansson M, et al. Enhanced expression of VEGF-A in beta cells increases endothelial cell number but impairs islet morphogenesis and beta cell proliferation. Dev Biol. 2012 Jul 1;367(1):40-54.

204. Zhang N, Richter A, Suriawinata J, Harbaran S, Altomonte J, Cong L, et al. Elevated vascular endothelial growth factor production in islets improves islet graft vascularization. Diabetes. 2004 Apr;53(4):963-70.

205. Berman DM, Willman MA, Han D, Kleiner G, Kenyon NM, Cabrera O, et al. Mesenchymal stem cells enhance allogeneic islet engraftment in nonhuman primates. Diabetes. 2010 Oct;59(10):2558-68.

206. Panakanti R, Mahato RI. Bipartite adenoviral vector encoding hHGF and hIL-1Ra for improved human islet transplantation. Pharm Res. 2009 Mar;26(3):587-96.

207. Biarnes M, Montolio M, Nacher V, Raurell M, Soler J, Montanya E. Beta-cell death and mass in syngeneically transplanted islets exposed to short- and long-term hyperglycemia. Diabetes. 2002 Jan;51(1):66-72.

208. Garcia-Ocana A, Takane KK, Reddy VT, Lopez-Talavera JC, Vasavada RC, Stewart AF. Adenovirus-mediated hepatocyte growth factor expression in mouse islets improves pancreatic islet transplant performance and reduces beta cell death. J Biol Chem. 2003 Jan 3;278(1):343-51.

209. Bertuzzi F, Grohovaz F, Maffi P, Caumo A, Aldrighetti L, Nano R, et al. Successful [correction of Succesful] transplantation of human islets in recipients bearing a kidney graft. Diabetologia. 2002 Jan;45(1):77-84.

210. Shapiro AM, Ricordi C, Hering BJ, Auchincloss H, Lindblad R, Robertson RP, et al. International trial of the Edmonton protocol for islet transplantation. N Engl J Med. 2006 Sep 28;355(13):1318-30.

211. Delaney CA, Pavlovic D, Hoorens A, Pipeleers DG, Eizirik DL. Cytokines induce deoxyribonucleic acid strand breaks and apoptosis in human pancreatic islet cells. Endocrinology. 1997 Jun;138(6):2610-4.

212. Schwarznau A, Hanson MS, Sperger JM, Schram BR, Danobeitia JS, Greenwood KK, et al. IL-1beta receptor blockade protects islets against pro-inflammatory cytokine induced necrosis and apoptosis. J Cell Physiol. 2009 Aug;220(2):341-7.

213. Maedler K, Sergeev P, Ris F, Oberholzer J, Joller-Jemelka HI, Spinas GA, et al. Glucose-induced beta cell production of IL-1beta contributes to glucotoxicity in human pancreatic islets. J Clin Invest. 2002 Sep;110(6):851-60.

214. Rosenberg L, Wang R, Paraskevas S, Maysinger D. Structural and functional changes resulting from islet isolation lead to islet cell death. Surgery. 1999 Aug;126(2):393-8.

215. Matsuda T, Omori K, Vuong T, Pascual M, Valiente L, Ferreri K, et al. Inhibition of p38 pathway suppresses human islet production of pro-inflammatory cytokines and improves islet graft function. Am J Transplant. 2005 Mar;5(3):484-93.

216. Augstein P, Bahr J, Wachlin G, Heinke P, Berg S, Salzsieder E, et al. Cytokines activate caspase-3 in insulinoma cells of diabetes-prone NOD mice directly and via upregulation of Fas. J Autoimmun. 2004 Dec;23(4):301-9.

217. Sarkar SA, Kutlu B, Velmurugan K, Kizaka-Kondoh S, Lee CE, Wong R, et al. Cytokine-mediated induction of anti-apoptotic genes that are linked to nuclear factor

kappa-B (NF-kappaB) signalling in human islets and in a mouse beta cell line. Diabetologia. 2009 Jun;52(6):1092-101.

218. Pittenger MF, Mackay AM, Beck SC, Jaiswal RK, Douglas R, Mosca JD, et al. Multilineage potential of adult human mesenchymal stem cells. Science. 1999 Apr 2;284(5411):143-7.

219. Russell KC, Phinney DG, Lacey MR, Barrilleaux BL, Meyertholen KE, O'Connor KC. In vitro high-capacity assay to quantify the clonal heterogeneity in trilineage potential of mesenchymal stem cells reveals a complex hierarchy of lineage commitment. Stem Cells. 2010 Apr;28(4):788-98.

220. Dominici M, Le Blanc K, Mueller I, Slaper-Cortenbach I, Marini F, Krause D, et al. Minimal criteria for defining multipotent mesenchymal stromal cells. The International Society for Cellular Therapy position statement. Cytotherapy. 2006;8(4):315-7.

221. Psaltis PJ, Paton S, See F, Arthur A, Martin S, Itescu S, et al. Enrichment for STRO-1 expression enhances the cardiovascular paracrine activity of human bone marrow-derived mesenchymal cell populations. J Cell Physiol. 2010 May;223(2):530-40.

222. Tondreau T, Lagneaux L, Dejeneffe M, Delforge A, Massy M, Mortier C, et al. Isolation of BM mesenchymal stem cells by plastic adhesion or negative selection: phenotype, proliferation kinetics and differentiation potential. Cytotherapy. 2004;6(4):372-9.

223. Stiehler M, Duch M, Mygind T, Li H, Ulrich-Vinther M, Modin C, et al. Optimizing viral and non-viral gene transfer methods for genetic modification of porcine mesenchymal stem cells. Adv Exp Med Biol. 2006;585:31-48.

224. McMahon JM, Conroy S, Lyons M, Greiser U, O'shea C, Strappe P, et al. Gene transfer into rat mesenchymal stem cells: a comparative study of viral and nonviral vectors. Stem Cells Dev. 2006 Feb;15(1):87-96.

225. Porada CD, Almeida-Porada G. Mesenchymal stem cells as therapeutics and vehicles for gene and drug delivery. Adv Drug Deliv Rev. 2010 Sep 30;62(12):1156-66.

226. McGinley L, McMahon J, Strappe P, Barry F, Murphy M, O'Toole D, et al. Lentiviral vector mediated modification of mesenchymal stem cells & enhanced survival in an in vitro model of ischaemia. Stem Cell Res Ther. 2011 Mar 7;2(2):12.

227. Treacy O, Ryan AE, Heinzl T, O'Flynn L, Cregg M, Wilk M, et al. Adenoviral transduction of mesenchymal stem cells: in vitro responses and in vivo immune responses after cell transplantation. PLoS One. 2012;7(8):e42662.

228. Liu TM, Wu YN, Guo XM, Hui JH, Lee EH, Lim B. Effects of ectopic Nanog and Oct4 overexpression on mesenchymal stem cells. Stem Cells Dev. 2009 Sep;18(7):1013-22.

229. Go MJ, Takenaka C, Ohgushi H. Forced expression of Sox2 or Nanog in human bone marrow derived mesenchymal stem cells maintains their expansion and differentiation capabilities. Exp Cell Res. 2008 Mar 10;314(5):1147-54.

230. Wu H, Ye Z, Mahato RI. Genetically modified mesenchymal stem cells for improved islet transplantation. Mol Pharm. 2011 Oct 3;8(5):1458-70.

231. Sordi V, Melzi R, Mercalli A, Formicola R, Doglioni C, Tiboni F, et al. Mesenchymal cells appearing in pancreatic tissue culture are bone marrow-derived stem cells with the capacity to improve transplanted islet function. Stem Cells. 2010 Jan;28(1):140-51.

232. Milanesi A, Lee JW, Li Z, Da Sacco S, Villani V, Cervantes V, et al. beta-Cell regeneration mediated by human bone marrow mesenchymal stem cells. PLoS One. 2012;7(8):e42177.

233. Ito T, Itakura S, Todorov I, Rawson J, Asari S, Shintaku J, et al. Mesenchymal stem cell and islet co-transplantation promotes graft revascularization and function. Transplantation. 2010 Jun 27;89(12):1438-45.

234. Hess D, Li L, Martin M, Sakano S, Hill D, Strutt B, et al. Bone marrow-derived stem cells initiate pancreatic regeneration. Nat Biotechnol. 2003 Jul;21(7):763-70.

235. Luo JZ, Xiong F, Al-Homsi AS, Roy T, Luo LG. Human BM stem cells initiate angiogenesis in human islets in vitro. Bone Marrow Transplant. 2011 Aug;46(8):1128-37.

236. Zheng YB, Zhang XH, Huang ZL, Lin CS, Lai J, Gu YR, et al. Amniotic-fluid-derived mesenchymal stem cells overexpressing interleukin-1 receptor antagonist improve fulminant hepatic failure. PLoS One. 2012;7(7):e41392.

237. Duprez IR, Johansson U, Nilsson B, Korsgren O, Magnusson PU. Preparatory studies of composite mesenchymal stem cell islets for application in intraportal islet transplantation. Ups J Med Sci. 2011 Mar;116(1):8-17.

238. Jang B, Choi Y. Photosensitizer-conjugated gold nanorods for enzyme-activatable fluorescence imaging and photodynamic therapy. Theranostics. 2012;2(2):190-7.

239. Choi Y, Weissleder R, Tung CH. Selective antitumor effect of novel protease-mediated photodynamic agent. Cancer Res. 2006 Jul 15;66(14):7225-9.

240. Quan B, Choi K, Kim YH, Kang KW, Chung DS. Near infrared dye indocyanine green doped silica nanoparticles for biological imaging. Talanta. 2012 Sep 15;99:387-93.

241. Tang Y, McGoron AJ. Combined effects of laser-ICG photothermotherapy and doxorubicin chemotherapy on ovarian cancer cells. J Photochem Photobiol B. 2009 Dec 2;97(3):138-44.

242. Zheng M, Yue C, Ma Y, Gong P, Zhao P, Zheng C, et al. Single-step assembly of DOX/ICG loaded lipid--polymer nanoparticles for highly effective chemo-photothermal combination therapy. ACS Nano. 2013 Mar 26;7(3):2056-67.

243. Zhao C, Wu N, Deng F, Zhang H, Wang N, Zhang W, et al. Adenovirus-mediated gene transfer in mesenchymal stem cells can be significantly enhanced by the cationic polymer polybrene. PLoS One. 2014 Mar 21;9(3):e92908.

244. Tsuda H, Wada T, Ito Y, Uchida H, Dehari H, Nakamura K, et al. Efficient BMP2 gene transfer and bone formation of mesenchymal stem cells by a fiber-mutant adenoviral vector. Mol Ther. 2003 Mar;7(3):354-65.

245. Park SH, Doh J, Park SI, Lim JY, Kim SM, Youn JI, et al. Branched oligomerization of cell-permeable peptides markedly enhances the transduction efficiency of adenovirus into mesenchymal stem cells. Gene Ther. 2010 Aug;17(8):1052-61.

246. Yao X, Zhou N, Wan L, Su X, Sun Z, Mizuguchi H, et al. Polyethyleneimine-coating enhances adenoviral transduction of mesenchymal stem cells. Biochem Biophys Res Commun. 2014 May 9;447(3):383-7.